

Doctoral Thesis

Spatial and Temporal Variabilities of
Mesospheric Concentric Gravity Waves Revealed with a
Space Borne Visible Spectroscopic Instrument

衛星搭載分光器による
中間圏同心状大気重力波の空間・時間変動

Septi Perwitasari
(セプティ・ペルウィタサリ)

Department of Geophysics
Graduate School of Science
Tohoku University
2016

Doctor Thesis

Spatial and Temporal Variabilities of Mesospheric Concentric Gravity Waves Revealed with a Space Borne Visible Spectroscopic Instrument

衛星搭載分光器による
中間圏同心状大気重力波の空間・時間変動

Septi Perwitasari
(セプテイ・ペルウィタサリ)

Department of Geophysics
Graduate School of Science
Tohoku University

Thesis Committee Members

Associate Professor Takeshi Sakanoi (chair, supervisor)
Professor Takahiro Obara
Professor Yasumasa Kasaba
Associate Professor Isao Murata
Associate Professor Atsushi Kumamoto
Assistant Professor Mitsumu K. Ejiri (NIPR)

2016

Abstract

This thesis focuses on the spatial and temporal variability of concentric gravity waves (CGWs) in the mesopause region based on the O₂ A-band (762 nm) nightglow data obtained with IMAP/VISI. Atmospheric gravity waves (AGWs) have been studied intensively because of their major role in the atmospheric dynamics, such as transporting energy and momentum and interaction to the mean wind and thermal structure of the middle atmosphere. CGWs are one of the most distinct features of gravity waves, which show a direct coupling between lower and upper atmosphere. The past studies have revealed the general properties of CGWs, such as launching mechanism and effect of the background wind profile. However, these are mostly based on a single event, which give only local information. Thus, a statistical approach with space-based observations is ideal since they cover wider area globally and can measure atmospheric gravity waves without cloud obscuration.

For the data analysis, we used the airglow data measured with the Visible and near-Infrared Spectral Imager (VISI) of the IMAP mission on the International Space Station (ISS). IMAP/VISI was operated from October 2012 until August 2015 in the nightside hemisphere with geographical latitude range of $\pm 51^\circ$, measuring mainly three different airglow emissions of OI at 630 nm, the OH Meinel band at 730 nm and the O₂ (0-0) A-band at 762 nm at an altitude of ~ 400 km with the typical spatial resolution of 16 – 50 km.

The present study of CGWs is divided into two parts; the first part is a case study using the coordinated observations of IMAP/VISI and ground-based all-sky imager at Rikubetsu, and the second part is a statistical study on the global distribution and seasonal variability of CGWs. Here we examined a partial CGWs case observed in northeastward of Japan on October 18, 2012. IMAP/VISI measured an arc-like shaped; partial CGWs pattern around the mesopause (~ 95 km) in the O_2 762-nm airglow emission at 1204 UT. The maximum radius of CGWs was ~ 1400 – 1500 km. Similar patterns were also observed by the all-sky imager at Rikubetsu (43.5°N , 143.8°E) in OI 557.7-nm and OH-band airglow emissions from ~ 1100 – 1200 UT. Horizontal wavelengths of the observed small-scale gravity waves are ~ 50 km (OH-band and OI 557.7-nm) and ~ 67 km (O_2 762-nm). From MTSAT and TRMM data the source is suggested to be a deep convective activity over Honshu island (33°N , 136°E) which likely to be related to a typhoon in the south of Japan. Background winds and temperature on the propagation mechanism were analyzed with MERRA, Wakkanai MF Radar and SABER data. Using atmospheric temperature profiles, we conclude that this long-distance propagation of the waves could be caused by thermal duct in the middle atmosphere in the altitude range of 45 to 110 km. The zonal and meridional wind profiles could produce the arc-like shaped CGWs in which the wind filtering effect plays a role on the suppression of wave propagation in the particular direction.

We also conducted a statistical study using 235 CGW events obtained from 3 years data of IMAP/VISI to clarify the spatial and temporal variability of CGWs in the mesopause. We found the horizontal wavelength ranging from 40 to 250 km and maximum radius of 200 to 3000 km, clearly demonstrating the fact that the small-scale gravity waves can travel for a long distance up to 3000 km. The zonally averaged latitudinal distribution of the CGWs occurrence maximized at mid-latitudes (40°N and

40°S) and minimized at low latitudes (10°S). It is interesting to note that more events were found in the summer hemisphere mid-latitudes, with a rapid transition between northern and southern hemisphere around the equinoxes. Occurrence probability of the CGWs was significantly high during non-solstice months (February-May and August–November) than solstice months (June-July and December-January), suggesting that they are able to survive breaking, critical level absorption and turning level reflection in the middle atmosphere to reach the mesopause region more often during these periods. Information regarding localized regions of high CGW activities seen in the global map and the seasonal variability are useful for the future mesospheric and upper atmospheric studies.

Acknowledgement

This doctoral thesis would have not been written without the help of so many people in so many ways. Thus, the author would like to express her sincere gratitude to everyone who has helped through out her study period.

First of all, the author would like to express the deepest appreciation to the committee chairman as well as her supervisor, Associate Professor Takeshi Sakanoi. The author cannot thank him enough for all the guidance, support and opportunities given to her during her study period.

The author would like to extend her appreciation to the thesis committee members, Professor Takahiro Obara, Professor Yasumasa Kasaba, Associate Professor Isao Murata, Associate Professor Atsushi Kumamoto and Assistant Professor Mitsumu K. Ejiri for their encouragement, insightful comments and difficult questions.

The author sincere thanks also go to Associate Professor Hiroaki Misawa, Associate Professor Naoki Terada, Associate Professor Yuto Katoh, Assistant Professor Fuminori Tsuchiya, Assistant Professor Masato Kagitani and Assistant Professor Hiromu Nakagawa for their support on research and academic life.

Special thanks are extended to Professor Takuji Nakamura, Associate Professor Masaki Tsutsumi, Associate Professor Yoshihiro Tomikawa of National Institute of Polar Research, Associate Professor Yuichi Otsuka of STEL Nagoya University and Associate Professor Akinori Saito of Geophysics Department Kyoto University for their

valuable comments and discussions regarding the research. Special thanks also go to Associate Professor Koji Nishimura of National Institute of Polar Research who has always been patiently teaching the author math and statistics method as well as introducing a new algorithm for data analysis.

The author is indebted to Dr. Mizuki Yoneda for his genuine caring attitude and continuous support both on the daily and academic life. Without his help, it would have been difficult for the author to settle down during her first year in Japan. A special thank is also extended to Assistant Professor Takanori Nishiyama of National Institute of Polar Research who has always been helping the author with administration and schedule arrangement during her stay at NIPR for discussion. The author also thanks Dr. Hajime Kita for his kind helps especially on dealing with Japanese administration document. The author would also thank Dr. Manabu Yagi for helping with IDL programming.

The author is also indebted to all secretaries at PPARC who have always been a great help especially on administration and daily life. The author also grateful to have a very nice and helpful lab mates whose names cannot be mentioned one by one here. The cheerful lab environment helps the author to deal with severe homesick and loneliness.

Finally, the recognition goes to author's mother and brothers, who always encourage her with their gentle words, keeping her strong even in the hardest time. Above all, the author owes it to Almighty God for granting her the wisdom, health and strength to undertake research task and enabling the author to its completion.

Table of Contents

Abstract.....	i
Acknowledgment.....	iv
Table of Contents.....	vi
List of Figures.....	x
List of Tables.....	xix
Chapter I Introduction.....	1
1. Atmosphere Structure and Dynamics.....	2
1.1. The Earth's Atmosphere.....	2
1.2. Atmospheric Gravity Waves.....	5
1.2.1. Equation of Motions	6
1.2.2. Observations of Atmospheric	
Gravity Waves.....	10
1.2.2.1. Radar, Lidar and	
Airglow Observation by	
All-Sky Camera.....	10
1.2.2.2. Remote Sensing Measurements	
from Space	15
1.3. Airglow Emissions	19

1.3.1.	O ₂ (0-0) Atmospheric Band.....	20
1.3.2.	OH Meinel Band (730 nm).....	22
1.3.3.	OI Green Line (577.7 nm)	23
1.4.	Concentric Gravity Waves	25
2.	Purpose of Thesis.....	32
Chapter II	Instrumentation and Data Analysis	35
2.1.	Airglow Emissions Data Observerd by IMAP/VISI and All Sky Camera	36
2.1.1.	IMAP/VISI	30
2.1.2.	Rikubetsu All Sky Camera	42
2.2.	Convective Activity Data from MTSAT, TRMM and WWLLN.....	43
2.2.1	MTSAT.....	43
2.2.2.	TRMM.....	44
2.2.3.	WWLLN	47
2.3.	Background Wind Data from GAIA, MERRA and Wakkanai MF Radar	47
2.3.1.	GAIA.....	48
2.3.2.	MERRA.....	40
2.3.3.	Wakkanai MF Radar.....	50
2.4.	Temperature Profile from SABER Data.....	51
2.5.	Analysis Method.....	52
2.5.1.	Data Analysis of IMAP/VISI	52
2.5.2.	Data Analysis of All-Sky Camera.....	56

Chapter III	Observation Result and Discussion Part I: Case Study	
	Coordinated Observation of IMAP/VISI and an All Sky Camera on Concentric Gravity Wave in the Mesopause	60
3.1.	Observation Results.....	61
3.1.1.	Concentric Gravity Waves Pattern Observed by IMAP/VISI	61
3.1.2.	Concentric Gravity Waves Patterns in OH-band and OI 557.7-nm Image Data at Rikubetsu.....	65
3.2.	Discussion	70
3.2.1.	Relationship between CGWs Patterns and Convection Activity Map.....	70
3.2.2.	Background Profile Condition and Wave Propagation Mechanism	75
3.3.	Concluding Remarks.....	93
Chapter IV	Observation Result and Discussion Part II: Statistical Study	
	3-years of Concentric Gravity Waves Variability in the Mesopause as Observed by IMAP/VISI.....	96
4.1.	Observation Results.....	97
4.1.1.	Occurrence Probability and Characteristics of CGWs	97
4.1.2.	Global, Seasonal and Latitudinal Distribution of CGWs	99
4.2.	Discussion	105
4.2.1.	Comparison with Previous Studies: Occurrence Variability and Global Distribution.....	105

4.2.2.	Explanation of Zonal and Latitudinal Distribution with Background Wind from GAIA Model.....	107
4.3.	Concluding Remarks.....	112
Chapter V	Conclusion.....	113
	References.....	117

List of Figures

1.1.	Typical vertical temperature profile at 35°N showing classification of the Earth's atmosphere. The temperature profile data was obtained from the MSIS-E-90 model website (http://ccmc.gsfc.nasa.gov).....	4
1.2.	Schematic drawing of atmospheric gravity wave coupling from tropopause to mesopause. White circles show the zonal wind during the solstice. Red and yellow arrows are gravity waves and circulation, respectively (modified from <i>Fritts and Alexander</i> , 2003).....	6
1.3.	FM-CW radar images recorded on 14 th October 1999. Record begins at 07:40:20 GMT. Kelvin–Helmholtz waves are between 1500 and 1800 m and between 500 and 600 m. (Courtesy of Stephen Frasier, Univ. of Massachusetts, Amherst.).....	12
1.4.	Vertical cross-section wind speeds scan taken from HRDL as a function of height and horizontal range. Positive winds are away from radar. The data was taken during the CASES-99 experiment at Walnut River in Southern Kansas (38°N, 96°W) [<i>Newsom et al.</i> , 2000].....	14

1.5.	OH and OI airglow all-sky images from Haleakala, Hawaii on 10 th October 1993, 1057 UTC [<i>Taylor et al.</i> , 1995].	14
1.6.	Map showing the location of current all sky camera of OMTI network.....	15
1.7.	Summary of spaced-based observation in nadir and limb-view (modified from <i>Alexander et al.</i> , 2003).	17
1.8.	Modulation of gravity wave in the 4.3 μ m taken from MSX satellite observation [<i>Dewan et al.</i> , 1998].	18
1.9.	Comparison of temperature profiles made with radiosonde and GPS-RO system [<i>Tsuda and Hocke</i> , 2004].	19
1.10.	The volume emission rates of OH, sodium molecular and atomic oxygen [<i>Swenson et al.</i> , 2005; <i>Vargas et al.</i> , 2007].	21
1.11.	Schematic of transitions between various electronic states of molecular oxygen [<i>Greer, et al.</i> , 1987].	23
1.12.	Structure of the metastable levels and the wavelengths of the transitions between these levels for a neutral oxygen atom.	24
1.13.	Schematic sketch showing the convective plume model that explains the concentric gravity waves [<i>Vardas, et al.</i> , 2009].	26
1.14.	CGW moving northeastward observed on October 3, 2002 from Shigaraki (a). The hodograph of background wind from 12:00-16:00 UT showing the direction of the wind in the 96 km changing from northeastward to southwestward [<i>Suzuki et al.</i> , 2007].	28

1.15.	CGW temperature perturbations at $z = 87$ km with the propagation time at $t = 50, 90,$ and 120 min (a,b,c, respectively) with the July zonal wind and (d) the zonal wind data obtained from HAMMONIA-GCM [<i>Vadas et al.</i> , 2009].	29
1.16.	CGWs event generated by volcanic eruption observed by Suomi/DNB data reported by <i>Miller et al.</i> , 2015.	30
1.17.	Geographic distribution of ring centers during January 2010 on (a) ascending and (b) descending orbits. The dot size is linearly proportional to wave amplitude, which varies from 1 to 5 K. Color corresponds to estimated phase propagation direction, with positive (negative) values meaning clockwise (counterclockwise) from the North. Arrows are MERRA monthly averaged wind vectors at 2.5 hPa. Thick black contours represent proxies of tropical deep convection.....	31
1.18.	A Diagram showing a summary of the past studies of CGWs (solid line) versus the studies that will be covered in this thesis (dashed line).....	37
2.1.	Schematic drawing of the FOVs of IMAV/VISI mapped on the emission layers [<i>Sakanoui et al.</i> , 2011]	30
2.2.	Top: First light (a CCD full-frame image) of IMAV/VISI obtained with the calibration mode on August 13, 2012. The horizontal axis is the wavelength and the vertical axis is the zonal direction. Each ROIs are shown in forward and backward FOVs. Bottom: the spectral profile estimated by integrating counts along a column of the CCD frame. The horizontal axis is the wavelength in nm and the vertical axis shows the count [courtesy of T. Sakanoui].	39

2.3.	An example of O ₂ (762 nm) data on April 16, 2014 around 17 UT. Concentric gravity waves can be seen in both FOVs. Red arrow shows the direction of the ISS movement.	41
2.4.	Forward FOV O ₂ (762 nm) airglow emission on April 16, 2013 projected onto geographical coordinate by assuming the altitude of the airglow layer was ~95 km.	41
2.5.	4-days plot of IMAP/VISI data on April 1-4, 2013. The plot showing the latitudinal coverage of the IMAP/VISI data. The color bar shows the intensity of the data in Rayleigh [R].	42
2.6.	The convective index derived from the TBB data of MTSAT satellite at 1100 UT on 18 October 2012. The color bar shows the hourly convective index derived from the top-cloud temperature of MTSAT-R1 data.	45
2.7.	An example of global precipitation data obtained from Giovanni TOVAS on March 31, 2013 at 0000 UT.	46
2.8.	One-day global lightning occurrences from WWLLN data. The map shows data on September 1, 2013.	49
2.9.	Global map of zonal wind data at an altitude of 95 km of GAIA model on March 30, 2013. The color bar indicates the zonal wind speed in m/s... ..	49
2.10.	Zonal-mean zonal wind data from MERRA on March 1, 2013. The plot shows the latitudinal distribution as a function of pressure level. The color bar indicates the wind speed in m/s where positive values show the eastward wind.	50
2.11.	Latitudinal distribution of kinetic temperature of SABER data on February 09, 2013 as a function of altitude. The color bar shows the kinetic temperature in K.	52

2.12.	Circle fitting applied to the CGWs event on 16 April 2013 at 1700 UT. The X mark shows the center of the wave as a result of circle fitting. The black arrows represent the radius from the estimated center to each wave front. The maximum radius (R_{\max}) shows the distance from the estimated center to the outermost ring. The color bar shows the 3-hourly precipitation rate from TRMM data (1330-1630 UT).....	55
2.13.	Estimation of horizontal wavelength from the calculated rings. The crosses indicate the radii of the best fitting set of wavefronts.....	56
2.14.	An example of the raw image of OI 557.7-nm, taken at Rikubetsu at 1102 UT on 18 th October 2012. (b) Same as (a), except that it was projected onto the geographical grid with a size of 512×512 km.....	58
3.1.	The CGWs event in O ₂ (762 nm) airglow emission obtained by IMAP/VISI during the period of 1203-1232 UT on October 18, 2012. The red arrow shows the direction of the ISS orbit.....	62
3.2.	The backward FOV of IMAP/VISI data at 1203 UT and 1336 UT on October 18, 2012 mapped on to geographic coordinate. Dashed lines indicate the best fitted round circle to the circular wave fronts. The estimated center of the circle is indicated by the cross mark. The red arrow represents the outer radius of the circle from the expected center (~1400 km). The diamond marks show the location of the Rikubetsu all sky camera and the Wakkanai MF radar.....	64
3.3.	Sequential images of OH-band (top) and OI 557.7-nm emission (bottom) showing the deviation of 1-hour running average during the period of 1103– 1159 UT. The emissions were mapped by assuming that the airglow layer of OH-band is ~86 km and OI 557.7-nm is ~96 km.	66

3.4.	Mapped airglow images, fitted circles and estimated center positions (cross mark) for OH data (a) and OI 557.7-nm data (b) of the CGWs event on October 18, 2012.	68
3.5.	The convective index derived from the TBB data of MTSAT satellite at 1100 UT on October 18, 2012 (a). Dash-dotted line represents an approximate circle fitted to the CGW pattern, and a cross mark is its center. (b) TRMM data at 0600 UT plotted together with CGWs even in O ₂ 762-nm and location of SABER data available during the event.....	73
3.6.	The precipitation data (mm/hr) from the TRMM satellite during the period from 0000 to 1500 UT, October 18, 2012.....	74
3.7.	Zonal wind profile obtained from MERRA data over the expected center (33°N, 143°E) (0-60 km) at 0600 UT (black dashed line) and over Wakkanai (45°N, 141°E) at 1200 UT (red dashed line). Zonal wind profile obtained from Wakkanai MF Radar (84-102 km) at 1200 UT is shown in solid red line.	76
3.8.	Background wind profile obtained from MERRA: (a) Zonal wind speed from 0-60 km at the latitude of 33°N with longitude from 134° to 144°E, (b) meridional wind speed from 0-60 km at longitude of 143°E with latitude from 28° to 38°N, (c) contour of zonal wind speed and (d) contour of meridional wind speed at the altitude of 60 km.....	77
3.9.	Vertical profile of m^2 calculated using the dispersion relationship for the background wind speed ranging from -60 to 60 m/s.....	79

3.10.	(a) Zonal wind profiles in the MLT region derived from the MF radar at 1000-1200 UT on October 18, 2012. Eastward wind is positive. (b) Meridional wind profiles at 1000-1200 UT from the Wakkanai MF Radar.	81
3.11.	Hodographs at altitudes of OH emission layer at 86 km (solid line) and O ₂ emission layer at 95 km (dashed line) for 1000-1300 UT. Positive meridional wind means northward, and positive zonal wind means eastward.	83
3.12	Background winds and squared vertical wavenumber analysis for 5 July 2003 small-scale gravity wave event reported by <i>Sikhamda et al.</i> , 2009 (top), which shows a strong wind inversion in the opposite direction of the wave propagation that lead the negative value of m^2 at ~87 km and ~97 km forming a duct region. The model simulation for the same event depicts upward wave propagation through the mesopause region (bottom).....	84
3.13.	Altitude profiles of m^2 showing two duct regions in stratosphere and lower atmosphere [<i>Waltherscheid et al.</i> , 2001].....	88
3.14.	Schematic of simulation study reported by <i>Snively et al.</i> , 2008 (top) showing the linear coupling between stratospheric and lower-thermospheric ducts (top). Three bottom images show the vertical perturbation velocity depicting (a) stratospheric ducted wave excitation, (b) vertical propagation into thermosphere and (c) ducted wave propagation in both stratospheric and thermospheric ducts.....	89

3.15.	(a) Brunt-Väisälä frequency profile derived from the temperature profile of SABER data for event number 40 (black dashed-line) and event number 41 (red dashed-line). (b) Altitude profile of m^2 for SABER data event number 40 (black dashed-line) and number 41 (red dashed-line)....	92
3.16.	Plausible scenario of propagation mechanism of partially CGWs seen in O ₂ (762 nm) airglow emission on October 18, 2012.....	95
4.1.	a) Monthly path number from January to December. Red, black and green are 2013, 2014 and 2015, respectively. (b) Monthly occurrence number of the CGWs. (c) Distribution of horizontal wavelength. Horizontal wavelength of 60-150 km is dominant. (d) Distribution of the maximum radius shows the majority of the CGWs travel a distance of 600-1800 km from its center.....	100
4.2.	The same with Figure 4.1, except in these figures show the distribution of occurrence rate (b), horizontal wavelength (c) and (d) maximum radius in northern and southern hemisphere.....	101
4.3.	(a) Global distribution of CGWs occurrence during the period of 2013 to 2015. (b) Zonally averaged latitudinal distribution of CGWs event number which shows maxima at 40°N and 40°S and minimum at 10°S...	103
4.4.	(a) Latitudinal distribution of event number from January to December and (b) transition of CGWs occurrence between northern and southern hemisphere before and after the equinoxes	104
4.5.	Transition of CGWs occurrence between northern and southern hemisphere before and after the equinoxes on February-March to April May seen in the latitudinal distribution profile (top) and global map (bottom).....	104

4.6.	Same as Figure 4.5, except for transition seen between August-September and October-November.....	105
4.7.	Occurrence variability comparison between ground-based observation at (a) Yucca Ridge [Yue <i>et al.</i> , 2009] and (b) IMAP/VISI (present study)....	106
4.8.	Latitudinal distribution of zonal-mean zonal wind from the GAIA data between 10-95 km. The solid line represents the minimum wind (westward wind) and dashed line represents the maximum wind (eastward wind). The Blue shaded region indicates the critical level region. The waves with horizontal phase speed (c_x) $> \pm 50$ m/s can avoid the critical level filtering.....	110
4.9.	Latitudinal distribution of zonal-mean zonal wind from the GAIA data between altitude range of 10-95 km on solstices (Dec-Jan and Jan-Jul) and equinoxes (Feb-May and Aug-Nov).....	111

List of Tables

2.1.	Detail specifications of IMAP/VISI.....	37
2.2.	Summary of scientific targets of IMAP/VISI.....	38
2.3.	Filters, typical exposure time and sensitivity for the Rikubetsu all-sky camera [<i>Shiokawa et al</i> , 2000].....	43
2.4.	TRMM-precipitation related instruments.....	46
2.5.	Specification of Wakkanai MR radar [<i>Igarashi et al.</i> , 1999].....	51
3.1.	SABER data on October 18, 2012 near the expected center around the time of the wave generation. All values reference to the 90 km tangent point.....	90

Chapter 1

Introduction

This chapter introduces the basic knowledge of the middle atmospheric dynamic to facilitate the understanding of physical processes discussed later in this thesis. The introduction begins with a brief description of the Earth's atmosphere. Following description of different atmospheric layers explains the fundamental theory of atmospheric gravity waves (AGWs) and its importance on the dynamic of middle and upper atmosphere. The introduction continues with a various observation techniques of AGWs. Since the main topic of this thesis is the observation of concentric gravity waves (CGWs) in airglow emission, here we describe a section on the modulation of AGWs in the airglow emission and a specific section on CGWs studies. We present the purpose of this thesis in the last section of this chapter.

1. Atmosphere Structure and Dynamics

1.1. The Earth's Atmosphere

The Earth's atmosphere is defined on the basis of the vertical temperature structure. From the bottom of atmosphere, it is divided into the troposphere, stratosphere, mesosphere and thermosphere regions. **Figure 1.1** shows the typical vertical temperature profile at geographical latitude of 35° N, which displays four regions of the Earth's atmosphere; troposphere, stratosphere, mesosphere and thermosphere.

Troposphere is the lowest region of the Earth's atmosphere, begins from the ground to about 15 km. In this region, usually categorized as the lower atmosphere, most of the meteorological phenomena occur. As the density of the gases decrease with height, the air becomes thinner and the temperature decreases with height as a result. The upper boundary of this layer is called the tropopause. At the tropopause height, the temperature reaches the minimum, with an average of 210 K. The height of the tropopause varies with season and latitude where the peak is at Equator (~17 km) and reaches minimum height over the poles (less than ~6 km).

The region above the tropopause up to ~50 km is called the stratosphere. In this region, the temperature rises with height because of the heating by solar ultraviolet absorption by the ozone layer. The upper boundary of stratosphere is called the stratopause. At this layer, the maximum temperature reaches 300 K.

The mesosphere is the region at altitude range of 50-80 km where the temperature decreases again. The temperature decreases because the heating by ozone layer falls off and the CO₂ radiative emission gives a cooling effect in this region. The thermal effect caused by the dynamical motions such as breaking of

gravity wave should also be taken into account. The top of the layer (~90 km) where the temperature reaches minimum (~173 K) is called the mesopause. The region from stratosphere to mesopause is classified as middle atmosphere.

The region beyond the mesopause is called the thermosphere, which usually classified as the upper atmosphere. The thermosphere is the region right above the mesopause when the temperature begins to rise again because of the reduced radiative cooling combined with heating by absorption of UV and EUV radiation mainly by O₂, O and N₂. This region extended from ~90 km to ~500 km and the temperature reaches 500-1200 K at 200 km. In this region, the E and F regions of the ionosphere exist. The upper boundary of this region is called the thermopause.

The exosphere is the region above the tropopause and the uppermost part of the Earth's atmosphere, where the air is extremely thin and gradually fades into space. Although this region is technically part of the Earth's atmosphere but not all scientists agree that the exosphere is part of the atmosphere, they think that the exosphere is part of space.

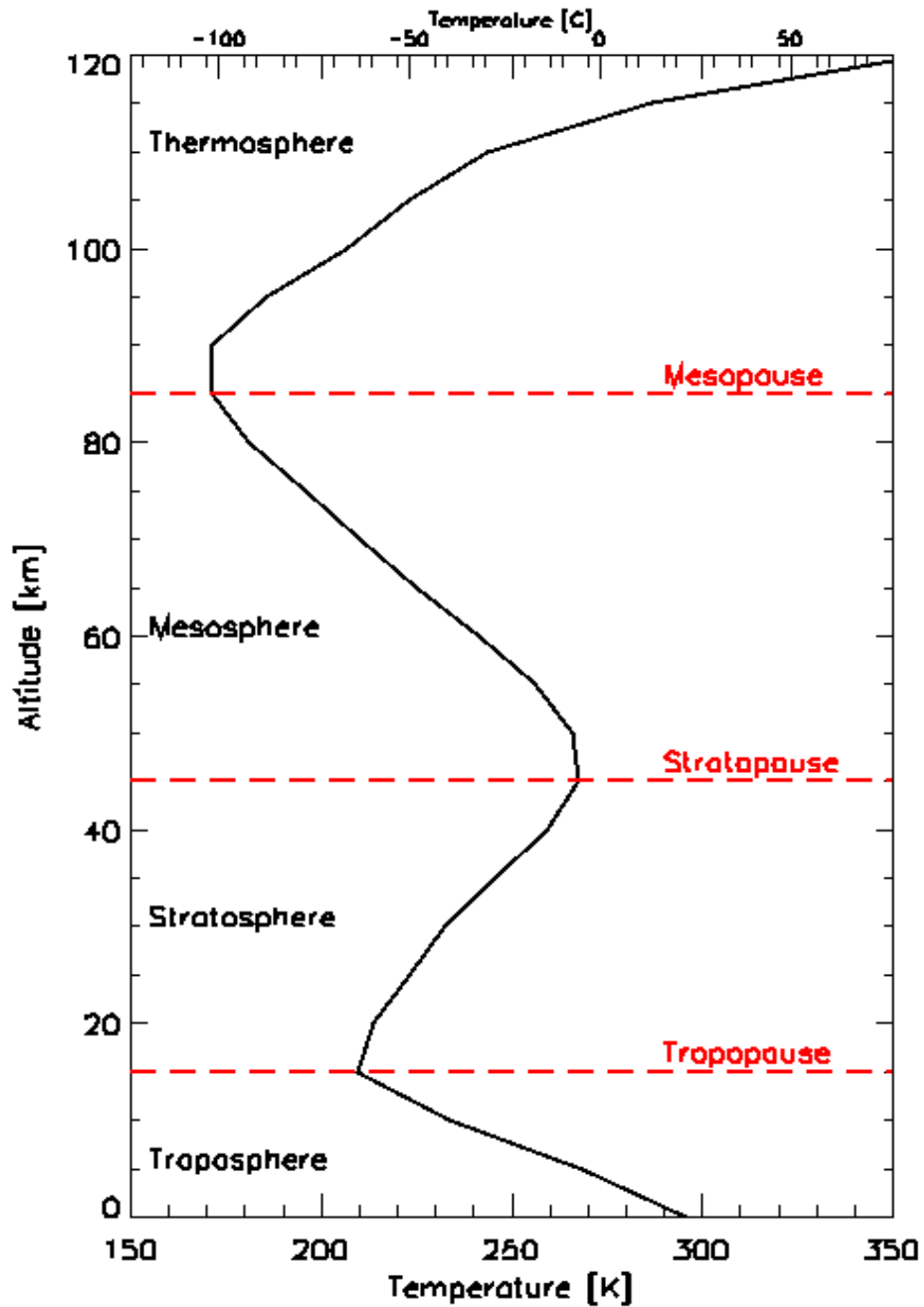


Figure 1.1. Typical vertical temperature profile at 35°N showing classification of the Earth's atmosphere. The temperature profile data was obtained from the MSIS-E-90 model website (<http://ccmc.gsfc.nasa.gov>).

1.2. Atmospheric Gravity Waves

Dynamical processes in the middle and upper atmosphere are heavily influenced by various atmospheric waves. These waves have typical period ranging from days (planetary waves), ~24 hours (tidal waves) and minutes to several hours (gravity waves) [e.g. *Kato, 1966; Lindzen, 1967; Madden and Julian, 1972; Holton, 2004; Nappo, 2002; Fritts and Alexander, 2003*]. These waves can propagate upward and their amplitudes increase with height until their amplitudes become very large, these waves are damped and then transfer their energy and momentum to their background [e.g. *Lindzen, 1981; Nakamura et al., 1996; Fritts and Alexander, 2003*]. This energy and momentum transfer is contributing in turbulence and mixing, also influencing the mean circulation and thermal structure in the middle atmosphere [e.g. *Matsuno, 1982; Fritts and Rastogi, 1982; Fritts, 1984; Fritts and Alexander, 2003*]. Although all the waves are superimposed on the mean winds, however gravity waves are the major influence for the dynamic in the middle and upper atmosphere [e.g. *Holton et al., 1982; Nakamura et al., 1993; Fritts and Alexander, 2003*]. **Figure 1.2** shows the schematic drawing of AGWs driving of the middle atmosphere transport circulation.

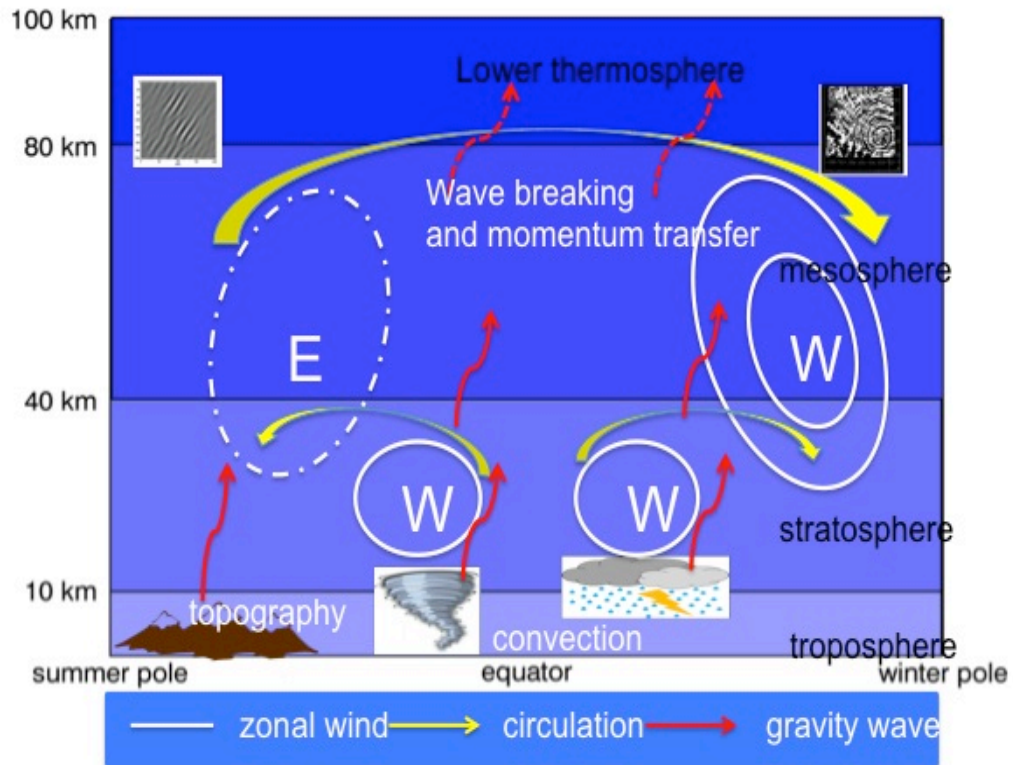


Figure 1.2. Schematic drawing of atmospheric gravity wave coupling from tropopause to mesopause. White circles show the zonal wind during the solstice, W represents westerly wind (eastward wind) and E represents easterly wind (westward wind), respectively. Red and yellow arrows are gravity waves and circulation, respectively (modified from *Fritts and Alexander, 2003*).

1.2.1. Equation of Motion

The fundamental theory of AGWs is described in this section, assuming the atmosphere to be an ideal gas. The linear theory is generally used to study the atmospheric gravity waves (AGWs) because this system is more simple and understandable.

The equation of motion of an air parcel that is displaced vertically, assuming that the process is adiabatic is expressed as [Nappo, 2002]:

$$\frac{d^2(\delta z)}{dt^2} = -\frac{g}{\rho_0} \frac{\partial \rho_0}{\partial z} \delta z \quad (1.1)$$

where g is the acceleration of gravity and ρ_0 is the initial density of the air parcel. This equation expresses a simple harmonic motion in the vertical direction. If the air parcel is displaced vertically and then released, the solution of Equation (1.1) can be expressed as

$$\delta z(t) = Ae^{iNt} + Be^{-iNt} \quad (1.2)$$

where A and B are constant, and N is the frequency of the oscillation of the air parcel and is called as the Brunt-Väisälä frequency given by

$$N = \sqrt{\frac{g}{\rho_0} \frac{\partial \rho_0}{\partial z}} \quad (1.3)$$

The vertical motion is possible only when N is positive. If the N is imaginary, then the equation (1.2) represents the convective instability [Nappo, 2002; Holton, 2004].

The Taylor-Goldstein equation [Taylor, 1931; Goldstein, 1931] forms the basis wave equation for linear gravity waves, assuming the perturbations like turbulence, zonal winds, thermal plumes and density currents are much smaller than the background mean values; therefore the perturbations do not affect the background state.

This linear theory is applied according to

$$q(x, z, t) = q_0(z) + q_1(x, z, t), \quad (1.4)$$

where $q(x, z, t)$ is the perturbation in the atmosphere, $q_0(z)$ is a steady, horizontally uniform background value and $q_1(x, z, t)$ is a first-order perturbation value.

The Taylor-Goldstein equation is then expressed as

$$\frac{d^2 \hat{w}}{dz^2} + \left[\frac{k^2 N^2}{\Omega^2} + \frac{k d^2 u_0}{\Omega dz^2} - k^2 - \frac{k}{\Omega H} \frac{du_0}{dz} - \frac{1}{4H^2} \right] \hat{w} = 0 \quad (1.5)$$

where \hat{w} represents the wave equation for linear gravity waves, $\Omega = (\omega - u_0 k)$ is the intrinsic frequency relative to the flow, ω is the wave frequency observed in a fixed coordinate system, k is the horizontal wave number u_0 is the background wind and H is the scale height.

Assuming a constant background wind where the wind speed, u_0 , is the component of the background wind velocity in the direction of wave propagation.

The Taylor-Goldstein equation is now

$$\frac{d^2 \hat{w}}{dz^2} + \left[\frac{k^2 N^2}{(\omega - u_0 k)^2} - k^2 - \frac{1}{4H^2} \right] \hat{w} = 0 \quad (1.6)$$

The intrinsic phase speed is given as $(c - u_0) = \frac{\Omega}{k}$. The vertical wavenumber m then can be written as

$$m^2 = \frac{N^2}{(c - u_0)^2} - k^2 - \frac{1}{4H^2} \quad (1.7)$$

where c is the apparent phase speed of the wave. If we replace the bracketed part in Equation (1.6) with m^2 , then

$$\hat{w}'' + m^2 \hat{w} = 0 \quad (1.8)$$

The general solution is

$$\hat{w}(z) = Ae^{imz} + Be^{-imz} \quad (1.9)$$

This is the basis of linear AGWs theory. Equation (1.7) indicates the dispersion relation relates the wave frequency to the wave's spatial characteristics (wave numbers) and to the background atmosphere properties (N and u_0). If $m^2 > 0$, the gravity waves transport the energy vertically and this energy-transport is usually referred as internal or propagating. On the other hand, if the $m^2 < 0$, the waves do not propagate vertically and usually referred as evanescent. However, there are cases where the waves propagate vertically ($m^2 > 0$) but having evanescent layer above and below. These waves are trapped or ducted [e.g. *Nappo, 2002; Fritts and Alexander, 2003*]

The background wind also affects the polarization equations given by [*Nappo, 2002*]

$$i\Omega \hat{u} - \hat{w} \frac{du_0}{dz} = \frac{i}{\rho_0} k \hat{p} \quad (1.10)$$

where \hat{u} is the wind perturbation and \hat{p} is the background pressure. For constant

background wind and $\Omega/k = (c - u_0)$ the equation becomes

$$\hat{u} = \frac{\hat{p}}{\rho_0(c - u_0)} \quad (1.11)$$

Thus, if $c > u_0$, the pressure and wind speed perturbations are in phase, but if $c < u_0$, then the perturbations are 180° out of phase.

1.2.2. Observations of Atmospheric Gravity Waves

The previous section mostly describes the theoretical issues of the AGWs. This theoretical knowledge is useful for analyzing data and understanding the wave characteristic, i.e., amplitude, wavenumber, frequency and dispersion from the observations. The observations of the AGWs in the upper atmosphere have been made from ground and space for the last three decades. AGWs have broad and multidimensional spectrum, makes it difficult for one single technique of observation to observe the whole spectrum of AGWs since one observation technique is sensitive to a particular spectrum while totally insensitive to other portions. Section below is a summary of various techniques used to observe the AGWs. From ground-based method, radar, lidar and all-sky camera have been used, while satellites and Global Positioning System (GPS) have been used for space-based observation.

1.2.2.1. Radar, Lidar and All-Sky Airglow Imager Observations

A radar experiment has been extensively used to study gravity waves from the lower atmosphere up to mesosphere and lower thermosphere region. However the

observation usually limited in a few sites and on short-time campaign basis. It was started by *Ottersten, et al.* [1973] using sodar data with a carrier frequency of 950 Hz to describe gravity wave observations in the planetary boundary layer (lowest part of troposphere extending from the ground up to 100-3000 m). *Gauge and Balsley* [1978] described probing of the troposphere and stratosphere by using a VHF (Very High Frequency) radar operates at a frequency of 53 MHz. *Manson* [1990] presented a climatology wave structure in the mesosphere by using MF radar data at Adelaide and Saskatoon which operate at a frequency of 1.98 MHz and 2.2 MHz, respectively. *Fritts and Isler* [1994] described wave motions in the mesosphere and lower thermosphere from MF radars data at Hawaii and Christmas Island. *Vincent and Reid* [1983] used these techniques to measure gravity wave momentum fluxes in the mesosphere. At a height range of 80–90 km, *Vincent and Reid* [1983] calculated a westerly acceleration due to momentum flux convergence of about 20 m/s per day due to waves with a dominant wavelength of about 50 km and a phase speed of about 50 m/s. The gravity waves kinetic energy as well as the wind variances $\left(\overline{u'^2}, \overline{v'^2}, \overline{w'^2}\right)$ studies, where u , v and w are zonal, meridional and vertical wind directions, have shown a semiannual variation with maxima in summer and winter and minima in spring and fall [e.g. *Tsuda et al.*, 1990; *Nakamura et al.*, 1996]. **Figure 1.3** shows an example of the Frequency Modulated-Continuous Wave (FM-CW) radar echoes taken during the CASES-99 field program [*Poulos et al.*, 2001], which illustrates the fine wave-like structures that can be revealed by radar measurement.

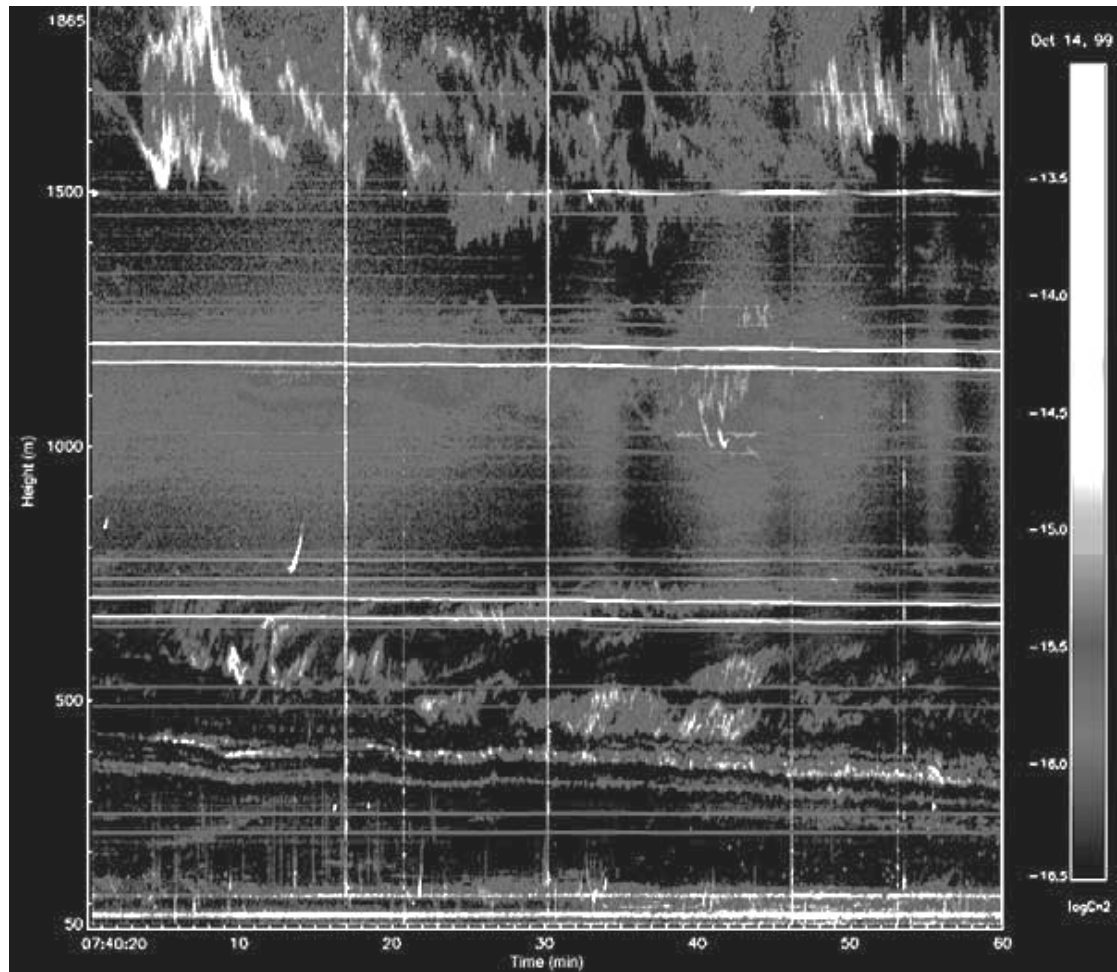


Figure 1.3. FM-CW radar images recorded on 14th October 1999. Record begins at 07:40:20 GMT. Kelvin-Helmholtz waves are between 1500 and 1800 m and between 500 and 600 m. (Courtesy of Stephen Frasier, Univ. of Massachusetts, Amherst.)

On contrast with extensively radar observation, lidar (light detecting and ranging) observation of gravity waves in the middle atmosphere is restricted to a few specific sites. The monthly average of the data shows a seasonal cycle, maximum in winter and minimum in summer [e.g. *Wilson et al.*, 1991; *Marsh et al.*, 1991; *Mitchell et al.*, 1991; *Whiteway and Carswell*, 1995]. These studies observe AGWs

with the vertical wavelength down to 1 km at altitudes in the upper stratosphere and lower mesosphere from Rayleigh radar observations at mid-latitudes. **Figure 1.4** shows an example of gravity waves observation from High Resolution Doppler lidar during the CASES-99 campaign reported by *Newsom et al.* [2000].

Radar and Lidar observations provide one-dimensional (1 D) data where observation using an imager can provide 2-dimensional (2 D) data. In the upper atmosphere between 80-120 km, the gravity waves can be seen in the modulation of airglow emission. Common airglow emissions observations for gravity waves study are atomic oxygen (OI) at 557.7 nm, sodium (Na) at 589 nm, and the hydroxyl radical (OH) at 600–2000 nm. Each of these emissions occurs at a particular altitude (~95 km for OI, ~92 km for Na and ~85 km for OH) with a thickness of 10–20 km [Swenson and Gardner, 1998]. Because the intensity of the photochemical emission is proportional to the local neutral and electron density and also the temperature, variations in intensity can be related to variations in density and temperature. It is now widely accepted that these variations are due to gravity waves [e.g. *Molina*, 1983; *Hecht et al.*, 1997; *Fritts et al.*, 1997, *Nakamura et al.*, 2003]. **Figure 1.5** shows an example of airglow distribution caused by the AGWs taken at Haleakala reported by *Taylor et al* [1995].

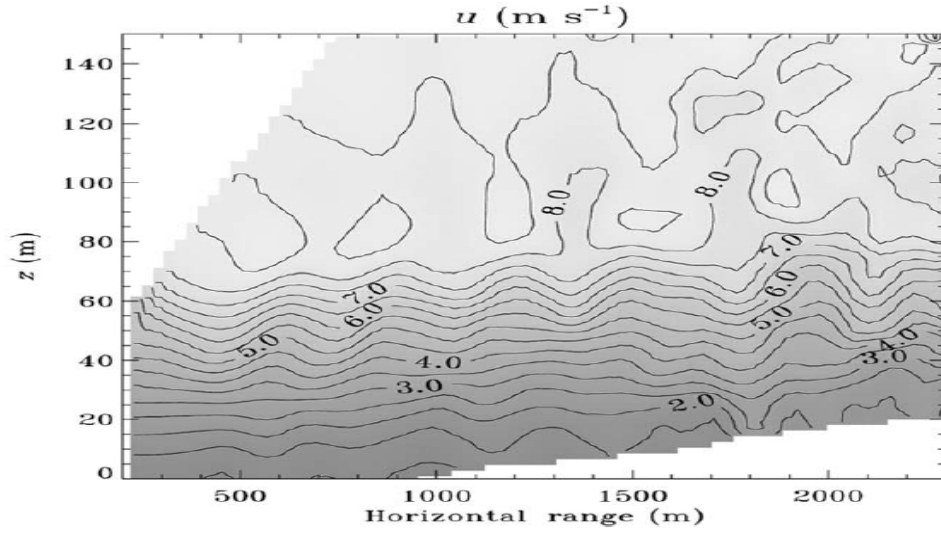


Figure 1.4. Vertical cross-section wind speeds scan taken from HRDL as a function of height and horizontal range. Positive winds are away from lidar. The data was taken during the CASES-99 experiment at Walnut River in Southern Kansas (38°N , 96°W) [Newsom *et al.*, 2000].

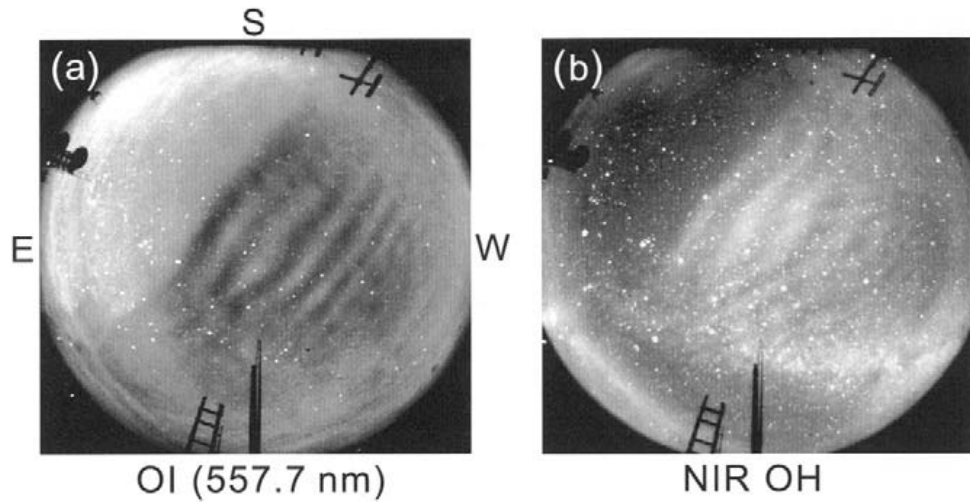


Figure 1.5. (a) OH and (b) OI airglow all-sky images from Haleakala, Hawaii on 10th October 1993, 1057 UTC [Taylor *et al.*, 1995].

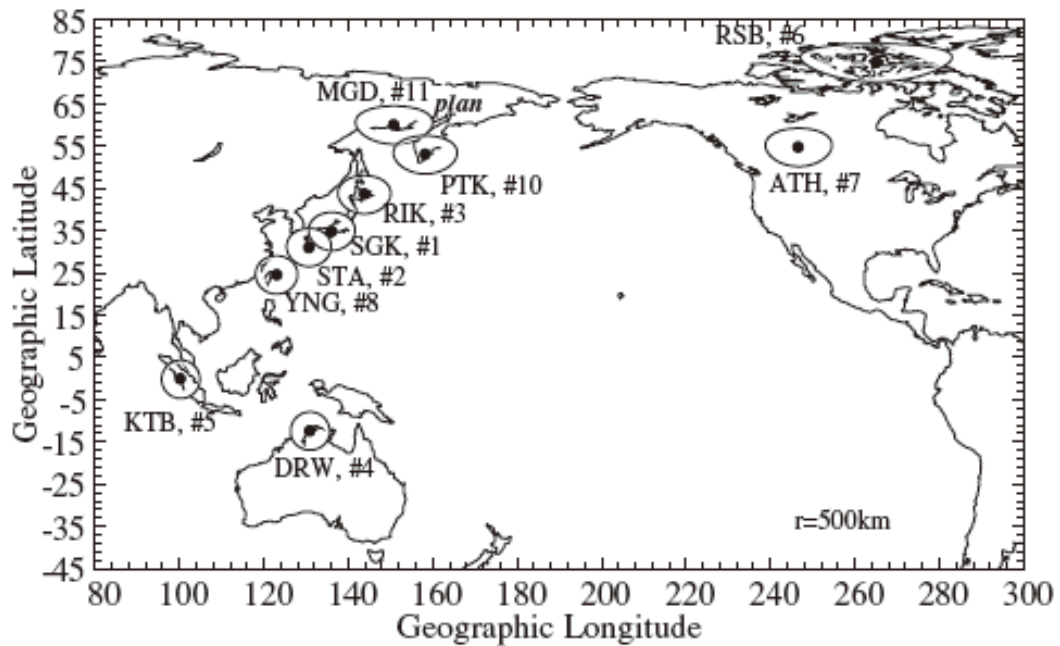


Figure 1.6. Map showing the location of current all sky camera of OMTI network.

An attempt to study the gravity waves over different latitudes has been made by installing an airglow imager network. One example is the OMTI network operated by Nagoya University. **Figure 1.6** shows the location of OMTI all-sky imager installation [Shiokawa *et al.*, 1999].

1.2.2.2. Remote Sensing Measurements from Space

The modulation of AGWs in the airglow emissions can also be observed using the satellite-borne optical instrument from space. Observation from the space can provide a global view of gravity waves variations. The observations were mainly conducted in a limb-view of the Earth; revealed the vertical structure of the airglow emissions. The advantages of the limb measurement are that the contaminations due

to the reflections of moonlight on cloud-top can be negligible and the intensity increases by integrating along the line-of-sight direction. However, this type of observation does not have a good horizontal resolution, in which the small-scale waves (which is believed to be more important in the middle atmosphere dynamic) cannot be observed. Limb Infrared Monitor of the Stratosphere (LIMS) was launched to retrieve the temperature profile in the altitude range of 15-60 km [Fetzer and Gille, 1994]. Maps of gravity wave temperature variance have been similarly derived from Cryogenic Infrared Spectrometers and Telescopes for the Atmosphere (CRISTA) data [Preusse *et al.*, 1999]. The most recent limb-view observation was conducted by HIRDLS (High resolution Dynamics Limb Sounder) [Hays *et al.*, 2003].

Another type of satellite observation is the nadir-view measurement, which provides a high spatial resolution, makes it possible to observe the small-scale AGWs. AIRS observation provides a global map of AGWs variability in the stratosphere (Hoffman *et al.*, 2013, Gong *et al.*, 2015). The most recent state of art space-based nadir-imaging measurement is conducted by IMAP/VISI [Sakanoi *et al.*, 2011; Akiya *et al.*, 2014; Perwitasari *et al.*, 2015] and Suomi/DNB instrument [Miller *et al.*, 2015].

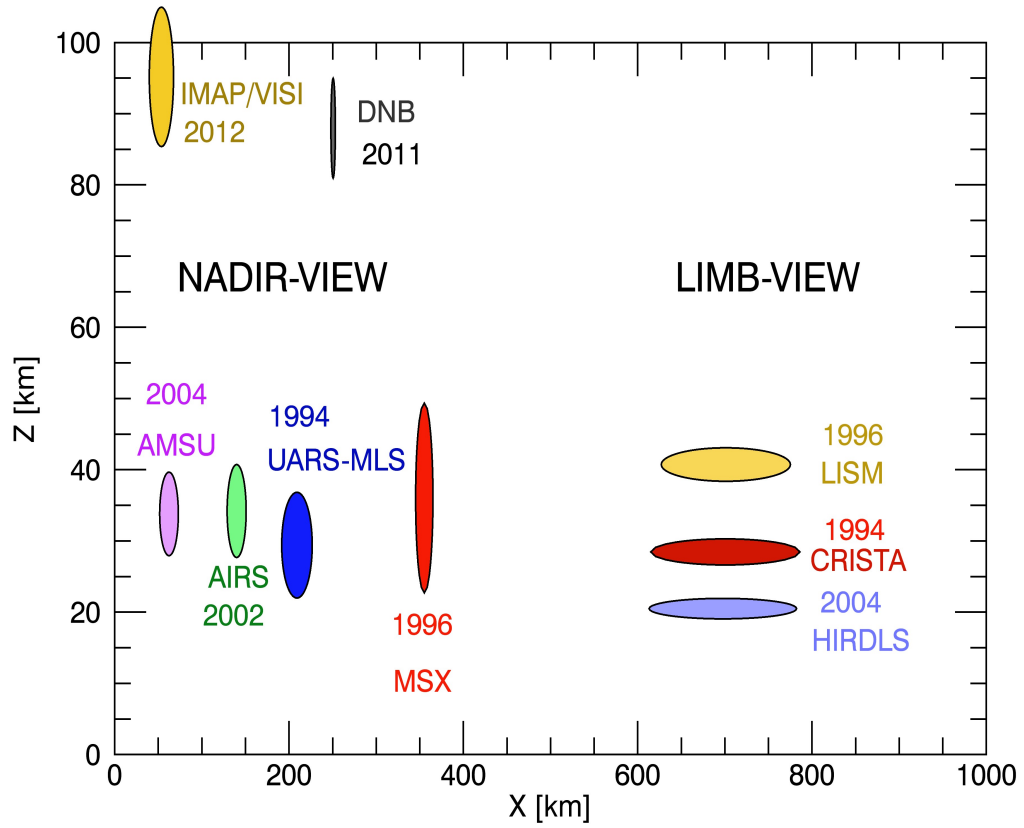


Fig. 1.7 Summary of spaced-based observation in nadir and limb-view (modified from *Alexander et al.*, 2003).

IMAP/VISI could observe the AGWs modulation in the nightglow emission with a horizontal resolution ~ 14 - 16 km for O_2 at 762 nm. On the other hand, the Suomi/DNB instrument can observe a fine structure with a horizontal resolution down to ~ 700 m. **Figure 1.7** demonstrates the summary of space-based observation in limb and nadir view and **Figure 1.8** shows the gravity wave modulation seen in O_2 atmospheric band emission at 762 nm obtained with the MSX satellite [*Dewan et al.*, 1998].

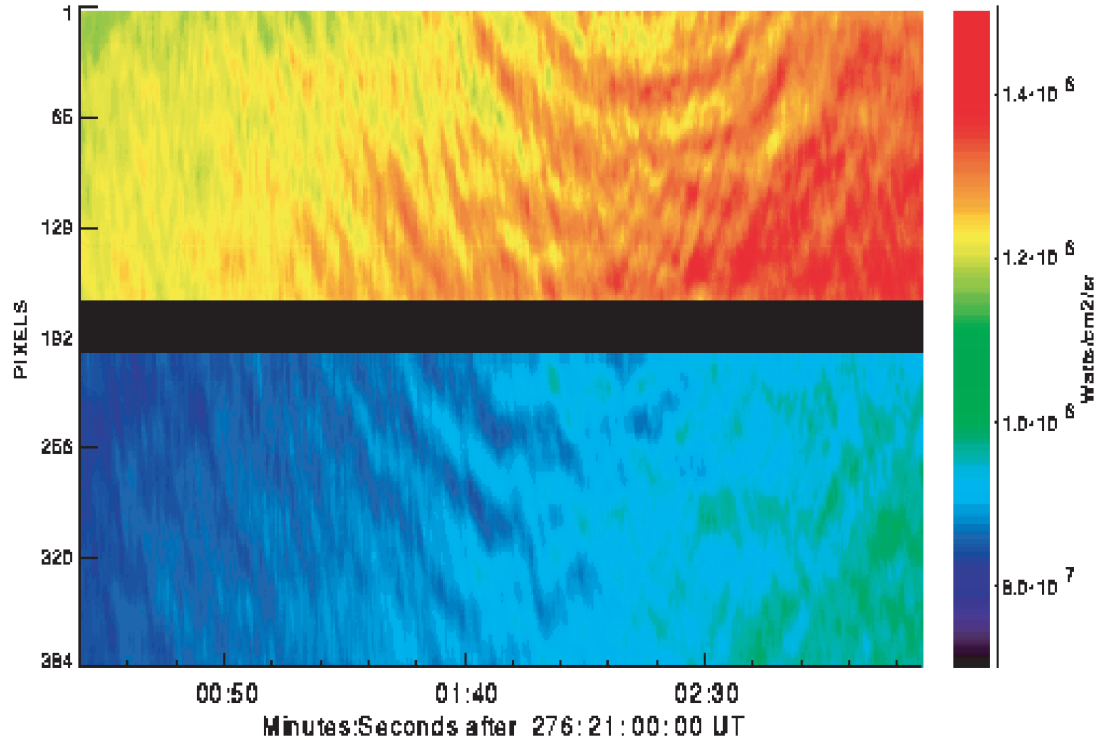


Figure 1.8. Modulation of gravity wave in the $4.3\mu\text{m}$ taken from MSX satellite observation [Dewan *et al.*, 1998].

In the past decade, the Global Positioning System (GPS) has been used to study the atmosphere [e.g., Tsuda *et al.*, 2000]. With the advent of the GPS, it is now possible to make near-continuous soundings of the lower and middle atmospheres. Tsuda and Hocke [2004] reported a comparison of tropical temperature profiles, above Indonesia, measured with a radiosonde and radio-occultation (RO) system. The RO profile shown in **Figure 1.9** shows that the wave activity above the tropopause continues far past the height of the radiosonde profile ends (~ 40 km). GPS-RO is useful even in the upper atmosphere, except for the ionosphere, because the density decreases at the upper atmosphere.

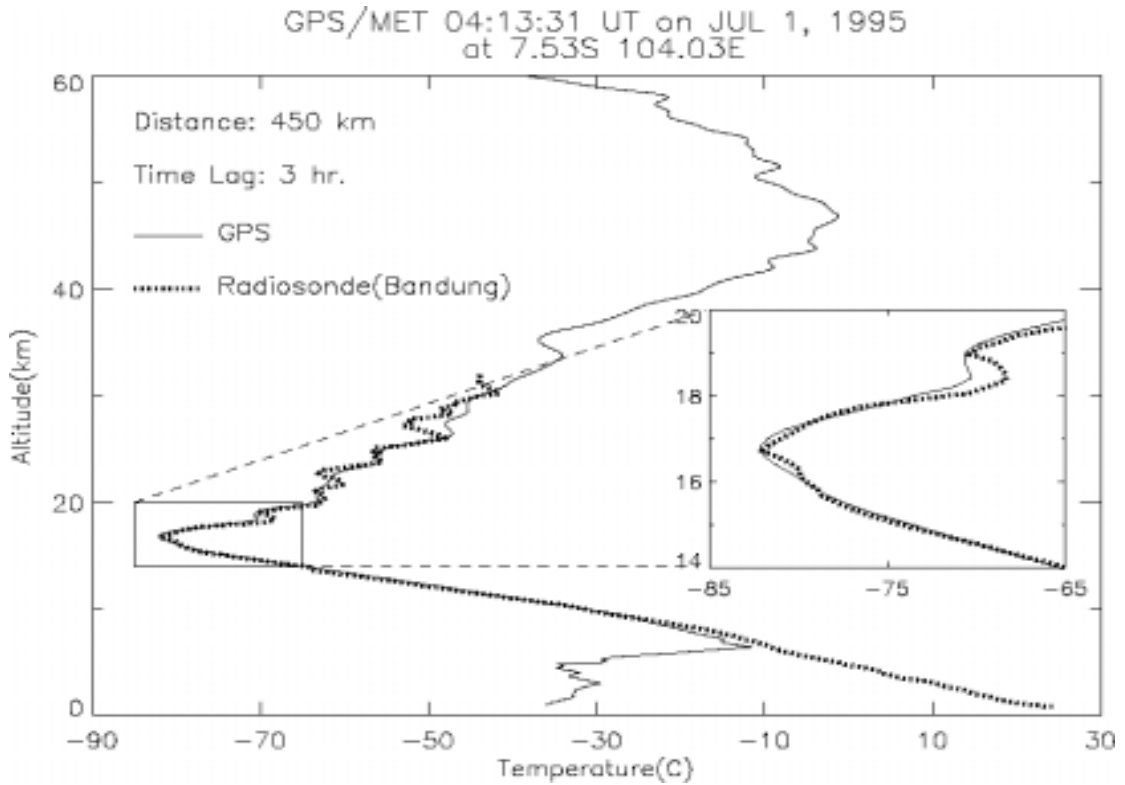


Figure 1.9. Comparison of temperature profiles made with radiosonde and GPS-RO system [Tsuda and Hocke, 2004].

1.3. Airglow Emissions

As already mentioned in the previous section, the gravity waves can modulate the airglow emissions. The passage of AGWs can change the density of the chemistry in the airglow layer, resulting the change of the intensity. There are three major classes of visible and near-infrared airglow emissions in the mesosphere and the lower thermosphere (MLT) region: (1) the vibrational-rotational bands of OH, (2) the atomic and molecular emissions of oxygen, and (3) the emissions of metallic atoms such as sodium, calcium, potassium, and magnesium. The following sub-sections

describe in further detail on the emissions that will be used in this study: OH band, molecular (O_2) and atomic (OI) emissions of oxygen. **Figure 1.10** shows the volume emission rates of OH, sodium, molecular and atomic oxygen as a function of height in the MLT region.

1.3.1 O_2 (0-0) Atmospheric Band

One of the bright emissions in the molecular oxygen atmospheric band spectrum is the O_2 (0-0) A-band at 762 nm. Most rocket investigations have shown that the O_2 A-band emission intensity peaks at 94 ± 2 km [e.g., *Witt et al.*, 1979; *Watanabe et al.*, 1981; *Murtagh et al.*, 1990]. This emission is the primary candidate of the space-based observation since the high population of O_2 in the lower atmosphere produces dark background conditions by absorbing the scattered emission from the Earth's surface or clouds. The previous nighttime limb scan space-based measurement carried out with the HRDI photometer on board UARS satellite reveals the typical intensity of the O_2 , globally, up to several kilo-Rayleighs [*Hays et al.*, 2003].

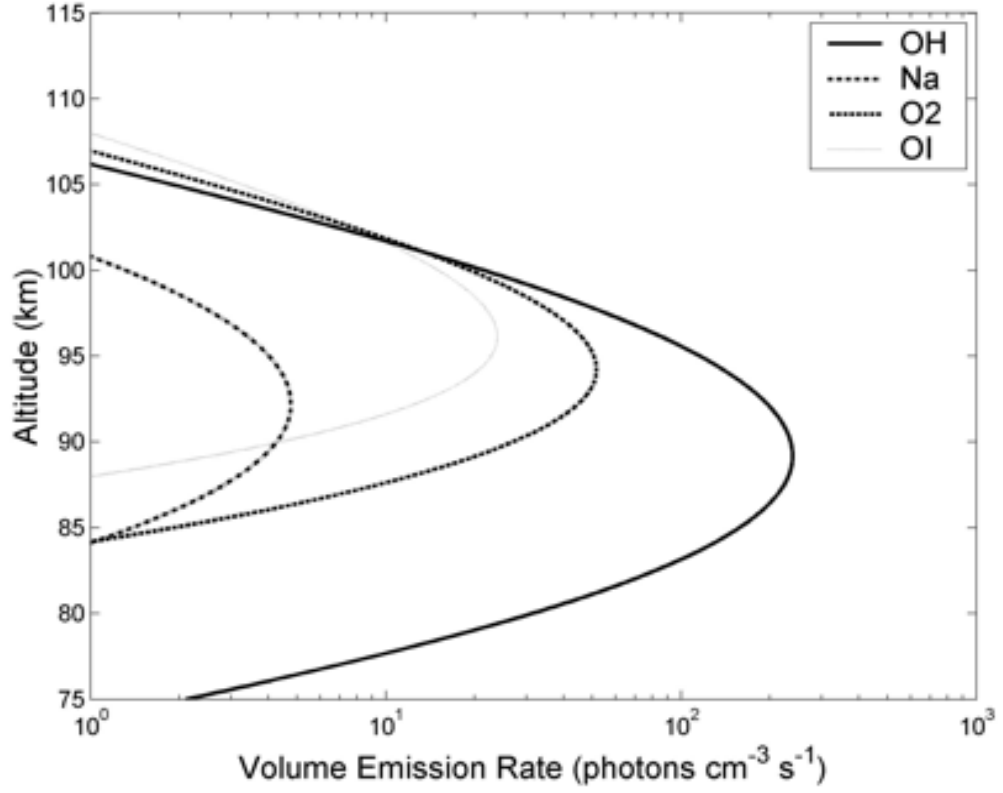
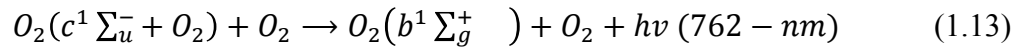
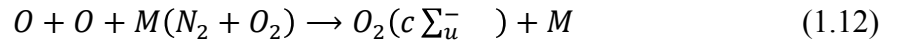


Figure 1.10. The volume emission rates of OH, sodium molecular and atomic oxygen [Swenson *et al.*, 2005; Vargas *et al.*, 2007].

The chemical processes of this emission is described as two-step mechanism (the Bath process) proposed by *Mc Dade et al.* [1986], given by:



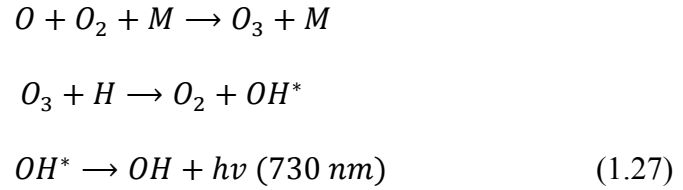
The volume emission rate (V_{O_2}) for this process can be expressed as:

$$V_{O_2} = \frac{c_1 A_1 [O]^2 ([O_2] + [N_2]) [O_2]}{(A_2 + c_2 [O_2] + c_3 [N_2]) (7.5 [O_2] + 33 [O])} \quad (1.14)$$

where c_1 , c_2 , and c_3 are the rate coefficient of the three-body recombination of O (the rate coefficients for quenching of O_2 by O_2 and N_2 , respectively). A_1 and A_2 express the molecular oxygen (0-0) A-band transition probability and the inverse radiative lifetime of O_2 . **Figure 1.11** shows the schematic transitions between various electronic states in the molecular oxygen emissions.

1.3.2. OH Meinel (8,3) Band around 730 nm

The study of the OH nightglow layer located at ~ 85 km, first reported by *Meinel* [1950]. The OH emission has a typical intensity of ~ 400 R/nm in the mid-latitude. The emission arises from the reaction (*McDade et al.*, 1986):



The volume emission rate of the OH Meinel (8,3) band (V) can be calculated using this expression:

$$V_{OH} = \frac{K_1 [O] [O_2]^2 (200/T)^{2.5}}{(1 + 7.7 \times 10^{-4} [O_2])} \tag{1.28}$$

where K_1 is the temperature-dependent rate coefficient [*Machlouf et al.*, 1995].

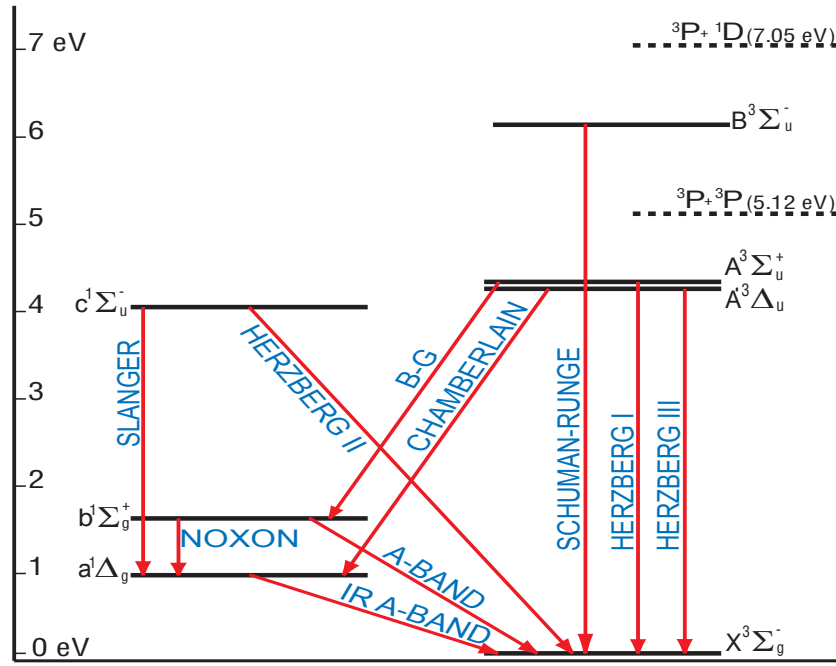
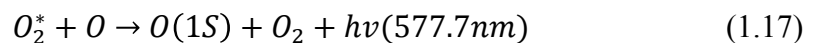
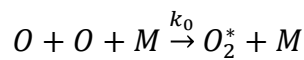


Figure 1.11. Schematic of transitions between various electronic states of molecular oxygen [Greer, *et al.*, 1987].

1.3.3. Atomic Oxygen Green Line at 577.7 nm

The Atomic oxygen (OI) emission at 577.7 nm was detected at mid-latitudes as the first discrete emission in the nightglow of the upper atmosphere. The energy level structure of the lower metastable states of the atomic oxygen is shown in **Figure 1.12**. The OI 577.7 nm emission peak generally appears centering at an altitude of 96 km. This emission arises from a two-step reaction given by [Mc. Dade *et al.* 1986]:



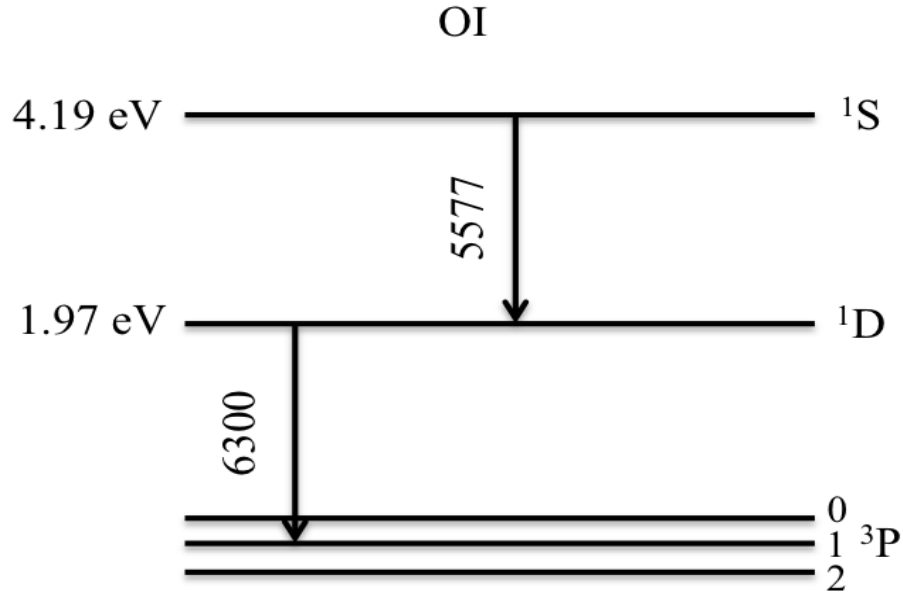


Figure 1.12. Structure of the metastable levels and the wavelengths of the transitions between these levels for a neutral oxygen atom.

The volume emission rate (V_{OI}) for the OI 577.7 nm emission is:

$$V_{OI} = \frac{A_5 k_0 [O]^3 \{[N_2] + [O_2]\}}{\{A_6 + k_5 [O_2]\} \{C'_{O_2} [O_2] + C'_O [O]\}} \quad (1.18)$$

where A_5 and A_6 are the Einstein coefficients, k_5 is the quenching rate of O(¹S) due to molecular oxygen. C'_{O_2} and C'_O determine the parameters describing the excitation process (Murtagh et al., 1990).

1.4. Concentric Gravity Wave Pattern

At the tropics and mid-latitudes, convection is considered to play a significant source for the generation of AGWs. If upward moving air in the unstable troposphere ‘overshoots’ the tropopause by 1 – 3 km into the stably stratified stratosphere and then collapses back down to the tropopause [*Pierce and Coroniti, 1966*]. These convectively generated AGWs reach to the upper atmosphere and produce the modulation of airglow emission in the mesopause region (80-100 km) as a group of expanding concentric rings on the horizontal plane with the center located near the convective source [*Dewan et al., 1998; Sentman et al., 2003; Suzuki et al., 2007, Yue et al., 2009; Vadas et al., 2009*]. Although AGWs are often observed by airglow imagers as quasi-linear and parallel-phase fronts, the concentric gravity waves (hereafter CGWs) are rarely observed [*Yue et al., 2009*]. **Figure 1.13** shows the sketch of convective plume model that generates the CGWs [*Vardas et al., 2009*].

The CGWs generated in the troposphere can penetrate into the mesosphere and lower-thermosphere (MLT) region under some specific conditions [*Horinouchi et al., 2002, Suzuki et al., 2007, Vadas et al., 2009, Yue et al., 2009*]. In order to avoid the critical level filtering from the background wind around the mesopause (80-100 km), the CGWs should have large phase speed (several ten m/s), large vertical and horizontal wavelength (several tens to hundreds km). The weak background wind (less than ~50 m/s) is also one of the important points in the observation of the CGWs.

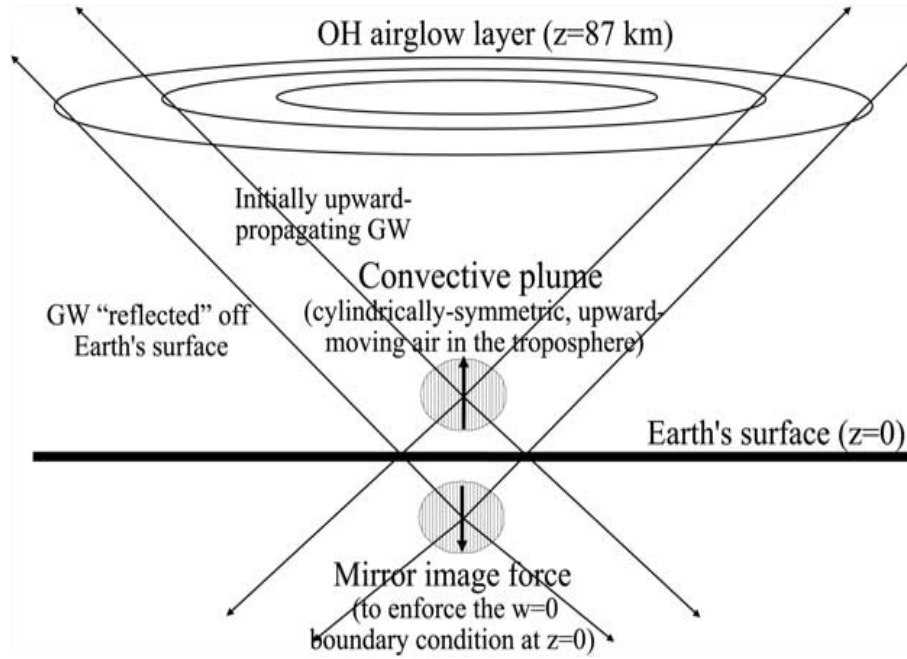


Figure 1.13. Schematic sketch showing the convective plume model that explains the concentric gravity waves [Vardas, *et al.*, 2009].

The ground-based observation of CGWs has a long story started with *Taylor and Hapgood* [1988] identified concentric rings in mesopause nightglow emissions by isolated thunderstorm in France. *Suzuki et al.* [2007] observed concentric wave patterns in both the OI (557.7 nm) and near-infrared OH Meinel band measured at Shigaraki, Japan with the source of the cumulonimbus cloud. *Yue et al.*, [2009] and *Vardas et al.* [2012] reported the observation of CGWs near the Great Plain region, USA. On the other hand, the space-based observations of these CGWs are limited. *Dewan et al.* [1998] using the data from the Midcourse Space eXperiment reported the first observation of CGWs from space. They reported radiation from CO₂ 4.3- μ m vibrational transitions (peak altitude at 40 km) showed circular or elliptical patterns above thunderstorms because the temperature and air density are perturbed

by GWs with the horizontal wavelength 25-50 km and radius of the ring is ~ 360 km.

Yue et al. [2013] reported the joint observations of CGWs using a ground-based airglow imager in Colorado and Atmospheric Infrared Sounder (AIRS) onboard the Aqua satellite on a single CGW event (3rd June 2008). The all-sky camera measured the CGW in OH band in the altitude of ~ 86 km while the AIRS measured the CGW in CO₂ 4.3-mm vibrational transitions radiation (~ 40 km).

Almost in all of the previous observations reported above they agree that the condition of background wind is very important in the upward propagation of the CGWs. *Suzuki et al.*, (2007) first speculated that the weak background wind could support the upward propagation of CGW and became evanescent because of the strong opposite wind, and were probably reflected downward. **Figure 1.14** shows the CGW observation from Shigaraki and the hodograph of background wind showing the changing wind direction (northeastward to southeastward) to the opposite of the CGW propagation (northeastward).

The model study by *Vardas et al.* [2009] supports this speculation of weak background wind conditions. The wind data (for 0-120 km) for the model study was obtained from the HAMMONIA-GCM model. **Figure 1.15** shows the effect of the wind on the CGW launched using the convective plume model. The result also shows that the background wind can shift the center of the CGW horizontally from its source ($x=0, y=0, t=0$), and “squashed” the concentric pattern into arc-like shape.

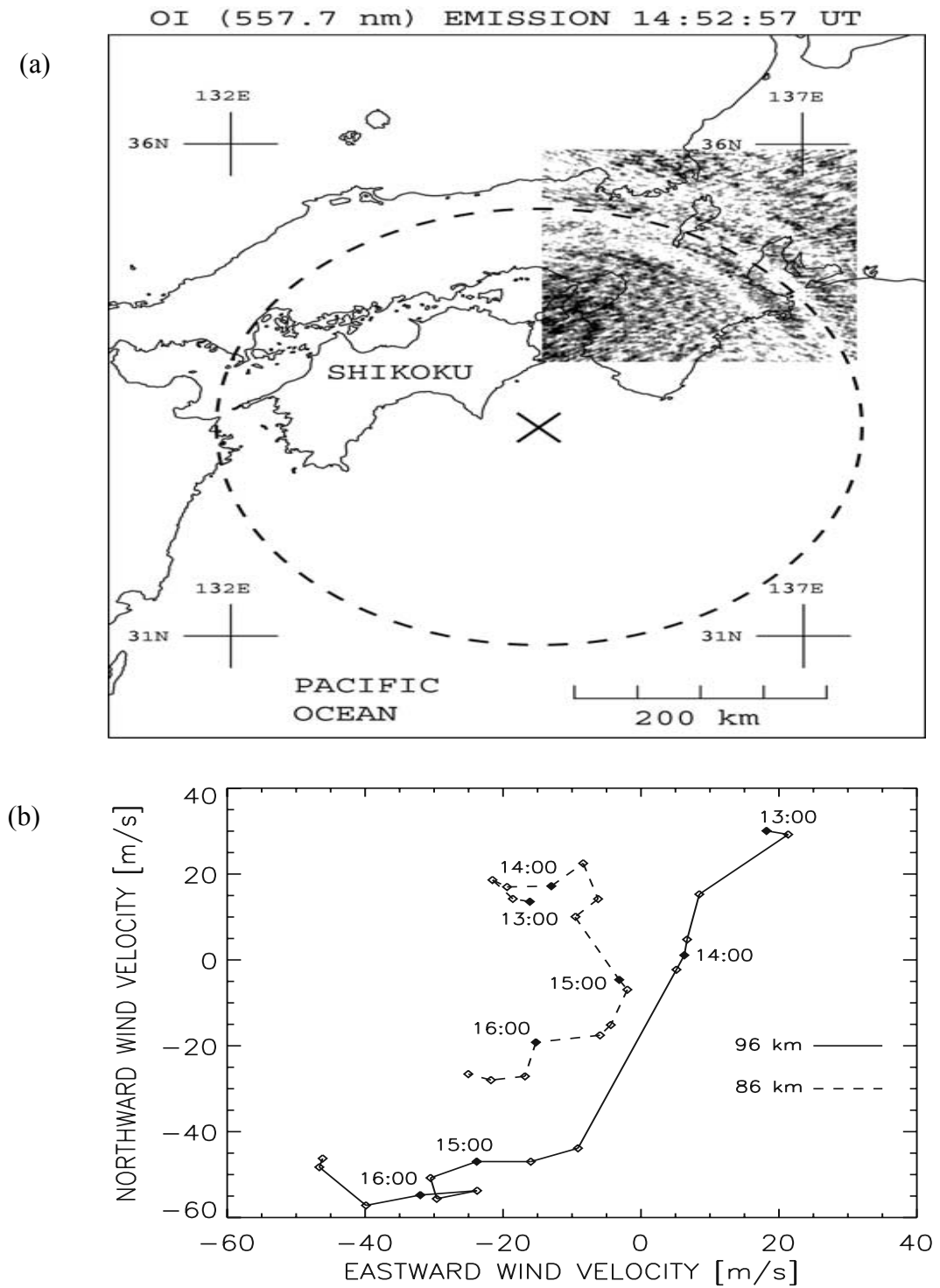


Figure 1.14. CGW moving northeastward observed on 3rd October 2002 from Shigaraki (a). The hodograph of background wind from 12:00-16:00 UT showing the direction of the wind in the 96 km changing from northeastward to southwestward [Suzuki *et al.*, 2007].

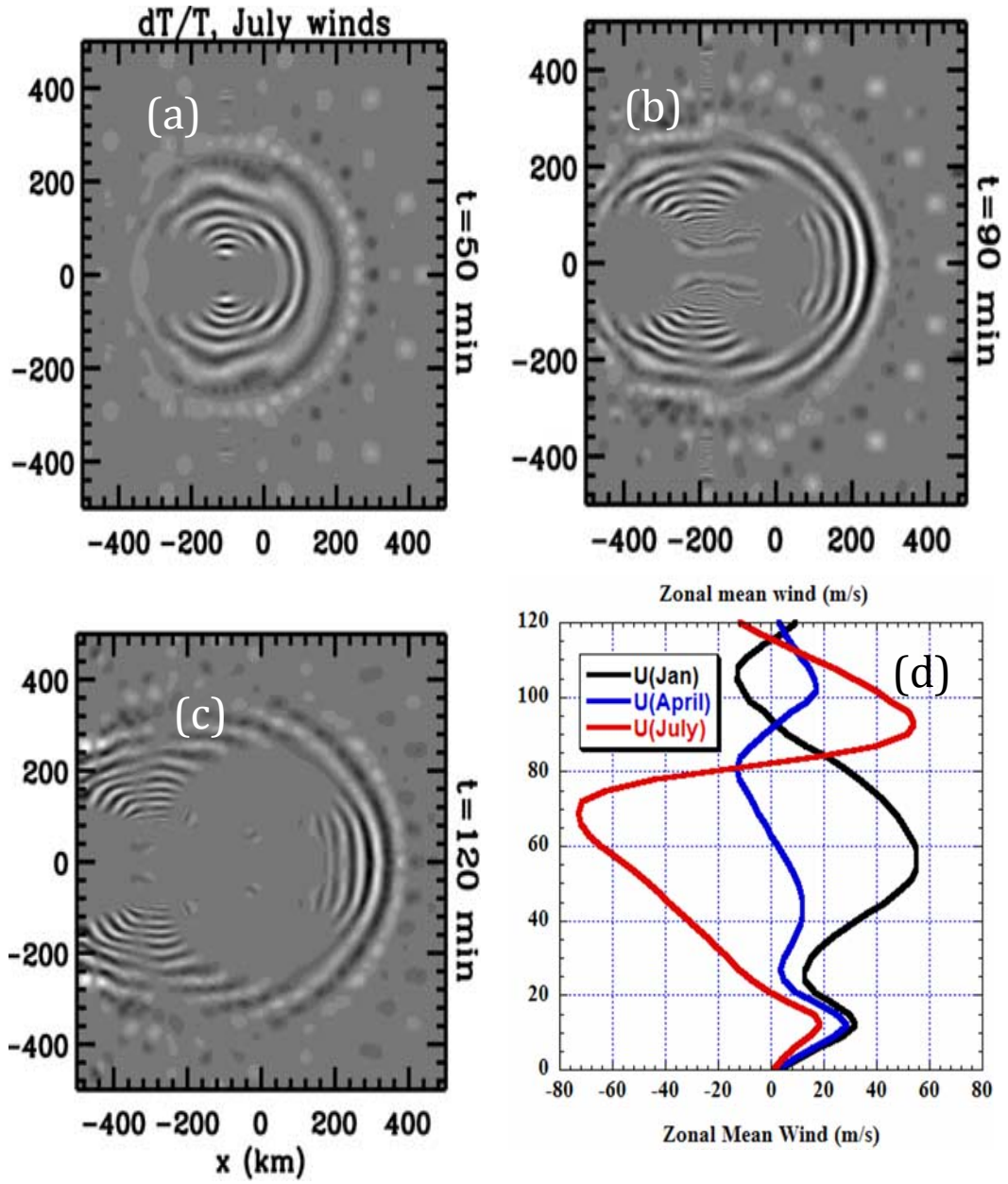


Figure 1.15. Computer simulation of CGW temperature perturbations at $z = 87$ km with the propagation time at $t = 50, 90$, and 120 min (a, b, and c, respectively) with the July zonal wind and (d) the zonal wind data obtained from HAMMONIA-GCM [Vadas *et al.*, 2009].

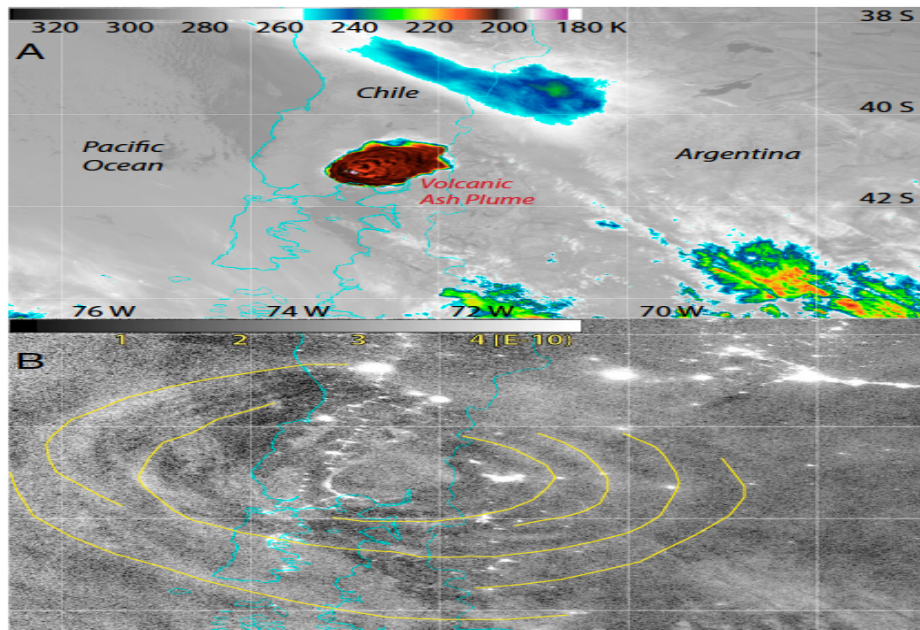


Figure 1.16. CGWs event generated by volcanic eruption observed by Suomi/DNB data reported by *Miller et al.* [2015].

Recently, *Azeem et al.* [2015] reported a multi instruments observation showing the CGWs propagate from troposphere up to the ionosphere. He used the data of AIRS in the stratosphere, DNB in the mesosphere and TEC data in the ionosphere. *Miller et al.* [2015] using the DNB data reported CGWs event generated by volcanic eruption along with various CGWs events generated by convective activities. Despite of the increasing study of CGWs, so far there is no global climatology of this GWs type due to the lack of observation data. The most recent and only statistical study of CGWs was reported by *Gong et al.* [2015] using the AIRS data to map the occurrence and wave parameters in the stratosphere (~ 40 km). As shown in **Figure 1.17**, they suggested that the occurrence of the CGWs is associated not only with tropical deep convections but also with summertime mid-latitude convection, wintertime extra-tropical jets, and topography such as islands.

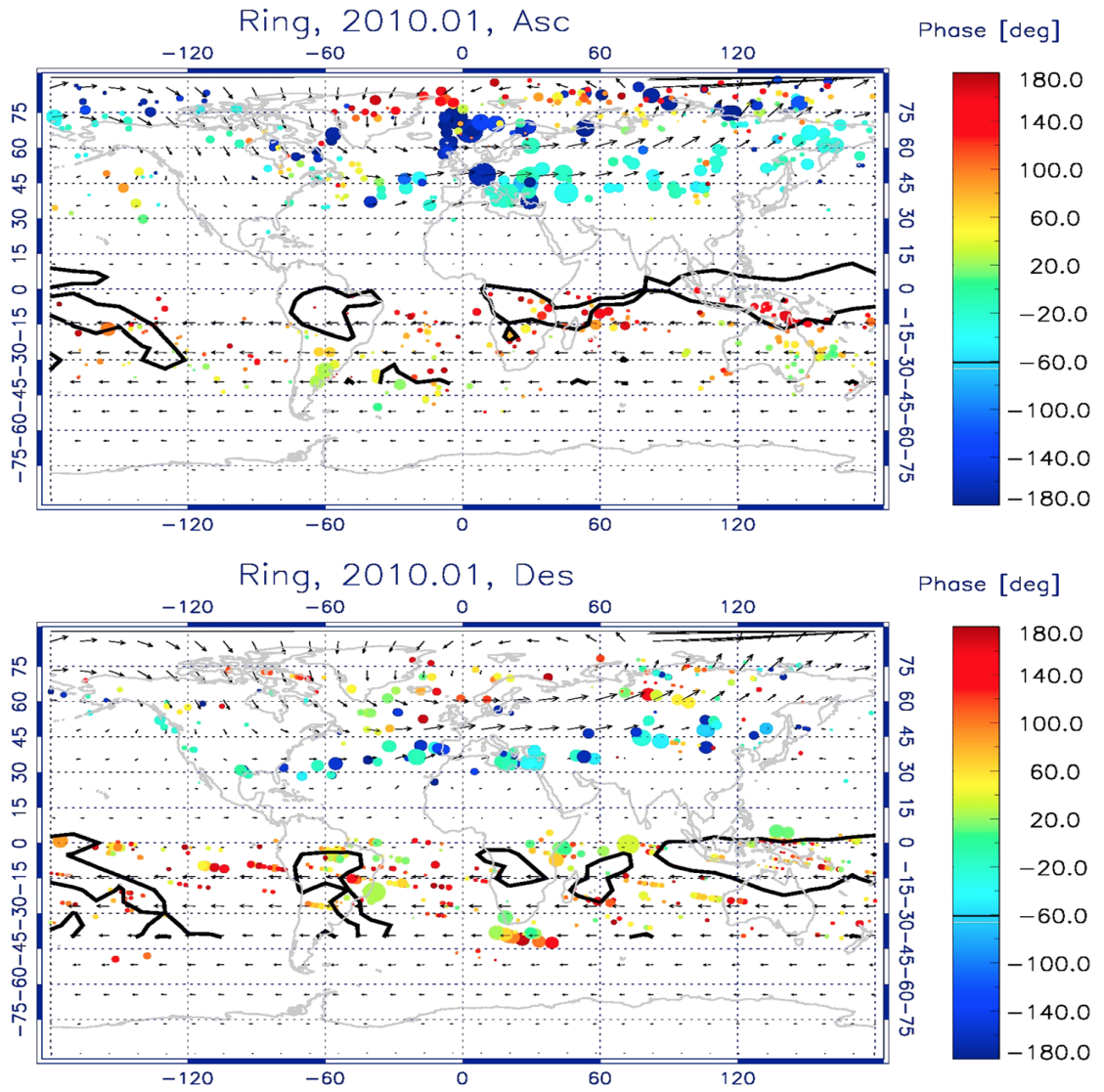


Figure 1.17. Geographic distribution of ring centers during January 2010 on (a) ascending and (b) descending orbits. The dot size is linearly proportional to wave amplitude, which varies from 1 to 5 K. Color corresponds to estimated phase propagation direction, with positive (negative) values meaning clockwise (counterclockwise) from the North. Arrows are MERRA monthly averaged wind vectors at 2.5 hPa. Thick black contours represent proxies of tropical deep convection. [Gong *et al.*, 2015].

2. Purpose of Thesis

CGWs are unique feature of AGWs seen in the upper atmosphere, which show an evidence for the direct coupling between the lower atmosphere and upper atmosphere. Past observations combined with model studies have revealed the generation of the CGWs and the mechanism of its upward propagation by identifying the relationship between the source region and the concentric pattern of airglow emission. However, all the past ground-based observations were limited by the typical coverage of all-sky imager (horizontal range of 20-500 km) and they have no data over the ocean in which the convective activities usually occur. In addition, the previous studies focused on the full ring pattern where the effects of the background profiles are minimal and direct upward propagation. More important, the past studies are mostly single event studies and give only local information. Therefore, a statistical study on global distribution of the CGWs is needed to gain a more comprehensive and quantitative understanding on the wave parameters, spatial and temporal variations regarding the energy transfer between lower and upper atmospheres.

The main objective of this thesis is to reveal the spatial and temporal variability of CGWs in the mesopause using the airglow data taken with a space-borne visible spectroscopic instrument. For the purpose, we analyzed the airglow data measured with the Visible and near-Infrared Spectral Imager (VISI) of the IMAP mission on the international space station (ISS). The IMAP/VISI was launched successfully on July 21st 2012 with H-IIB/HTV-3 and installed onto ISS. IMAP/VISI was continuously operated from October 2012 to August 2015 in the nightside hemisphere in the geographical latitude range of +/- 51 degrees.

IMAP/VISI measured three different airglow emissions of OI at 630 nm, the OH Meinel band at 730 nm and the O₂ (0-0) A-band at 762 nm with the typical spatial resolution of 16 – 50 km. The detail description of the instrumentation and supporting data used for the analysis is described in Chapter II.

The discussion of this thesis is divided into two parts. The first part of the discussion is a coordinated study between the IMAP/VISI and an airglow all-sky camera on a partial CGWs pattern in the mesopause described in Chapter III. The objective of this discussion is to examine the propagation of the CGWs through different airglow layers and analyze the background profile effects on the propagation mechanism. Since the start of the nominal observation of VISI, we found many interesting features on the airglow emissions showing meso-scale gravity waves structure in the MLT region. One of the rare events observed by IMAP/VISI is a partial concentric pattern of gravity wave in the O₂ (762 nm) airglow emission on October 18, 2012 over northeastern part of Japan around 1200 UT. The similar pattern was also observed by the all-sky camera at Rikubetsu (43.5N, 143.8E) in the OI 557.7 nm and OH airglow emissions. Beside the opportunity to study the effect of the background, this event also gave us a good opportunity to study possible ducted wave propagation.

The detailed analysis of the wave generation and propagation in the first part acts as a basis for the statistical study discussed in the second part of this thesis given in Chapter IV. IMAP/VISI observation provides us a unique opportunity to understand the statistical characteristics of coupling processes between lower and upper atmospheres with almost 3 years data of airglow emission in the mesopause region. 235 CGWs events were found from 3 years data of O₂ (762 nm) airglow emissions. The occurrence variability in seasonal, latitudinal, global distribution and

Chapter II

Instrumentation and Data Analysis

This chapter describes the instrumentation and data analysis used in this study. The main observational data used was the O₂ A-band (762 nm) nightglow emission taken with IMAP/VISI during the period from October 2012 to August 2015. An all sky camera data from Rikubetsu were also used in the first part of discussion in Chapter III to conduct a coordinated observation between space-based and ground-based observation in order to examine the waves motion between different airglow layers and effects of the background profiles to the wave propagation.

Since CGWs are tied principally to convection at lower-atmosphere, we used meteorological satellite data to locate the possible source of the waves. The convection index from MTSAT data, precipitation rate from TRMM and WWLLN lightning data were used to discuss the sources of the CGWs. Since there is no observational data of background winds above 60 km, we had to combine the observational and simulation data. MERRA was used to examine the background winds from 0-60 km and GAIA model was used to examine background winds from 60-100 km. Background wind data from Wakkani MF Radar was also used in the case study in Chapter III. SABER

instrument provides temperature profile from 0-180 km and it was used to discuss a possibility of thermal ducting in middle atmosphere.

2.1. Airglow Emissions data observed by IMAP/VISI and All Sky Camera

2.1.1. IMAP/VISI

IMAP/VISI is a visible and near-infrared spectral imager with a spectral resolution ($\lambda/\Delta\lambda$) of ~ 800 using a grism as a disperser [Sakanoi *et al.*, 2011, Akiya *et al.*, 2014]. Detail specification of IMAP/VISI is given in **Table 2.1**. By putting the two-line slit on the first focal plane combining a CCD imaging sensor, IMAP/VISI achieves the two field-of-views (FOVs) pointing 45° forward and 45° backward to nadir with mapping each of slit almost perpendicular to the orbital plane. The two-line scanning is useful to distinguish the airglow emission layer in the upper atmosphere (85-250 km) from the ground and clouds at the altitude of 0-10 km. With a wide viewing angle (90°) for each FOV, IMAP/VISI covers ~ 300 km width at the *F*-region altitude (~ 250 km) and ~ 600 km width at the *E*-region altitude (~ 95 km) perpendicular to an orbital plane as seen in **Figure 2.1**. IMAP/VISI measured three different nightglow emissions as shown in **Table 2.2**. Along with the type of airglow emissions, **Table 2.2** summarizes the scientific targets and the characteristic of the observed airglow emissions such as intensity, emission height and spatial resolution.

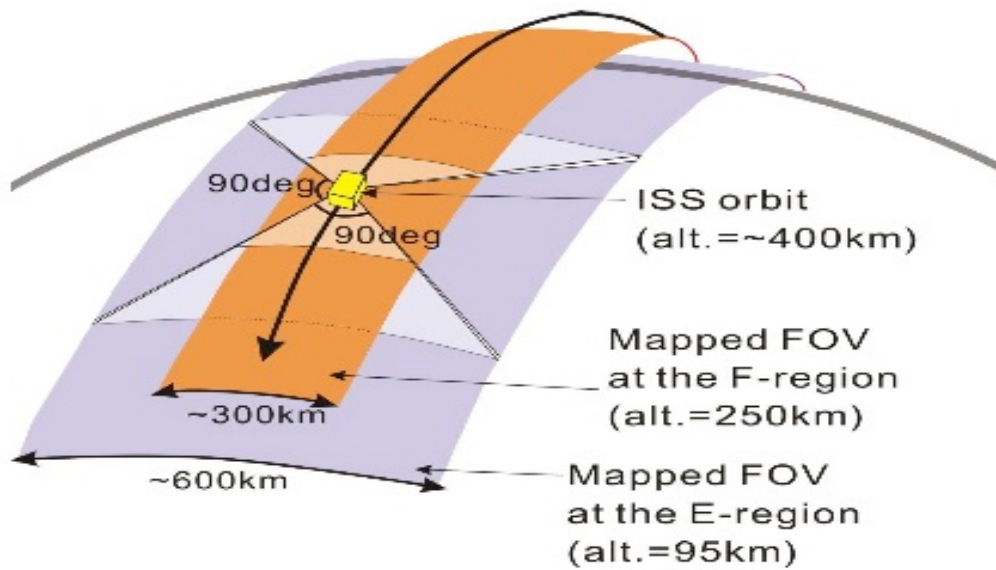


Figure 2.1. Schematic drawing of the FOVs of IMAP/VISI mapped on the emission layers [Sakanoi *et al.*, 2011].

Table 2.1. Detail specifications of IMAP/VISI

Field-of-views	Rectangular-shaped (90x0.09 deg.) FOVs pointing 45 deg. Forward and backward to nadir
Objective lens	F/0.96 and f=5.5 mm
Spectroscopic properties	Wavelength coverage 630-762 nm with resolution of ~1.0 nm/pixel (R~800)
CCD sensor	E2V 47-20 back-illuminated AIMO, 1024x1024 pixels, 1 pixel size=13.3 x13.3 μ m
CCD cooling	Below -25 deg. C with a Peltier electrical cooling connected to a radiator toward the earth
Size	450 (X) x 240 (Y) x 210 (Z)
Weight and power	14.5 kg, 7.9 W

Table 2.2. Summary of scientific targets of IMAP/VISI

Airglow (Wavelength)	Region (Altitude)	Scientific target	Typical spatial resolution	Typical intensity
OH Meinel (730 nm or 850 nm)	Mesosphere (85 km)	Gravity wave, temperature	14 km	400 R/nm
O ₂ (0-0) (762 nm)	Mesopause (95 km)	Gravity wave	14 km	1000 R
OI (630 nm)	Thermosphere (250 km)	Gravity wave, plasma bubble, traveling ionospheric disturbance	14-35 km	100 R

IMAP/VISI was operated only in nighttime to avoid the sunlit contamination. During the observation, IMAP/VISI uses three different observation modes, i.e. calibration mode, spectral mode and peak mode. In the calibration mode, the whole CCD frame data (1024 x 1024 pixels) were recorded without binning. In the spectral mode, the pixel position was determined on each row in a region-of-interest (ROI) area and then the spectral profiles, in which each ROI area had 12 pixels along a row around maximum, were recorded. In the peak mode, the ROI areas were the same as those in the spectral mode, but only the maximum and minimum values on each row in a ROI were recorded. **Figure 2.2** shows the first light image of IMAP/VISI taken on August 13, 2012 and the position of each ROI. The ROI is determined for each airglow emission (OH, O₂ and O) and each FOV (back and forward); resulted in 6 total of ROIs areas. For the pixel binning, the asymmetrical on-chip binning is applied for the each ROI. The size of row x column binning is selectable from 1x8, 1x16, and 1x32 pixels.

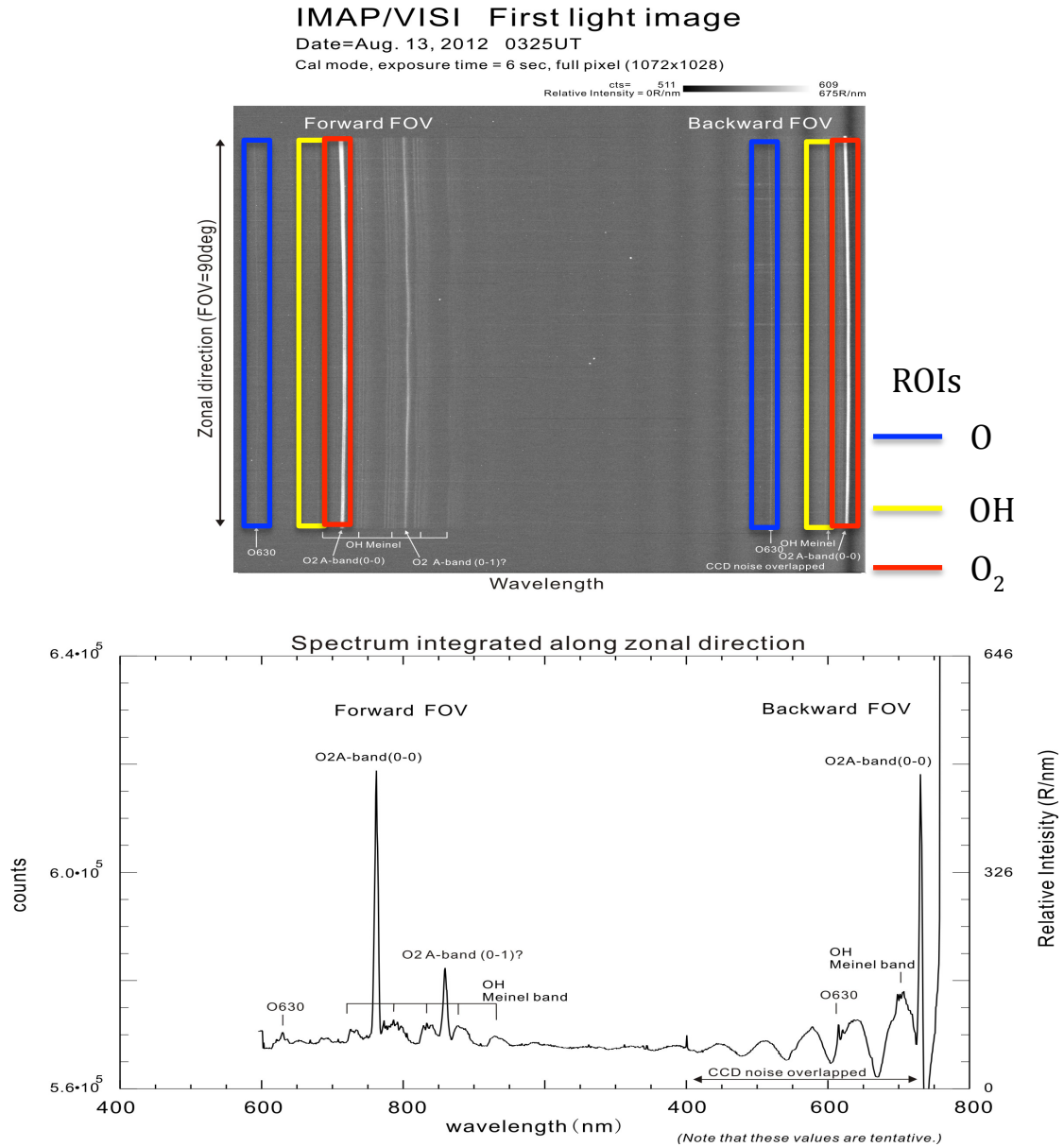


Figure 2.2. Top: First light (a CCD full-frame image) of IMAP/VISI obtained with the calibration mode on August 13th, 2012. The horizontal axis is the wavelength and the vertical axis is the zonal direction. Each ROIs are shown in forward and backward FOVs. Bottom: the spectral profile estimated by integrating counts along a column of the CCD frame. The horizontal axis is the wavelength in nm and the vertical axis shows the count [courtesy of T. Sakanoi].

Due to the limitation of data transfer rate from the international space station, the peak mode was used during the nominal observation. Successive exposures of

IMAP/VISI in peak mode provided two scanning images, i.e., background and intensity peak images, for forward and backward FOVs. Typical exposure time is 1 sec and exposure cycle is 1.86 sec, which corresponds to 14 km resolution along an orbital track. Spatial resolution along a slit is approximately 10 km at the *E*-region altitude determined by a pixel binning. Relative airglow intensity is obtained by subtracting the background data from the intensity peak data while the absolute intensity of each airglow emission is calculated by applying the calibration factors obtained by the spectral mode. An example of O₂ (762 nm) airglow emission data from IMAP/VISI observation is shown in **Figure 2.3**.

The data from both FOVs then could be projected onto a geographical coordinate system by assuming the altitude layer of the airglow emission was 95 km for O₂ (762 nm). **Figure 2.4** shows the forward FOV data from the 16 April 2013 event mapped onto the geographical coordinate. IMAP/VISI observation covered the equatorial and mid-latitudes between 51.6° N to 51.6° S in geographical latitude (GLAT). **Figure 2.5** shows an example of 4-days plot of IMAP/VISI data showing the latitudinal coverage of IMAP/VISI observation on global map.

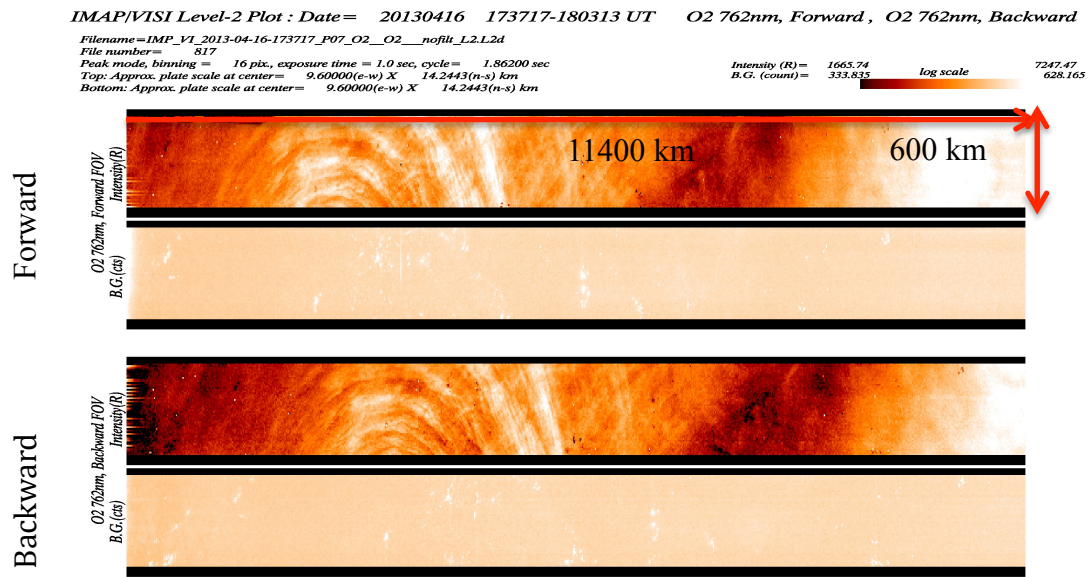


Figure 2.3. An example of O2 (762 nm) data on April 16, 2014 around 17 UT. Concentric gravity waves can be seen in both FOVs. Red arrow shows the direction of the ISS movement.

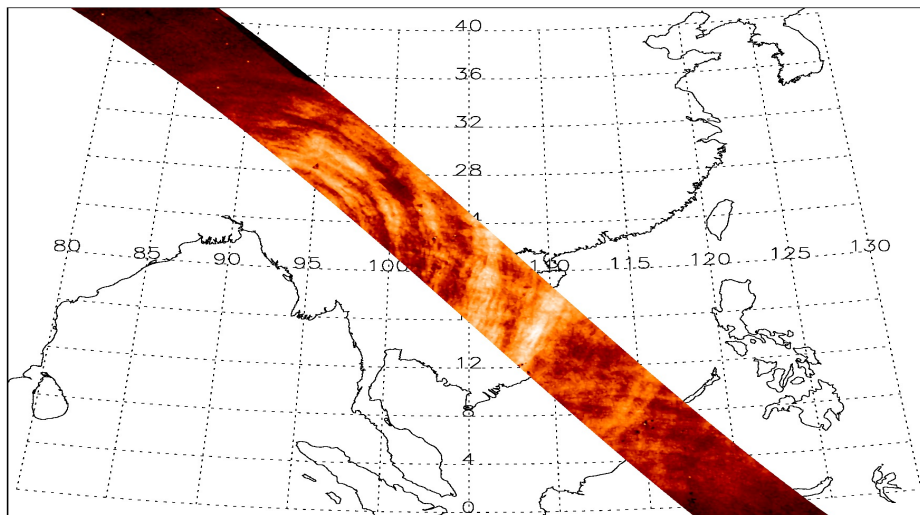


Figure 2.4. Forward FOV O2 (762 nm) airglow emission on April 16, 2013 projected onto geographical coordinate by assuming the altitude of the airglow layer was ~95 km.

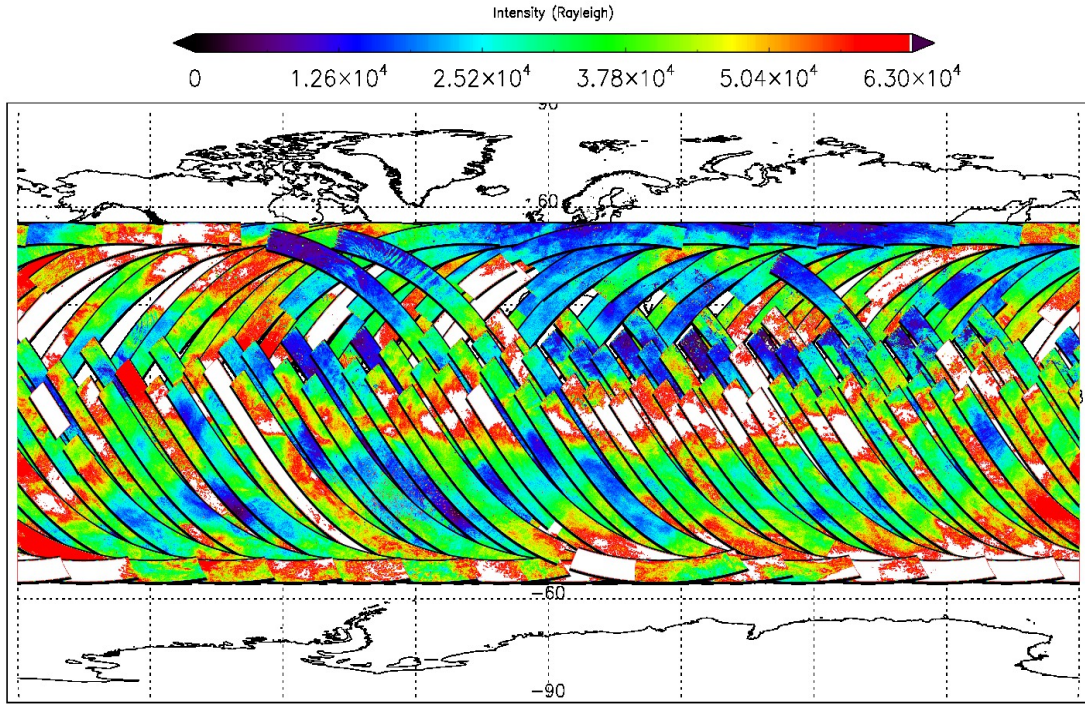


Figure 2.5. 4-days plot of IMAV/VISI data on April 1-4, 2013. The plot showing the latitudinal coverage of the IMAV/VISI data. The color bar shows the intensity of the data in Rayleigh [R].

2.1.2. Rikubetsu All Sky Camera

The all-sky imager at Rikubetsu, Japan (43.5°N , 143.8°E in GLAT) is part of the Optical Mesosphere Thermosphere Imagers (OMTIs) network [Shiokawa *et al.*, 2009]. The imager uses a cooled-CCD camera with 512×512 pixels and has five filters to measure OI 557.7 nm, OI 630 nm, OH near-infrared band, hydrogen-beta 486.1 nm and sky background emissions. The OH and OI 557.7 nm images on October 18, 2012 used in this discussion in Chapter III were obtained with a time resolution of 1.5 min. The exposure times of OH and OI 557.7 nm were 2 s and 30 s, respectively.

Table 2.3. Filters, typical exposure time and sensitivity for the Rikubetsu all-sky camera [Shiokawa *et al*, 2000].

Channel	Emissions	Wavelength (nm)	Bandwidth (nm)	Exposure (sec)	Sensitivity (count/R/s)
1	OI	557.7	1.78	105	0.049
2	OI	630	1.82	165	0.053
3	OH	720-910	190	15	-
4	H β	486.1	1.92	-	0.005
5	Background	572.5	1.77	105	0.050

2.2. Convective Activity Data from MTSAT and TRMM and WLLN

2.2.1. MTSAT

MTSAT (Multi-function Transport Satellites) is a series of weather and aviation geostationary satellites, which is located in the geostational orbit at the altitude of 35,800 km above the equator and at 140 degrees east longitude or 145 degrees east longitude. They provide information for monitoring the distribution/motion of clouds, sea surface temperatures and distribution of water vapor with spatial and time resolution of 4 km and 30 min, respectively [Takeuchi *et al.*, 2007].

MTSAT has five channels, four infrared (IR1 at 10.3-11.30 μm , IRI2 at 11.5-12.50 μm , IRI3 at 6.5-7.0 μm , IR4 at 3.5-4.0 μm) and one visible channel (VIS at 0.55-0.80 μm). The data are provided by Weather Home, Kochi University and can be freely used for research and education purposes [<http://weather.is.kochi-u.ac.jp/archive-e.html>]. To investigate the convection activity in the troposphere, the convective index

was derived from the MTSAT-IR1 data then the one-hourly convective index (I_c) was defined by [Ohsawa *et al.*, 2001]

$$I_c = T_{850mb} - TBB \quad (2.1)$$

where the T_{850mb} is the temperature at the altitude of 850 mb in pressure level and TBB is the top-cloud temperature observed by MTSAT-IR1. **Figure 2.6** shows an example of convective index derived from MTSAT-R1 data over Japan area (20° N-50° N and 120° E-150° E) on October 18, 2012 at 1100 UT.

2.2.2. TRMM

In addition to the convective index data, precipitation data from the TRMM (Tropical Rainfall Measuring Mission) satellite were used to locate the wave source. The NASA Tropical Rainfall Measuring Mission (TRMM) is a joint U.S.–Japan satellite mission to provide the first detailed and comprehensive dataset of the four dimensional distribution of rainfall and latent heating over vastly under sampled tropical and subtropical oceans and continents (40°S–40°N) [Liu, Z., *et al.*, 2012]. There are five instruments onboard the TRMM satellite, and four of them are used for precipitation, as shown in **Table 2.4**. Standard TRMM products from the Visible and Infrared Scanner (VIRS), the TRMM Microwave Imager (TMI), and Precipitation Radar (PR) are archived at and distributed from the NASA Goddard Space Flight Center (GSFC) Earth Sciences Data and Information Services Center (GES DISC).

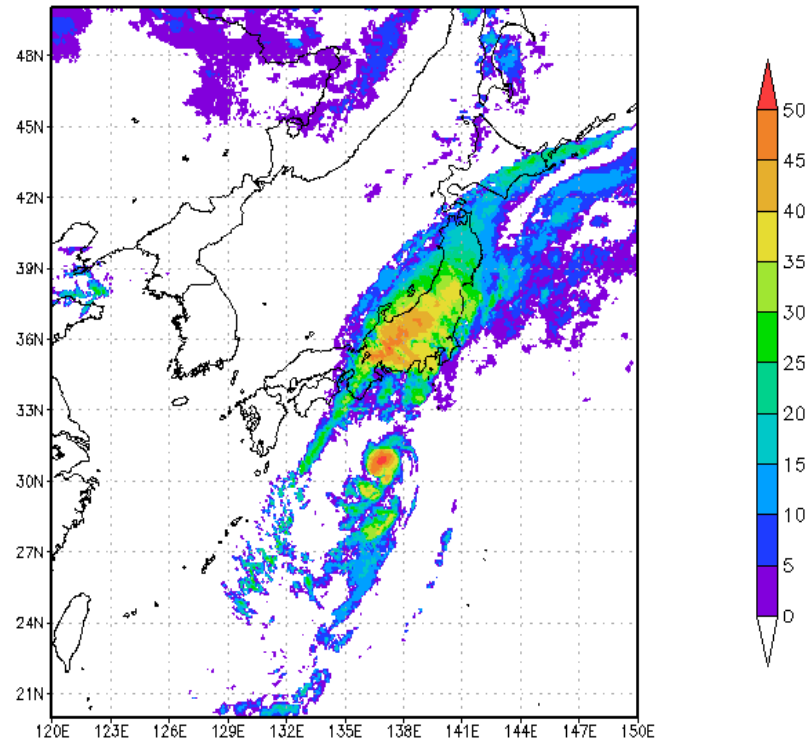


Figure 2.6. The convective index derived from the TBB data of MTSAT satellite at 1100 UT on 18 October 2012. The color bar shows the hourly convective index derived from the top-cloud temperature of MTSAT-R1 data.

Data set used in this study was obtained from the Precipitation Radar by using an online user-friendly analyzing tool called Giovanni (GES-DISC Interactive Online Visualization and Analysis Infrastructure) TOVAS (The TRMM Online Visualization and Analysis System). **Figure 2.7** shows an example of global precipitation data obtained from Giovanni TOVAS homepage at <http://gdata1.sci.gsfc.nasa.gov>.

Table 2.4 TRMM-precipitation related instruments

Instrument name	Band frequencies/ wavelength	Spatial resolution (km)	Swath resolution (km)
Visible and Infrared Scanner (VIRS)	5 channels (0.63, 1.6, 3.75, 10.8, and 12 μm)	2.4	833
TRMM Microwave Imager (TMI)	5 frequencies (10.7, 19.4, 21.3, 37, 85.5 GHz)	5.1 at 85.8 GHz	878
Precipitation Radar (PR)	13.8 GHz	5 (vertical: 250 m)	247
Lightning Imaging Sensor (LIS)	0.7774 μm	4.3	668

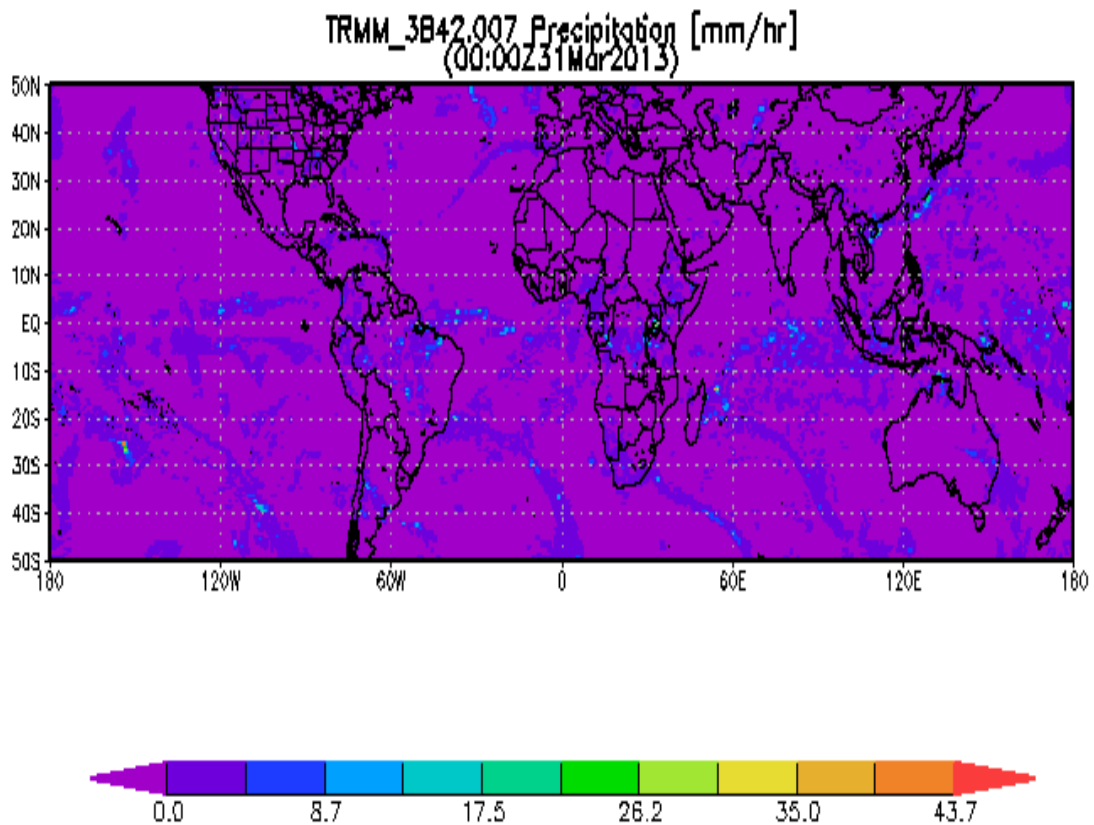


Figure 2.7. An example of global precipitation data obtained from Giovanni TOVAS on March 31, 2013 at 0000 UT.

2.2.3. WWLLN

The World Wide Lightning Location Network provides global lightning location using sparsely distributed very low frequency (VLF) detections stations [Jacobson *et al.*, 2006]. The spatial accuracy of the data is around 15 km, which is good enough to resolve convective-storm cells within a larger storm complex. Thus WWLLN can be useful for locating thunderstorms for possible source of CGWs.

WWLLN real time data are available for research purposes from the University of Washington [<http://wwlln.net>]. **Figure 2.8** shows an example of one-day lightning location globally from WWLLN data.

2.3. Background Wind data from GAIA, MERRA and Wakkanai MF Radar

2.3.1. GAIA

Background wind plays important role in upward propagation of CGWs as they act as filtering system [Suzuki *et al.*, 2007; Vadas *et al.*, 2009]. However, the observational data for background winds are limited, especially in the middle and upper atmosphere. Therefore, data from model are generally used to provide the global wind data. Ground-to-Topside Model of Atmosphere and Ionosphere for Aeronomy (GAIA) is a coupled model of atmosphere and ionosphere that covers the altitude from troposphere to exosphere [Jin *et al.*, 2011]. The data from GAIA is a result from realistic simulation by implementing Japanese 25-years reanalysis (JRA-25) incorporating with F10.7 solar radiation value as the external source. Global distribution of neutral and electron

temperatures, wind velocities (zonal, meridional and vertical) and neutral and ion density of nitrogen and oxygen are estimated with the GAIA model with a horizontal resolution of 2.8° and 0.2 scale height in vertical direction. **Figure 2.9** shows an example of global map of zonal wind data at an altitude of 95 km of GAIA model.

2.3.2. MERRA

MERRA (Modern-Era Retrospective Analysis for Research and Application) is NASA reanalysis using a major new version of the Goddard Earth Observing System Data Assimilation System Version 5 (GEOS-5). Its product is 3-hourly background wind on 42 pressure levels up to 0.01 hPa (~ 60 km). The grid used for MERRA is $1/2$ degrees latitude and $2/3$ degrees longitude [Rienecker *et al.*, 2011]. The data are available at the Modeling and Assimilation Data and Information Services Center (MDISC), managed by the NASA Goddard Earth Sciences (GES) Data and Information Services Center (DISC). **Figure 2.10** shows an example of zonal-mean zonal wind from MERRA data on March 1 2013. This plot was obtained from NIPR Trajectory Meteorological Display website (<http://www.firp-nitram.nipr.ac.jp/en/>).

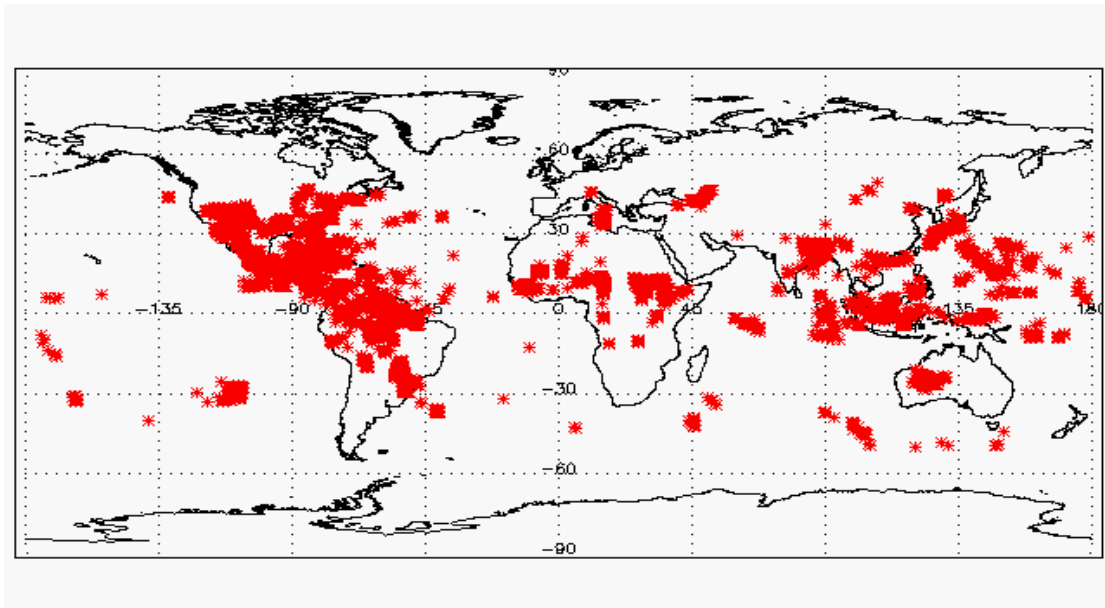


Figure 2.8. One-day global lightning occurrences from WLLN data. The map shows data on September 1, 2013.

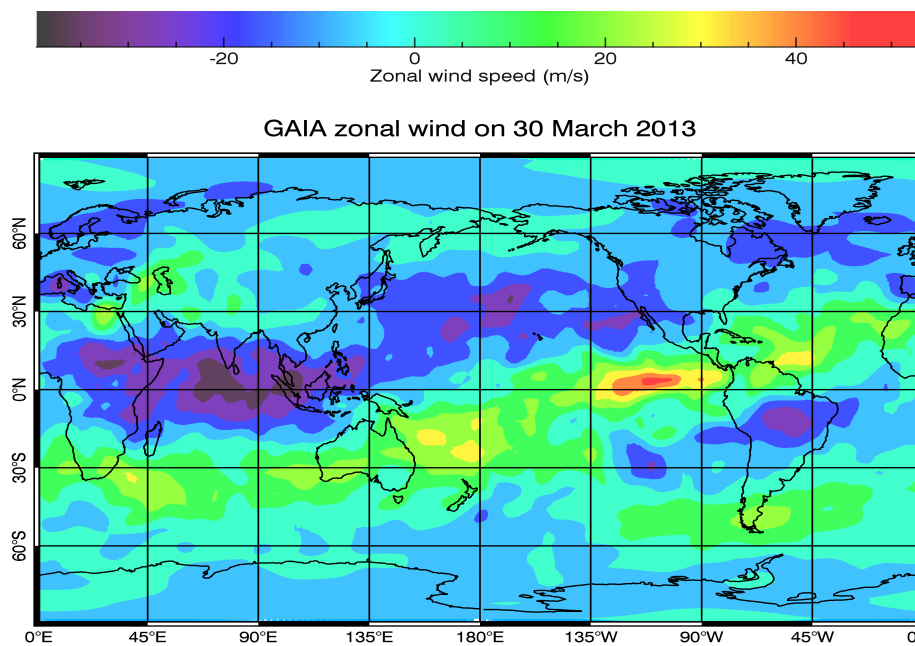


Figure 2.9. Global map of zonal wind data at an altitude of 95 km of GAIA model on March 30, 2013. The color bar indicates the zonal wind speed in m/s.

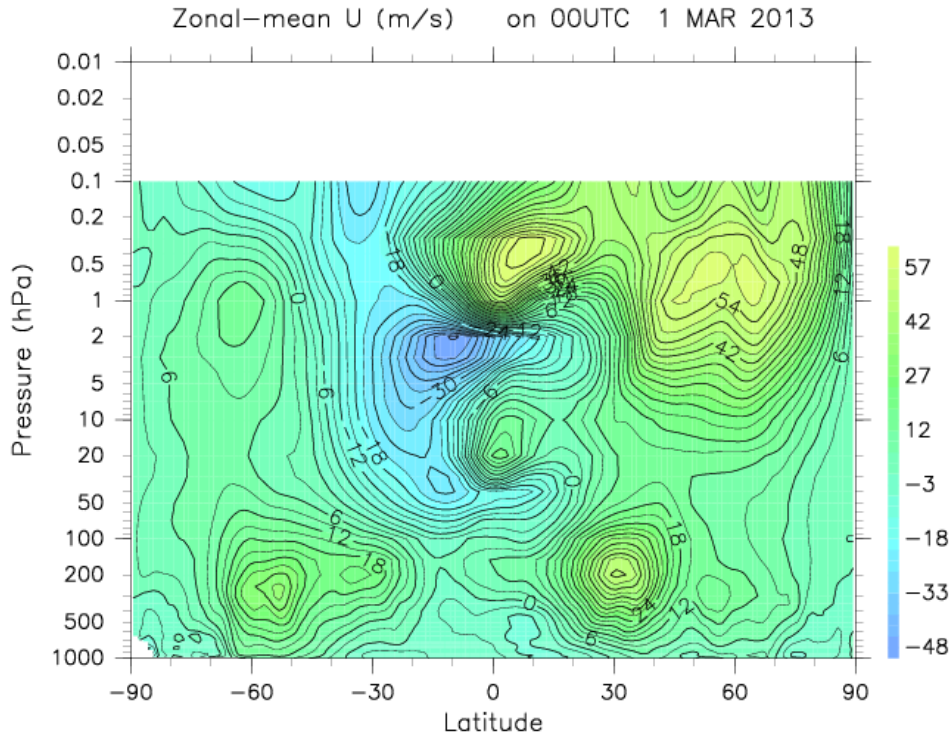


Figure 2.10. Zonal-mean zonal wind data from MERRA on March 1, 2013. The plot shows the latitudinal distribution as a function of pressure level. The color bar indicates the wind speed in m/s where positive values show the eastward wind.

2.3.3. Wakkani MF Radar

The MF radar has been operated at Wakkanai, Japan (45.36°N , 141.81°E in GLAT) since 1996 [Igarashi *et al.*, 1999]. The MF operating frequency is 1.9585 MHz with a peak transmitter power of 50 kW. The Wakkanai MF radar observes the wind in the mesosphere and lower-thermosphere (MLT) region (84-108 km) with an altitude resolution of 2 km. The specification of this radar is summarized in Table 2.6.

Table 2.6. Specification of Wakkanai MR radar [*Igarashi et al.*, 1999]

Parameters	
Location	45.36° N, 141.81° E
Peak envelope power	50 kW
Operating frequency	1.9585 MHz
Half power pulse width	48 micro second
Sampling interval	2 km
Operated period	Since 19 th September 1996

In this thesis, one-hour average of zonal and meridional wind data for an altitude range of 84-102 km were used to discuss the background wind condition in the MLT region in conjunction with IMAP/VISI data and Rikubetsu all-sky image data.

2.4. Temperature Profile from SABER data

The Sounding of the Atmosphere using Broadband Emission Radiometry (SABER) is one of four instruments on the NASA Thermospheric Ionosphere Mesosphere Energetics Dynamics (TIMED) satellite [*Russel et al.*, 1999]. Using a 10-channels broadband infrared radiometer, which covers the spectral range from 1.27 to 17 μm , SABER scans the atmospheric limb vertically and provides vertical profiles of kinetic temperature, geopotential height, pressure, ozone, carbon dioxide, water vapor, atomic oxygen and atomic hydrogen as well as volume emission rate for 5.2 μm NO, 2.1 μm OH, and 1.27 μm O₂ (¹ Δ) with an altitude of 80-100 km [e.g. *Mertens et al.*, 2001, *Feofilov et al.*, 2009]. **Figure 2.11** shows latitudinal distribution of kinetic temperature on February 9, 2013.

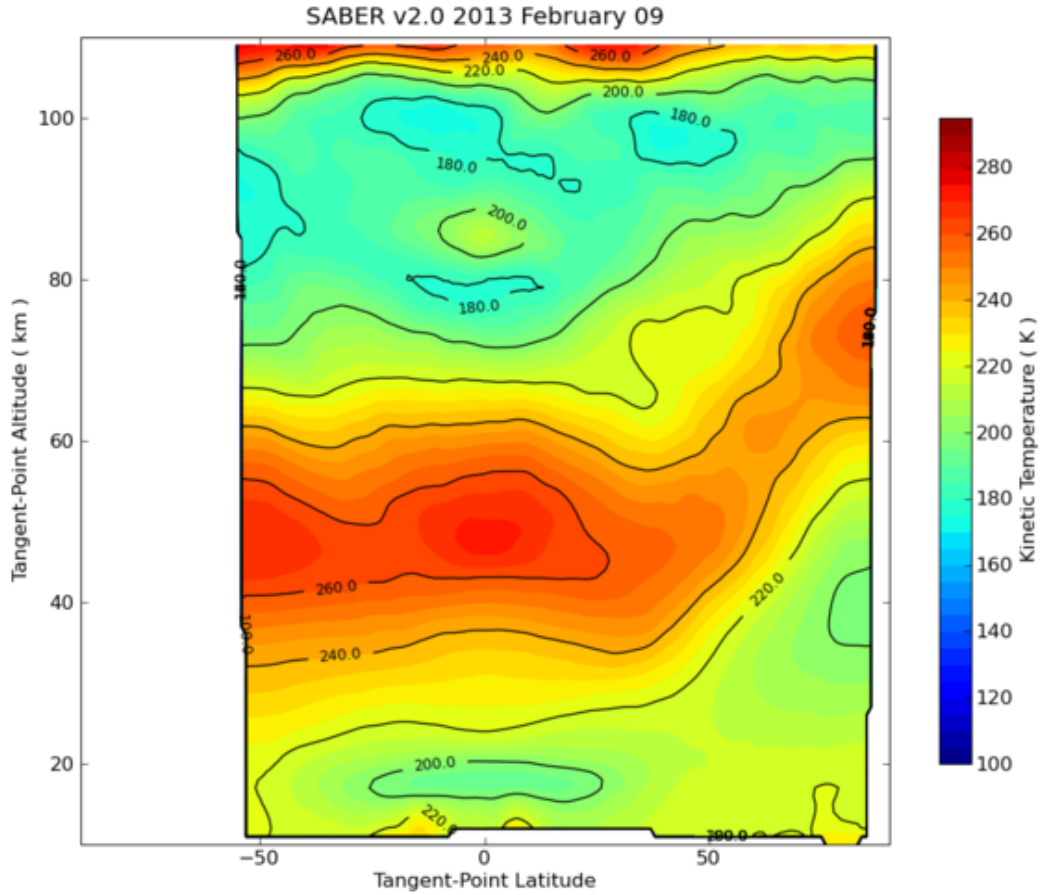


Figure 2.11. Latitudinal distribution of kinetic temperature of SABER data on February 09, 2013 as a function of altitude. The color bar shows the kinetic temperature in K.

2.5. Analysis Method

2.5.1. Data Analysis of IMAF/VISI

In order to discuss the source of the CGWs and the wave parameters, it is necessary to calculate the center of the circular wave fronts since the CGWs are usually generated by a point source, which should be located close to the center. Owing to the unique circular pattern of CGWs, the center and the horizontal wavelength can be estimated by fitting a

circle to the wave fronts. To do the fitting, at first we picked several points from each curvature wave front of the airglow data in geographical latitude and longitude $[(\lambda_{1k}, \varphi_{1k}), (\lambda_{2k}, \varphi_{2k}), \dots, (\lambda_{ik}, \varphi_{ik})]$, assuming the airglow emission was mapped onto the geographical coordinate with altitude of ~ 95 km, and then applied the least squares method. This method has been established in the previous studies of CGWs [Hapgood and Taylor, 1982; Suzuki *et.al.*, 2013 and Yue *et.al.*, 2013]. A reasonable measure to fit a circle to the points on the wave front is given by minimizing the residual of the sum of the squares of the distances (SS) from the points to the assumed circle. The minimization can be obtained by choosing the center of the assumed circle at geographical latitude λ_c and longitude φ_c then calculated the distances from the chosen center given in Equation (2.3), finally the SS was calculated using the Equation (2.2). The pair of longitude and latitude (λ_c, φ_c) that gives the minimum SS is the center for the best fitted circle. For example, for CGWs event on April 16, 2013 shown in **Figure 2.4**, we calculated the SS for the area that covers the latitude range from 20° to 30° N and longitude from 80° to 120° E. This measure is given by

$$SS = \sum_{i=1}^n (r_{ik} - r_k)^2 \quad (2.2)$$

and r_{ik} can be written as

$$r_{ik} = R_e \cos^{-1}[\sin\varphi_c \sin\varphi_{ik} + \cos\varphi_c \cos\varphi_{ik} \cos(\lambda_{ik} - \lambda_c)] \quad (2.3)$$

where r_{ik} is the distance from the chosen center to the i -th point on the k -th wave front and $r_k = \sum_i r_{ik} / n_k$ is the mean radius, n_k is the number of points and R_e the Earth radius (6378 km).

In the case on 16 April 2013 at 1700 UT, the SS was minimized at 20° - 24° N with in geographical latitude, and 89 - 91° E in longitude with value of 0.03 - 0.15 . The lowest value was found at $[21.2^\circ$ N, 90.5° E] with outermost radius of the ring is ~ 2000 km. Since the CGWs are assumed to be generated by a point source located near the center of the waves, the estimated center can be used to determine the source. **Figure 2.11** shows the result of the fitting over plotted with the emission and TRMM data. The precipitation rate shows a highly convective activity around the estimated center, which was likely the source of the CGWs.

The horizontal wavelength was calculated by averaging the radius of each wave front from the center [*Suzuki et al.*, 2013]. **Figure 2.13** shows estimation of horizontal wavelength from the calculated rings for the case on 16 April 2013 at 1700 UT shown in **Figure 2.12**. The crosses indicate the radii of the best fitting set of wavefronts. Number of wavefronts is determined at the peak of concentric airglow intensity pattern from the center. The horizontal wavelength was found to be 303.2 ± 64.7 km. Maximum radius was used to examine how far the CGWs can propagate in the horizontal direction from its source.

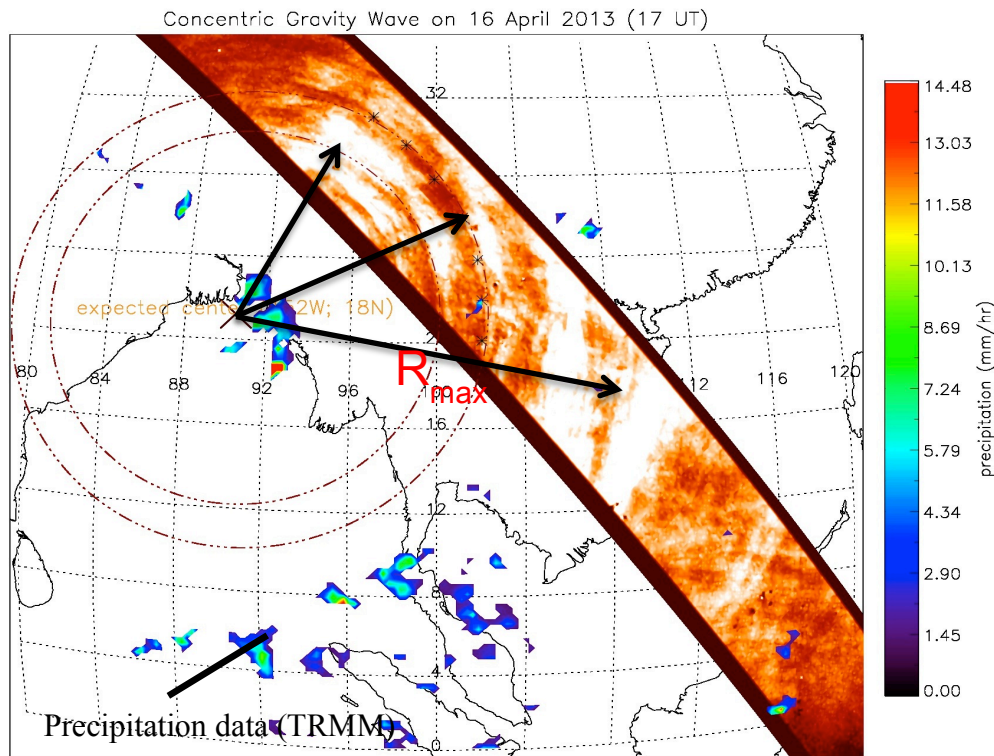


Figure 2.12. Circle fitting applied to the CGWs event on 16 April 2013 at 1700 UT. The X mark shows the center of the wave as a result of circle fitting. The black arrows represent the radius from the estimated center to each wave front. The maximum radius (R_{max}) shows the distance from the estimated center to the outermost ring. The color bar shows the 3-hourly precipitation rate from TRMM data (1330-1630 UT).

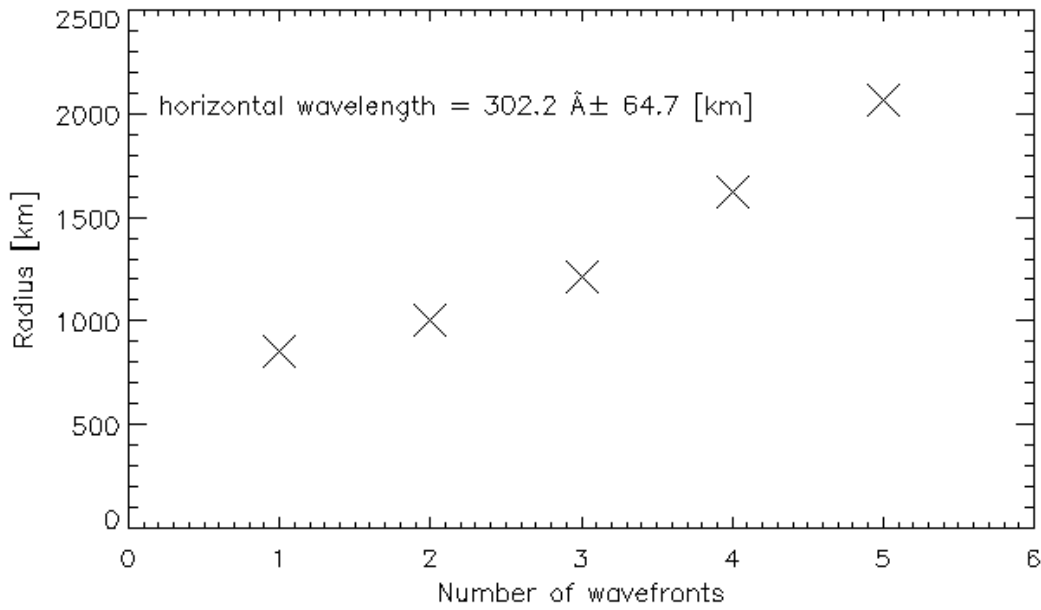


Figure 2.13. Estimation of horizontal wavelength from the calculated rings for the case on 16 April 2013 at 1700 UT. The crosses indicate the radii of the best fitting set of wavefronts.

235 CGWs events were found from January 2013 to August 2015 in IMAV/VISI O₂ A-band (762 nm) data. The method above was applied to all the events to derive the wave parameters, horizontal wavelength and maximum radius, to study the characteristic of the CGWs in the mesopause discussed in Chapter IV.

2.5.2. Data Analysis of All Sky Camera

Airglow data from Rikubetsu all sky camera was used in Chapter III to discuss the wave propagation in different layers. From the successive measurements of airglow images taken by an all sky camera, we can estimate spatial scales, propagation directions and phase velocities of AGWs in the mesopause region and the thermosphere.

The image processing to extract the wave pattern in airglow emission from the raw images is done with several processes. First, bright stars are attenuated from the images by using a median filter [Garcia *et al.*, 1997; Coble *et al.*, 1998, Suzuki *et al.*, 2007]. In this step, when the count difference between the raw pixel count and the median of 20 x 20 surrounding pixels was larger than the mean raw count of the whole image, then the raw count was replaced with the median count. The next step is the background continuum subtraction. The background counts are caused by emissions from the sky, including light scattered by dust, from urban areas, and from the atmospheric continuum emission.

Finally, the airglow images were projected into the geographical coordinates with an area size of 512 x 512 km by using the spatial calibration determined with the star catalog and assuming the altitude of the airglow was 86 km for OH and 96 km for OI (557.7 nm). For the detail step by step of image processing please refer to Suzuki *et al.*, 2007. **Figure 2.14** shows the example of the differential of two successive images image of OI 557.7 nm, taken at Rikubetsu at 1102-1104 UT on 18 October 2012, and the projected image onto the geographical grid. In this image, one pixel around the zenith corresponds to 1 km in the geographical coordinate system.

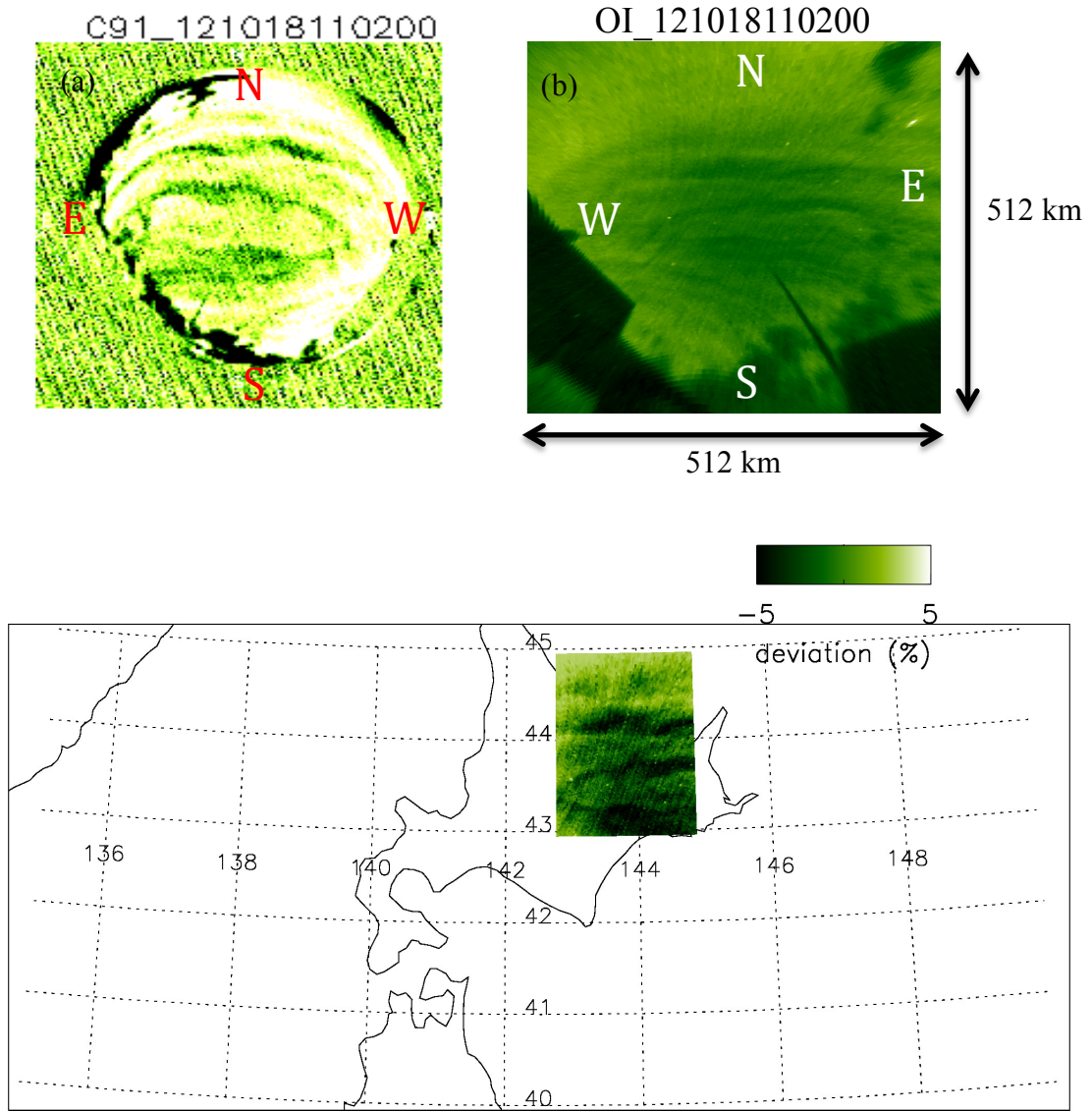


Figure 2.14. (a) An example of the differential of two successive images of OI 557.7 nm, taken at Rikubetsu at 1102-1104 UT on 18th October 2012. (b) Same as (a), except that it was projected onto the geographical grid with a size of 512×512 km. (c) The OI 557.7 nm in (b) in the geographical map, assuming the altitude of airglow layer as ~96 km.

The horizontal wavelength (λ_h) was calculated by using the same fitting method as the IMAF/VISI data. By utilizing several successive images and background wind, the apparent phase speed (c) and intrinsic period ($\tau = \lambda_h / (c - u)$) were estimated. The

vertical wavelength (λ_z) was derived using the dispersion relation of gravity wave [Hines, 1960] with the background wind. The equation is given by

$$m^2 = \frac{N^2}{(c-u)^2} - k^2 - \frac{1}{4H^2} \quad (2.4)$$

$$\lambda_z = \frac{2\pi}{m} \quad (2.5)$$

where N , k , H and m are the Brunt-Väisälä frequency, horizontal wave number, scale height, vertical wave number and u is the background wind. Since there is no background temperature measurement, we assumed that the N has a constant value of $2\pi/5$ rad/min.

Chapter III

Observation Result and Discussion Part I: Case Study

Coordinated Observation of IMAP/VISI and an All Sky Camera on Concentric Gravity Wave in the Mesopause

One of the main goals of the IMAP/VISI mission is to study the coupling processes between the lower atmosphere and upper atmosphere by AGWs. We found many interesting features on the airglow emissions showing small-scale gravity waves structure in the mesosphere and lower-thermosphere (MLT) region from 3 years observation data. One of the rare events observed with IMAP/VISI is a partial concentric gravity waves (CGW) pattern in the O₂ A-band 762-nm airglow emission occurred around 1200 UT on October 18, 2012 over northeastern part of Japan. The similar pattern was also observed with the all-sky camera at Rikubetsu in the OI 557.7-nm and OH airglow emissions.

This partial CGWs event gave a good opportunity to study the effect of background profiles, such as wind velocities, to the upward propagation mechanism of AGWs. As already stated in Chapter I, all the previous studies of CGWs events were

discussing full ring pattern, in which the effects of background profiles were suggested to be minimal. The discussion in this chapter is aiming to propose a plausible wave generation and study the effect of the background wind and temperature on the propagation mechanism of the partially CGWs event seen in different airglow layers observed from the coordinated observation between IMAP/VISI and ground-based all-sky camera.

3.1. Observation Results

3.1.1. Concentric Gravity Waves Pattern Observed by IMAP/VISI

One of the distinct AGW events observed with IMAP/VISI is an arc-like shape, apparently a part of CGW pattern, around 1204 UT on October 18, 2012. **Figure 3.1** shows the summary plot of O₂ 762 nm airglow data showing the CGW event on October 18, 2012. We found the multiple arc-like shaped airglow patterns in the differential image from 1203 UT to 1232 UT on the both FOVs data. The red rectangle in the intensity peak image indicates the region of interest for the discussion described later.

The intensity peak image in the backward FOV is mapped onto 95 km altitude in the geographic coordinate system as shown in **Figure 3.2**. The next orbit data of IMAP/VISI at 1336 UT is also shown in the same figure. In order to discuss the source of the CGWs, it is necessary to calculate the center of the circular wave fronts since we assume that the CGWs are usually generated by a point source, which should be located at the center.

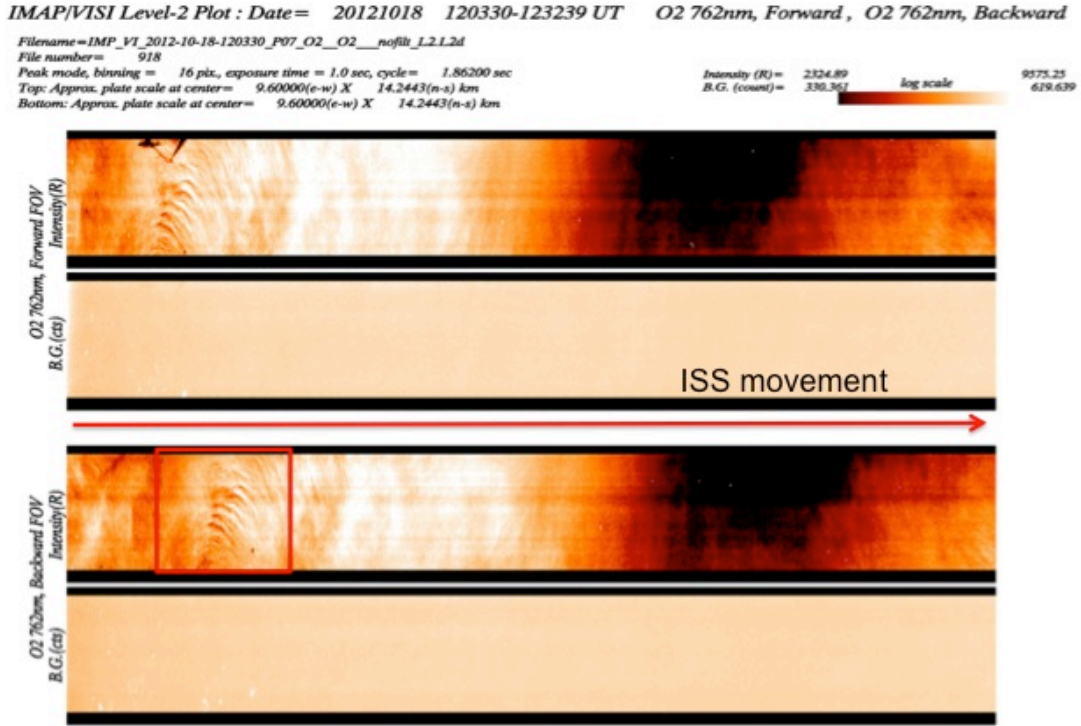


Figure 3.1. The CGWs event in O₂ 762-nm airglow emission obtained with IMAP/VISI during the period of 1203-1232 UT on October 18, 2012. The red arrow shows the direction of the ISS orbit.

To do the fitting of circle to the CGW pattern, at first we picked some points in each wave front and then applied the least squares method as described in the Section 2.5.1. On this event at 1200 UT, we estimated the best-fitted center at 33°N in geographical latitude, and 143°E in longitude with the outermost radius of the concentric airglow structure was ~1400 km as shown with the cross mark in **Figure 3.2**. The horizontal wavelength then simply calculated by averaging the radius from the center to each wave front, and it was found to be ~67 km. On the other hand, the CGWs were observed in the northeastern of Hokkaido around 1204 UT with IMAP/VISI. The next path data was obtained ~1.5 hours later starting from 1336 UT over the Honshu

Island of Japan. The IMAF/VISI data taken in this path covered the area close to the center of CGW seen in the previous path. However, there was no CGWs pattern observed with IMAF/VIS. This result indicated that the waves were generated and quickly evanescent within ~1.5 hours as the waves expanded outward or that the waves in the particular direction were filtered out.

From the results mentioned above, we propose several initial guesses as follows:

(1) it is reasonable to assume that the CGWs seen in O₂ 762-nm emission data is caused by a localized source. Convective activities in the lower atmosphere might be the source of CGWs. (2) The CGWs are categorized as small-scale GW (horizontal wavelength ≤ 100 km [e.g., *Taylor et al.*, 1995; *Nakamura et al.*, 1999; *Walterscheid et al.*, 1999]) as the calculated horizontal wavelength was found to be ~67 km. (3) The intrinsic period of this CGW should be a short period (~5-20 min), since only short period gravity wave can propagate up to mesopause region [e.g., *Walterscheid et al.*, 1999]. The ground-based measurement data can provide good estimation of duration, period, and propagation velocity of gravity waves. (4) It seems the background wind between the source and the airglow layer is relatively weak that allows the waves to propagate upward to the mesopause, yet enough to alter the shape of the ring pattern [e.g., *Taylor et al.*, 1988; *Sentman et al.*, 2003; *Suzuki et al.*, 2007; *Yue et al.*, 2009].

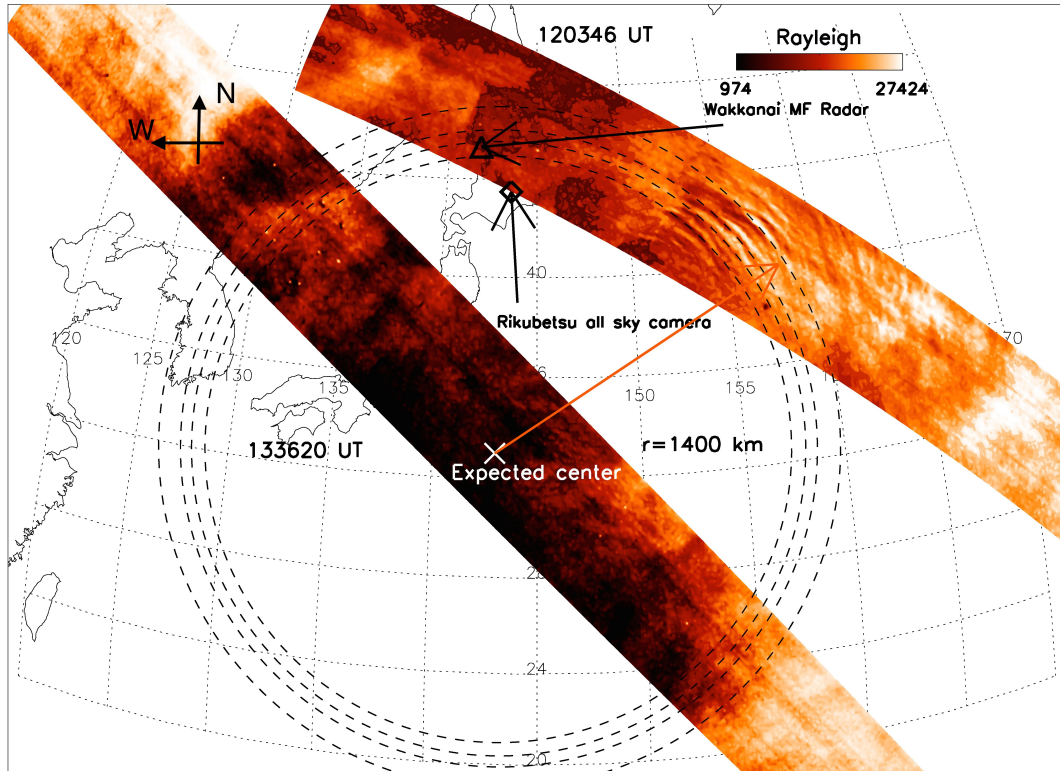


Figure 3.2. Map of the backward FOV data of IMAF/VISI at 1203 UT and 1336 UT on October 18, 2012. Dashed lines indicate the best fitted round circle to the circular wave fronts of airglow emission. The estimated center of the circle is indicated by the cross mark. The red arrow represents the outer radius of the circle from the expected center (~ 1400 km). The diamond marks show the location of the Rikubetsu all sky camera and the Wakkanai MF radar.

The gravity wave pattern seen in the O_2 762-nm emission data was not a full circle, only a part of the circle forming an arc-like shaped structure. This fact suggests that the waves pattern was disturbed and could only propagate toward particular direction due to the wind filtering effect. We compared the observation data from IMAF/VISI with the ground-based all-sky camera data at Rikubetsu to evaluate the suggestions (2) and (3). The meteorological satellite data were used to check the source

of CGWs to prove suggestion (1). The wind data from MERRA and Wakkanai MF radar were used to support suggestion (4). The results are given in the following subsections.

3.1.2. Concentric Gravity Waves Patterns in OH-band and OI 557.7-nm Image Data at Rikubetsu

The similar arc-like shaped airglow patterns were also observed in the OH-band and OI 557.7-nm data obtained with the all-sky camera at Rikubetsu during the period of one hour before the conjunction with ISS (~1100-1200 UT) on October 18, 2012. However, the wave didn't appear on the OI 630 nm emission. This may indicate that the wave broke around the mesopause and could not propagate up to thermosphere. **Figure 3.3** shows the deviation of 1-hour running average plots of OH-band and OI 557.7-nm when the CGWs were observed from 1100 to 1200 UT. After 1200 UT, the sky was cloudy. We suggested that the arc-like shaped airglow pattern seen at Rikubetsu were part of CGWs obtained by IMAF/VISI since these happened almost simultaneously and the field-of-view of Rikubetsu data was overlapped with the IMAF/VISI data (see **Figure 3.4**). The advantage of ground-based all-sky camera is to examine the motion of AGW by from successive image data. From 1102 UT, the AGW patterns in OH image data appeared to be moving in the northeastward direction. As for OI 557.7-nm image data, the similar pattern was observed from 1103 UT until the clouds covered the sky at 1155 UT.

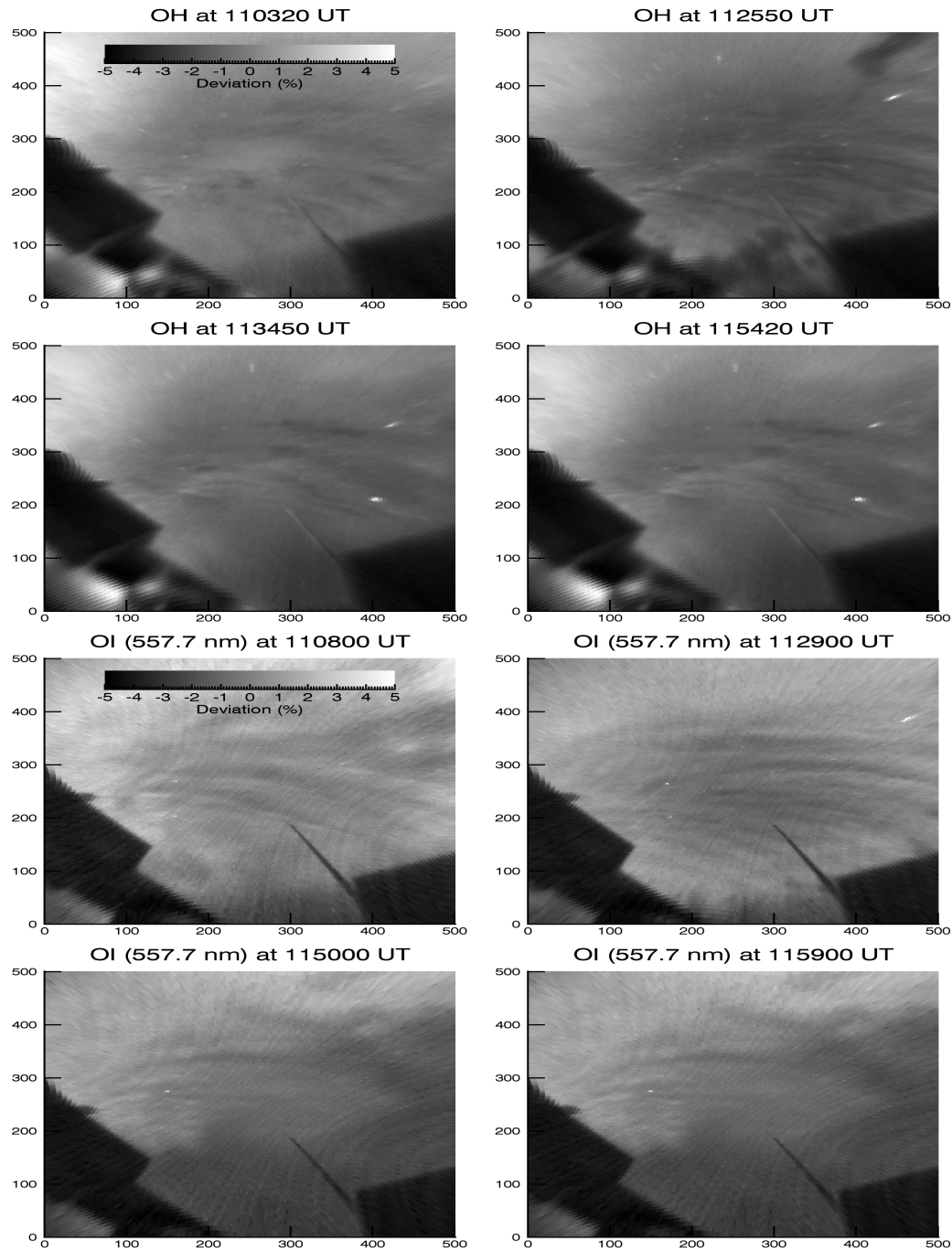


Figure 3.3. Sequential images of OH-band (top) and OI 557.7-nm emission (bottom) showing the deviation of 1-hour running average during the period of 1103 – 1159 UT on October 18, 2012. The emissions were mapped by assuming that the airglow layer of OH-band is ~ 86 km and OI 557.7-nm is ~ 96 km.

The CGWs were observed during the period from 1102 UT to 1200 UT (~58 min, even though the cloud began to appear around 1155 UT but a small part of the CGWs was still observed at ~1200 UT) in the OH-band data, and from 1103 UT to 1156 UT (~53 min) in the OI 557.7-nm emission data. On the other hand, IMAP/VISI measured the CGW pattern in the O₂ 762-nm emission around 1203 UT beyond the FOV of all-sky imager at Rikubetsu (several hundred km away). Unfortunately, the timing of IMAP/VISI data did not exactly match to the Rikubetsu data due to the clouds.

The wave parameters, such as horizontal wavelength (λ_h) and apparent wave speed (c), were estimated manually from the successive image data at Rikubetsu. The horizontal wavelength and phase velocity for OH data are ~50 km and ~105 m/s, respectively. For OI 557.7-nm data, they are ~51 km and ~96 m/s, respectively. These wave parameters suggest that the CGWs observed in OH-band and OI 557.7-nm emission have small scale and short periods. This fact is consistent with our initial suggestions (2) and (3) based on the IMAP/VISI O₂ 762-nm emission data.

Using the observed parameters and the background wind obtained from the Wakkanai MF radar, the intrinsic wave periods ($\tau = \lambda_h / (c - u)$) were estimated for OH data and OI 557.7-nm data assuming the emission altitudes of 86 km and 96 km, respectively. The estimated intrinsic wave periods are 8.6 min and 9.2 min for OH and OI 557.7-nm data, respectively. The vertical wavelength was calculated to be ~42 km from the linear dispersion relation for a gravity wave in Equation (2.4).

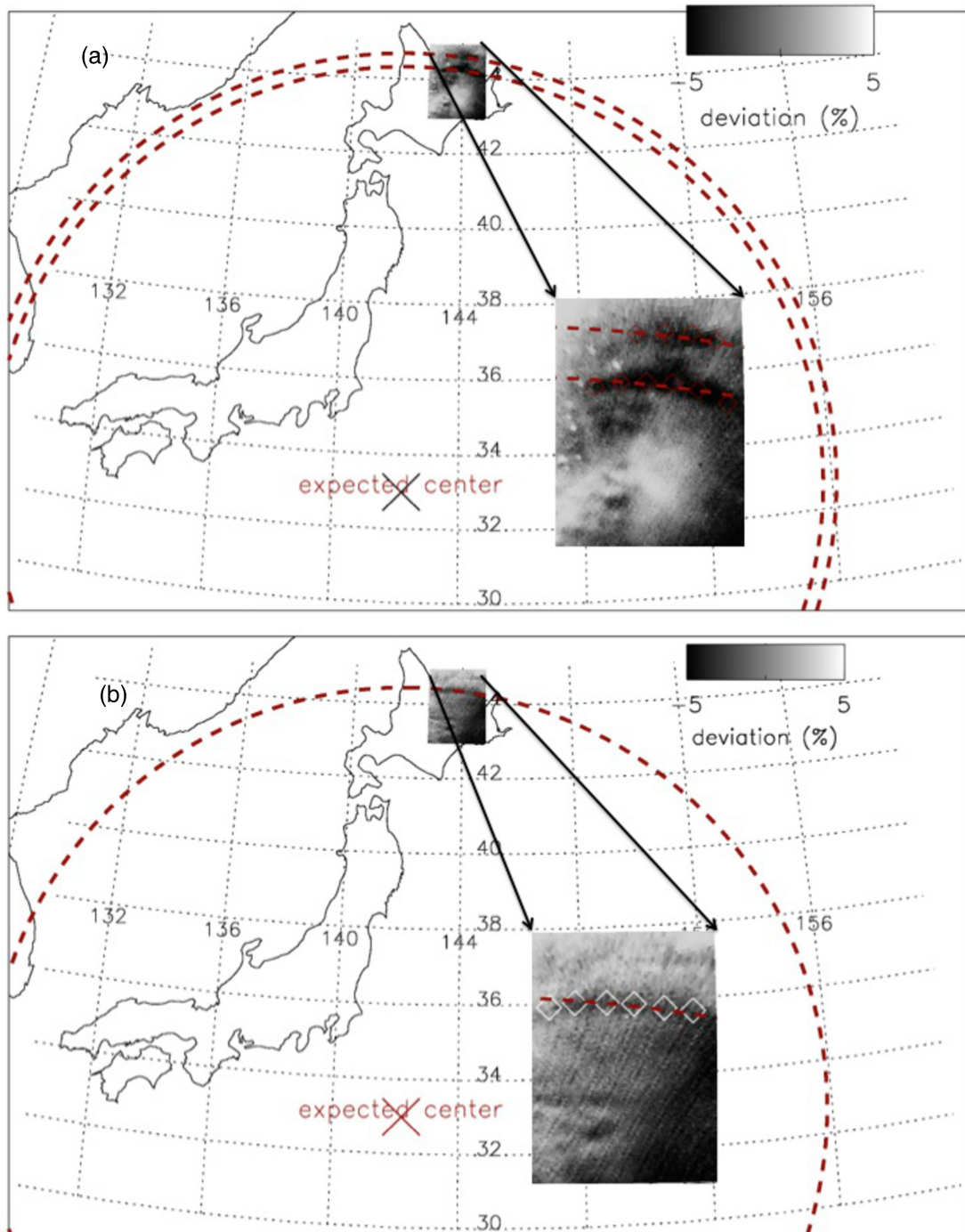


Figure 3.4. Mapped airglow images, fitted circles and estimated center positions (cross mark) for OH data (a) and OI 557.7-nm data (b) of the CGWs event at Rikubetsu on October 18, 2012.

The innermost ring radius of the concentric pattern determines the elevation angle of upward propagation (θ) [Dewan *et al.*, 1998]. From the IMAP/VISI data we only observed the part of the concentric pattern, which was far away from the source. From the data we can only determine the outermost ring radius, which is ~ 1400 km. Therefore it is difficult to calculate the elevation angle from the IMAP/VISI data itself. However, the angle can be calculated from observed wave period from the ground-based observation (τ) and Brunt-Väisälä period (τ_B) based on the simplified dispersion relation of *Hines* [1960].

$$\theta = \tan^{-1} \left[\left(\frac{\tau}{\tau_B} \right)^2 - 1 \right]^{-1/2} \quad (3.1)$$

The wave period observed from Rikubetsu data is ~ 9.2 min and assuming that the Brunt-Väisälä period (τ_B) ~ 5 min, the angle was found to be $\sim 42.5^\circ$.

To determine the center of CGWs, the same procedure as applied for the O₂ 762-nm of IMAP/VISI data was used for Rikubetsu OH and OI data. The mapped airglow image and fitted circle are shown in **Figure 3.4** for OH data (a) and OI 557.7-nm data (b). The estimated center for the CGWs in OH emission is at 33°N in latitude and 142°E in longitude with the outermost radius is ~ 1200 km, and for the CGWs in OI 557.7-nm is at 35°N in latitude, and 143°E in longitude with a radius of ~ 1100 km. Compared the center location and radius with those estimated by IMAP/VISI (33°N , 143°E and ~ 1400 km), it is obvious that the CGWs in OI 557.7-nm, OH and O₂ 762 nm emissions have the same source.

Considering the small-scale horizontal wavelength and elevation angle, it is almost impossible for the gravity wave to propagate to a very long distance directly (such as ~ 1400 km). This indicates that the CGWs observed both by IMAP/VISI and

Rikubetsu all sky imager could be ducted since the duct-mode atmospheric gravity waves can propagate for long distance [e.g. *Taylor et al.*, 1993; *Walterscheid et al.*, 2001]. The detailed discussion on ducted propagation will be given in the Section 3.2.2 using the Wakkanai wind data for a possibility of wind ducted mode and SABER data for thermal ducted mode.

3.2. Discussion

3.2.1. Relationship between CGWs Patterns and Convection Activity Map

Convective activity in the lower atmosphere, i.e., the troposphere, such as a development of cumulonimbus cloud, typhoon and tornado, are potentially the main sources of CGWs considering the typical spatial scale (~tens to hundreds km) of these activities. The estimated centers of three different data set (O_2 762-nm emission taken by IMAF/VISI, OH and OI 557.7-nm emission taken by the Rikubetsu all-sky imager) were found to be 33 ± 2 °N in latitude and 143 ± 2 °E in longitude. Here, we analyzed the meteorological data obtained with MTSAT and TRMM over Japan covering the center of CGW. **Figure 3.5** (a) shows the convective index derived from the top-cloud temperature data of MTSAT satellite at 1100 UT on October 18, 2012 with the Equation 2.1. The data show a deep convective activity covering wide area of the Honshu Island, which likely associated with the typhoon located in the southern part of the Honshu Island. The typhoon could be one of the sources of the CGWs, but the location of typhoon eye (30° N, 136° E) was too far to the south from the estimated center of CGWs. Therefore we suggest that the source of this CGWs is the deep convective activity over the Honshu Island (index value up to 40) instead of the typhoon

eye. This is consistent with our initial suggestion (1), which suggested the source was convective activity in the lower atmosphere.

The estimated center (marked with a cross in **Figure 3.5** (a)) is probably shifted from the active convective area likely due to the strong eastward wind around the tropopause, which is discussed in detail in Section 3.2.2, and shown in **Figure 3.8** (a). The convective index strongly correlates with the development of the convective clouds, e.g. the cumulonimbus cloud, which usually connected with precipitation [Ohsawa *et al.*, 2001]. The development of the convective cloud involves a strong vertical motion that possibly generates the CGWs. In the most cases, within an hour, in the location of the convective cloud, heavy precipitation occurs. Therefore, precipitation data can be used to examine the development of the convective cloud and the generation of the CGWs. Figure 3.6 shows the successive 3-hourly precipitation data obtained by TRIMM from 0600 UT to 1500 UT on October 18, 2012.

The only highly localized precipitation was observed up to 19.7 mm/hr at 0600 UT around the expected center was located a few hundred km (~500 km) to the west around (33°N, 136°N). Thus, this could be the source of the CGWs. The time difference between the beginning of the highly precipitation rate (0600 UT) and the observation of the CGWs over Rikubetsu is ~6 hours. However, only looking from the precipitation data without a ray tracing model and simultaneous background wind measurement, we cannot determine the exact location or time (where and when) of precipitation directly correlated with the launch of CGWs.

A ray-tracing model can estimate precisely the time needed for the CGWs to propagate from its source in the lower atmosphere to the observed emission layer in the MLT region, and also estimate the horizontal distance from the source. However, in the present study, we made a rough estimation of the time needed to propagate from the

source to the outermost ring of airglow layer (r_{max}) based on the simple propagation geometry of CGWs [Dewan *et al.*, 1998] given by

$$T = \frac{r_{max}}{v_{gx}} \quad (3.2)$$

$$v_{gx} = \frac{\partial \omega}{\partial K_x} = \left(\frac{\lambda_x}{\tau} \right) \left[1 - \left(\frac{\tau_B}{\tau} \right)^2 \right] \quad (3.3)$$

where T is the propagation time, r_{max} is the outermost ring (~ 1400 km from IMAV/VISI data), K_x is the horizontal wavenumber, λ_x is the horizontal wavelength, τ_B is the Brunt-Väisälä period and τ is the observed period (9.2 min from Rikubetsu data). The horizontal group velocity (v_{gx}) is found to be ~ 65 m/s from Rikubetsu data. The propagation time T is then calculated to be around 6 hours. This time is consistent with the beginning of the high precipitation activity, i.e., ~ 0600 UT on 18 October 2012, as seen in **Figure 3.6**.

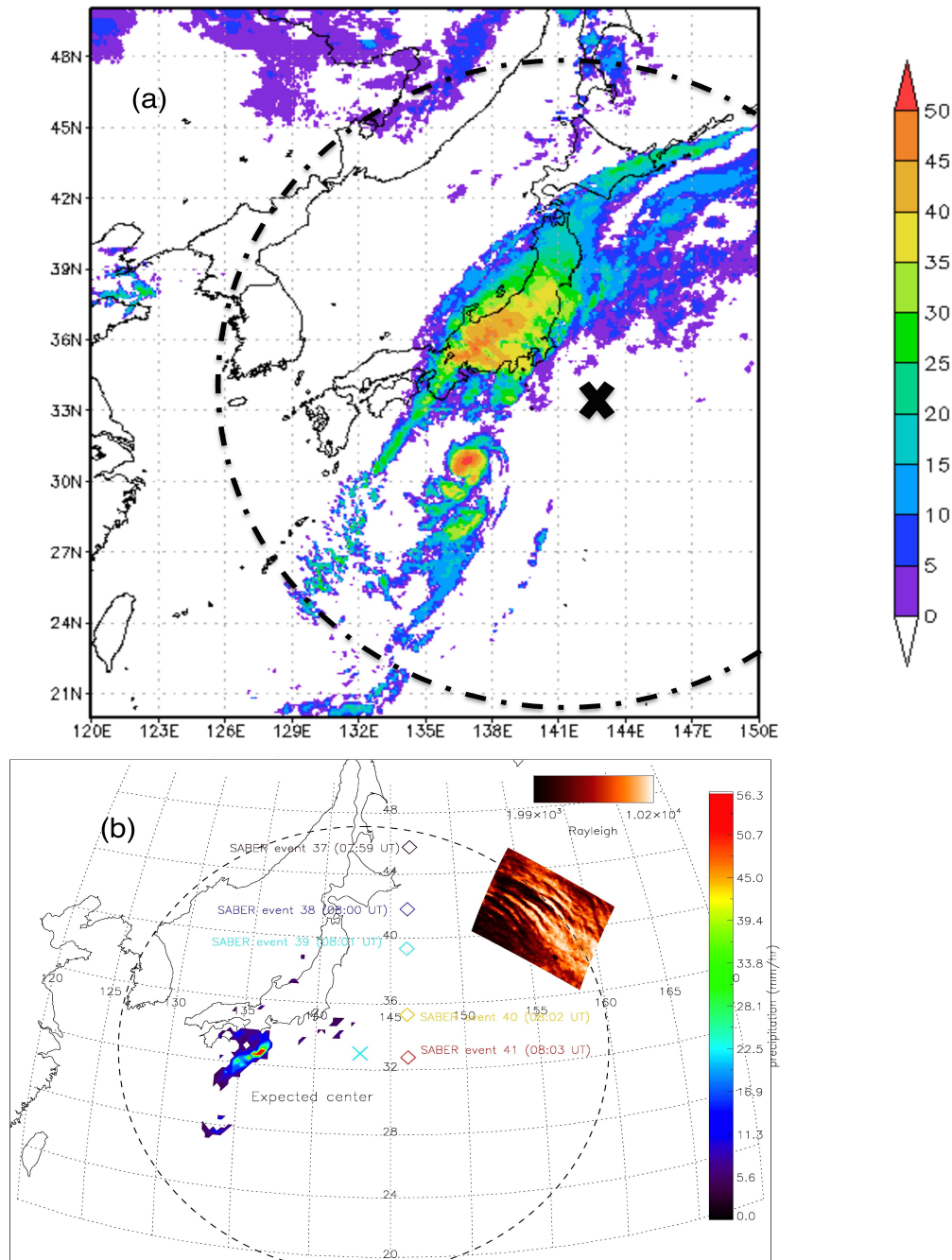


Figure 3.5. The convective index derived from the TBB data of MTSAT satellite at 1100 UT on October 18, 2012 (a). Dash-dotted line represents an approximate circle fitted to the CGW pattern, and a cross mark is its center. (b) TRMM data at 0600 UT plotted together with CGWs even in O₂ 762-nm and location of SABER data available during the event.

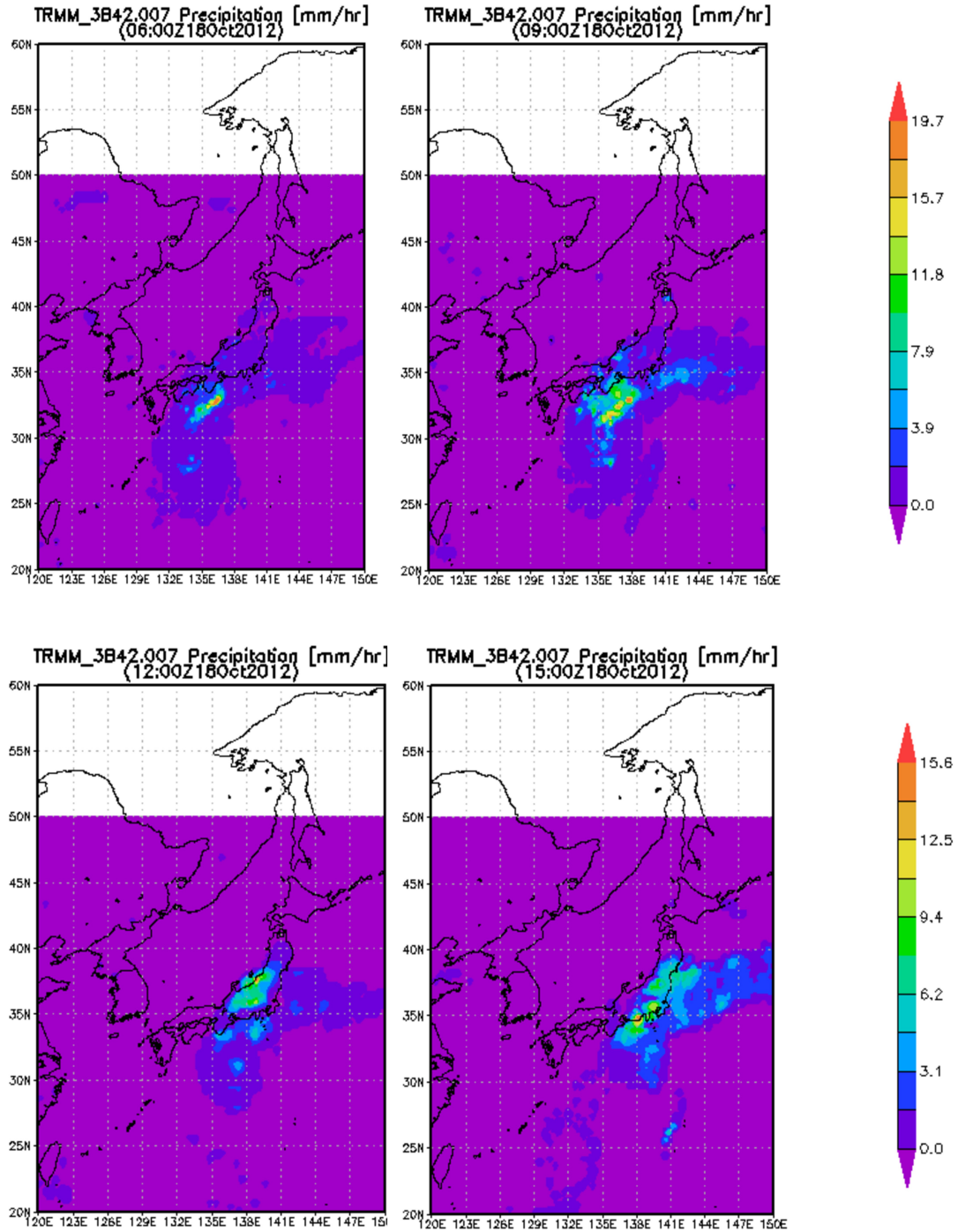


Figure 3.6. The precipitation data (mm/hr) from the TRMM satellite during the period from 0000 to 1500 UT, October 18, 2012.

3.2.2 Background Profile Condition and Wave Propagation Mechanism

Although the localized convective activity, such as convective cloud, typhoon or tornado, frequently occurs, the CGWs were relatively rare to observe from the ground-based observation in the upper atmosphere [Suzuki *et al.*, 2007]. However, from the IMAP/VISI observation data, we found that these type gravity waves are not very rare. The reason why the ground-based observation could only observe a few events is due to the restrictions of ground-based measurement; limited field of view (FOV), no observation over the ocean area and also the ground-based observations depend heavily on the weather conditions. The detailed statistical study on these events is given in Chapter IV.

Despite the relatively common occurrence, the CGWs' upward propagation is strongly affected by the background wind profile [e.g. Suzuki *et al.*, 2007; Yue *et al.*, 2009; Vadas *et al.*, 2010]. In this study, we examined the background wind profile in the lower and middle atmosphere (0-60 km) from MERRA data and that in the MLT region (84-102 km) from the Wakkanai MF radar. Figure 3.7 shows the background zonal wind profile on the October 18, 2012 event from both MERRA and Wakkanai data. Black dashed-line represents the zonal wind derived from MERRA data over Wakkanai (45°N, 141°E) at 1200 UT (time of CGWs observation) while the red dashed-line represents the zonal wind data over the center of CGWs (33°N, 143°E) at 0600 UT (time of generation of the CGW source in the lower-atmosphere). The zonal wind in the MLT region obtained from Wakkanai MF radar shown in the solid red line. The positive wind speed represents the eastward wind direction while the negative value shows the westward direction.

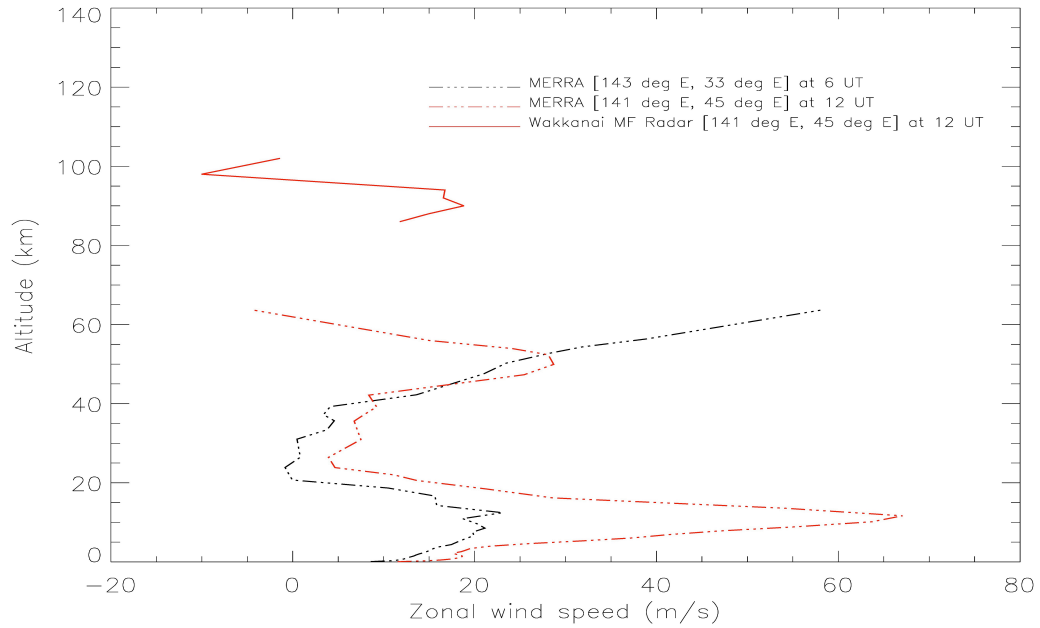


Figure 3.7. Zonal wind profile obtained from MERRA data over the expected center (33°N , 143°E) (0-60 km) at 0600 UT (black dashed line) and over Wakkanai (45°N , 141°E) at 1200 UT (red dashed line). Zonal wind profile obtained from Wakkanai MF Radar (84-102 km) at 1200 UT is shown in solid red line.

From the **Figure 3.5** (b) we can see that the expected center (33°N , 143°E) was shifted eastward about ~ 500 km from the active convective area (33°N , 135°E). This fact suggests that there might be a strong eastward zonal wind in the lower atmosphere. *Vadas et al.* [2009] stated in her model study that an eastward wind with the velocity >30 m/s can shift the center of the CGWs up to 200 km to the east. Therefore, in this study we first looked at the background wind conditions around the expected center to analyze the effect of wind in the lower atmosphere to the propagation direction of the CGWs.

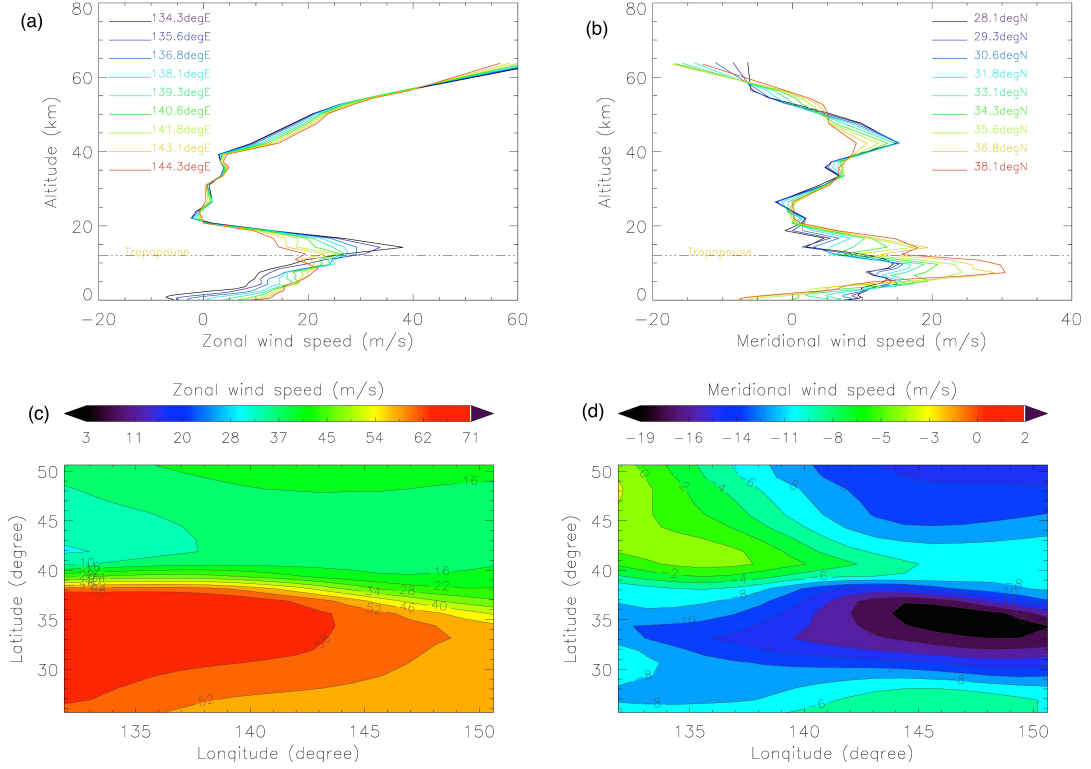


Figure 3.8. Background wind profile obtained from MERRA at 0600 UT on 18 October 2012: (a) Zonal wind speed from 0-60 km at the latitude of 33°N with longitudinal range from 134° to 144°E , (b) meridional wind speed from 0-60 km at longitude of 143°E with latitude from 28° to 38°N , (c) contour of zonal wind speed and (d) contour of meridional wind speed at the altitude of 60 km.

Figure 3.8 (a) shows the zonal wind speed at 33°N along the longitude range from 134° to 144°E at 0600 UT on 18 October 2012. Strong eastward wind with a speed of 40 m/s was seen around the source location and slowing down to 20 m/s around the expected center. This fact could be the reason why the wave center was shifted eastward. Upward propagating gravity waves from the lower atmosphere may encounter a “critical layer” which prevents the waves to propagate further upward [e.g., *Taylor et al.*, 1993]. This filtering effect can occur at any altitude level when the horizontal wind

speed in the direction of the gravity wave propagation is equal to the observed horizontal phase speed ($c=u$). When the horizontal wind along the propagation direction is equal to the c , according to the dispersion relationship given in the Equation (2.4), the m^2 is infinity, hence the gravity wave do not propagate upward anymore. On the other hand, when a strong wind blows in the opposite direction of the gravity wave propagation that $|c-u|$ becomes enormous which leads the m^2 to negative (m is imaginary), the gravity wave is evanescent. At the altitude when the $m=0$, the reflection of gravity wave occurs.

Figure 3.9 shows the vertical profile of m^2 as a function of neutral wind (u). Here, m^2 was calculated based on the dispersion relationship theory given in Equation (2.4), adopting the wave parameters derived from the Rikubetsu all-sky camera (horizontal wavelength of ~ 50 km and wave speed ~ 100 m/s) and assuming the background wind from -60 to 60 m/s. The value of m^2 starts becoming negative when $u < -40$ m/s, which means at the altitude when the background wind speed is 40 m/s in the opposite direction of the wave propagation, the gravity wave is reflected.

From the **Figure 3.8(a)**, zonal wind speed above the center in the altitude range of 12 - 40 km is varying from 0 - 20 m/s, much smaller than the apparent horizontal speed of CGWs at the emission layer as mentioned earlier (~ 96 - 105 m/s). Obviously, this relatively weak background wind above the tropopause allows the CGWs to propagate upward without encountering the critical level. The wind starts to change its direction to eastward at stratopause (~ 40 km altitude) and reaches a speed of 60 m/s around 60 km altitude. It means that the westward propagating gravity waves are reflected off while the gravity waves propagating in eastward direction are hardly affected and can propagate upward freely. This is consistent with the CGWs seen in the **Figure 3.2** where we do not see the westward direction of the CGWs pattern.

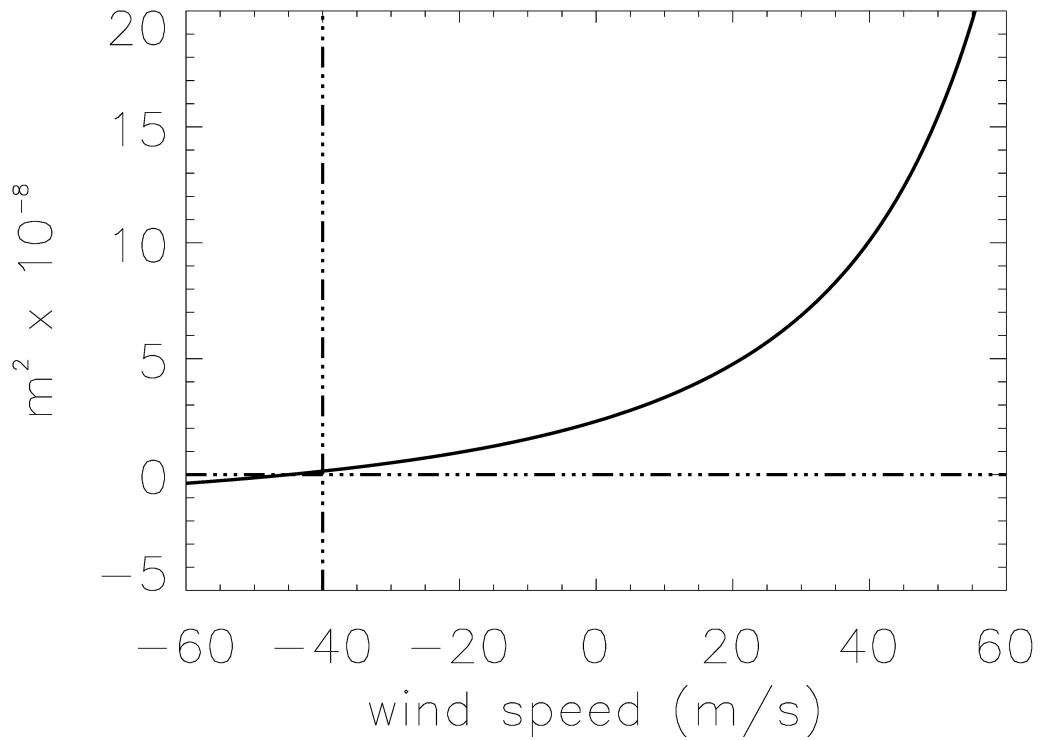


Figure 3.9. Vertical profile of m^2 calculated using the dispersion relationship for the background wind speed ranging from -60 to 60 m/s. See text for the details.

The meridional direction of the background wind is shown in the **Figure 3.8 (b)**, showing the meridional wind speed at 143°E with the altitude ranging from 28° to 38°N . Since this CGWs event was not one to one event, meaning that there was no immediate possible source in the troposphere at the expected center, here we carry out careful discussion on all the source possibilities to single out the most possible scenario. From the convective index shown in **Figure 3.5 (a)**, we notice that there was also a typhoon centering in the southern part of Honshu Island that could be the source of CGWs. As already mentioned in the Section 3.2.1, this typhoon location was a little bit too far ($\sim 830\text{ km}$) from the expected center but a strong meridional wind might shift the center in the northward direction. Therefore, we analyzed the meridional wind above the

typhoon eye to the expected center. The result shows that the northward wind velocity was insignificantly small, in the range of 0 - 14 m/s, above the tropopause along those locations throughout this period. Thus, we conclude that we rule out the possibility of the typhoon eye as the source of the CGWs.

Figure 3.8(c) and (d) show the contour of zonal and meridional wind at the altitude of 60 km obtained from MERRA data. The zonal wind shows a strong eastward wind (>50 m/s) above the expected center, indicating that the westward propagating waves could be reflected off (as already mentioned above), while the meridional wind shows a northward velocity with a speed up to 14 m/s. This northward wind was likely had a little affect for the waves moving southward, and therefore, the waves could be expanding in the southward direction as well. However, unfortunately, there was no observation data in the southward direction of the estimated center and we could not confirm this scenario.

Figure 3.10(a) shows the zonal wind data in the MLT region (84-104 km) for 1000 UT-1200 UT estimated from the Wakkanai MF radar data. The CGWs began to appear around 1100 UT for both OH (86 km) and OI 557.7-nm (96 km) emissions at Rikubetsu. The absolute values of zonal winds in the MLT region during the period from 1000 to 1200 UT were always less than ~ 20 m/s as shown in **Figure 3.10(a)**. The wind direction at 1100 UT dominated by the westward wind with the velocity less than ~ 10 m/s. The apparent speed estimated from the eastward propagating CGWs is ~ 90 -105 m/s, much faster than the westward background wind. This fact suggests that these CGWs propagating upward could pass through the westward winds in the MLT region.

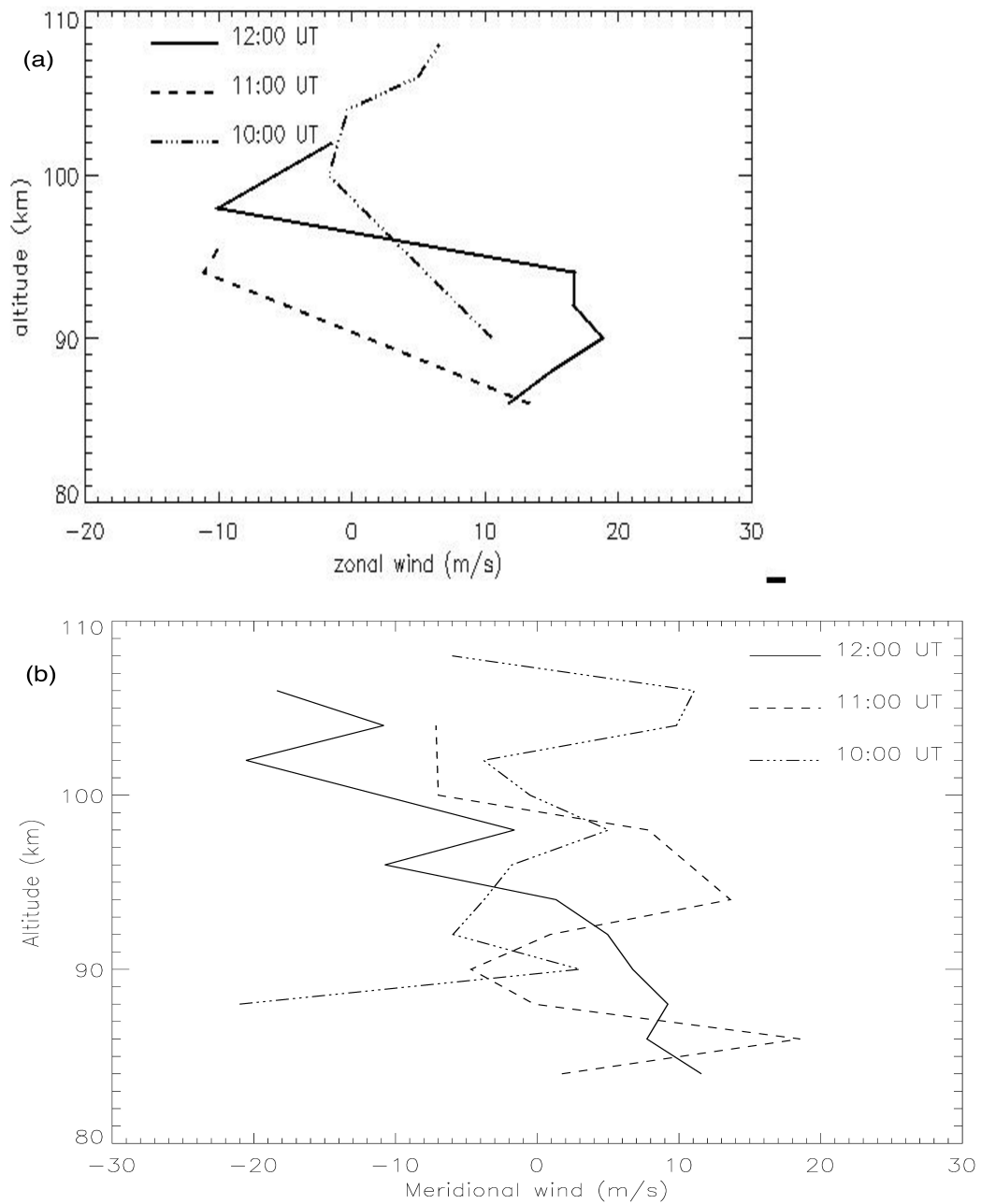


Figure 3.10 (a) Zonal wind profiles in the MLT region derived from the MF radar at 10:00-12:00 UT on October 18, 2012. Eastward wind is positive. (b) Meridional wind profiles at 1000-1200 UT from the Wakkanai MF Radar.

The hodograph at the altitudes of 86 km and 94 km showing the background wind direction is shown in **Figure 3.11**. The southeastward wind velocity dominates the

wind direction in both layers. In the altitude of OH emission (86 km), the wind velocity is increasing from 1000-1100 UT with the velocity of ~ 5 -15 m/s. From 1100-1300 UT the wind increasing with the velocity varying between ~ 15 -40 m/s. Unfortunately, there is no optical data from IMAP/VISI and the Rikubetsu all-sky imager after 1200 UT. However, the perpendicular wind direction to the CGWs likely did not affect the wave propagation. Therefore, it is reasonable to consider that the northeastward propagation of CGW seen during the period of $\sim 1100 - 1200$ UT continued after 1200 UT.

The model study by *Vadas et al* [2009] showed that the CGWs near the mesopause are “squashed” or arc-like shaped if the intervening zonal wind in the altitude range of 12 - 87 km is more than ~ 20 -30 m/s. This model study is consistent with the observations with both IMAP/VISI and Rikubetsu all-sky imager and confirm our initial suggestion (4), which showed the arc-like wave pattern (see **Figure 3.2** and **Figure 3.3**) with the intervening background wind in the MLT region less than ~ 20 m/s.

Based on the analyses mentioned above, the AGWs were likely generated by the convective activity seen in the lower atmosphere (**Figure 3.5 (b)**), and then the strong eastward wind around the tropopause shifted the waves eastward. The relatively low winds above the tropopause allow the wave to propagate upward but then the strong zonal in the altitude of 60 km reflected off the waves expanding in the westward direction, making the waves could only expanding in the eastward and northward directions, and might be in the southward direction up to the mesopause.

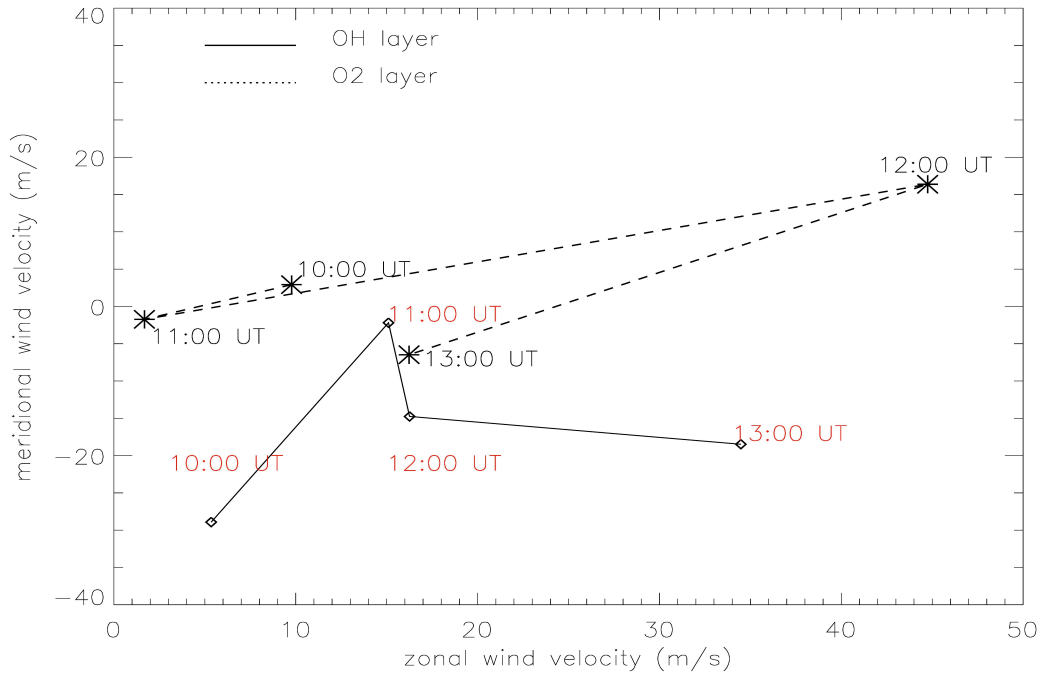


Figure 3.11. Hodographs at altitudes of OH emission layer at 86 km (solid line) and O₂ emission layer at 95 km (dashed line) for 1000-1300 UT. Positive meridional wind means northward, and positive zonal wind means eastward.

However, there is still one question remaining: How could such a small-scale waves propagate for a long distance up to ~1400 km from its source? One possible scenario is that the waves were propagate obliquely and when reached the mesopause height, the waves were ducted and continued to propagate horizontally until reached the distance when they were observed by IMAP/VISI and Rikubetsu all sky camera.

Ducting region is described as a region with $m^2 > 0$ between two evanescent regions in the atmosphere. The wave is vertically evanescent when $m^2 < 0$; therefore the waves cannot propagate further upward. There are two possibilities of ducting mode, wind ducting and thermal ducting [e.g. *Walterscheid et al.*, 2001; *Nappo*, 2002; *Simkhada et al.*, 2009; *Snively et al.*, 2008]. Based on the dispersion relation in Equation

(2.4), the evanescent regions may arise due to variation in the wind ($u_0(z)$), which is called the wind duct mode, or Brunt-Väisälä frequency ($N(z)$), which we call the thermal duct mode. In pure wind duct mode, the variation of the wind dominates the variation of the Brunt-Väisälä frequency. Several case studies of wind duct mode have been done in the past [e.g. *Isler et al.*, 1997; *Simkhada et al.*, 2009]. **Figure 3.12** shows an example of wind duct mode reported by *Simkhada et al.* [2009]. They reported a small-scale gravity waves with horizontal wavelengths $\lambda_H \sim 15\text{-}20$ km observed at Maui on 5 July 2003. From **Figure 3.12** we can see that the wind duct mode needs a strong wind speed on the opposite direction of the wave propagation which depends on the wave parameters like horizontal scale and wave speed as described in the Equation (2.4). However, in the case of CGWs event, the background wind along the propagation track is relatively small. Thus, the wind duct for this type of gravity wave is unlikely.

To confirm this theory, we simulated the required conditions of background wind strength needed to form a duct region for the CGWs case on 18 October 2012. We calculated the background wind assuming that the N is constant and using the horizontal wavelength (~ 50 km) and wave speed (~ 100 m/s) obtained from the observation. The result is shown in **Figure 3.9**, which suggests that the ducted region exists when wind velocities below and above the nightglow heights, i.e., altitudes of ~ 80 km and ~ 100 km respectively, were southward (opposite to the CGWs direction which is northward) with the speed more than 40 m/s ($m^2 < 0$) and wind velocity at the nightglow height was weak with the speed of 0 to ~ 20 m/s ($m^2 > 0$).

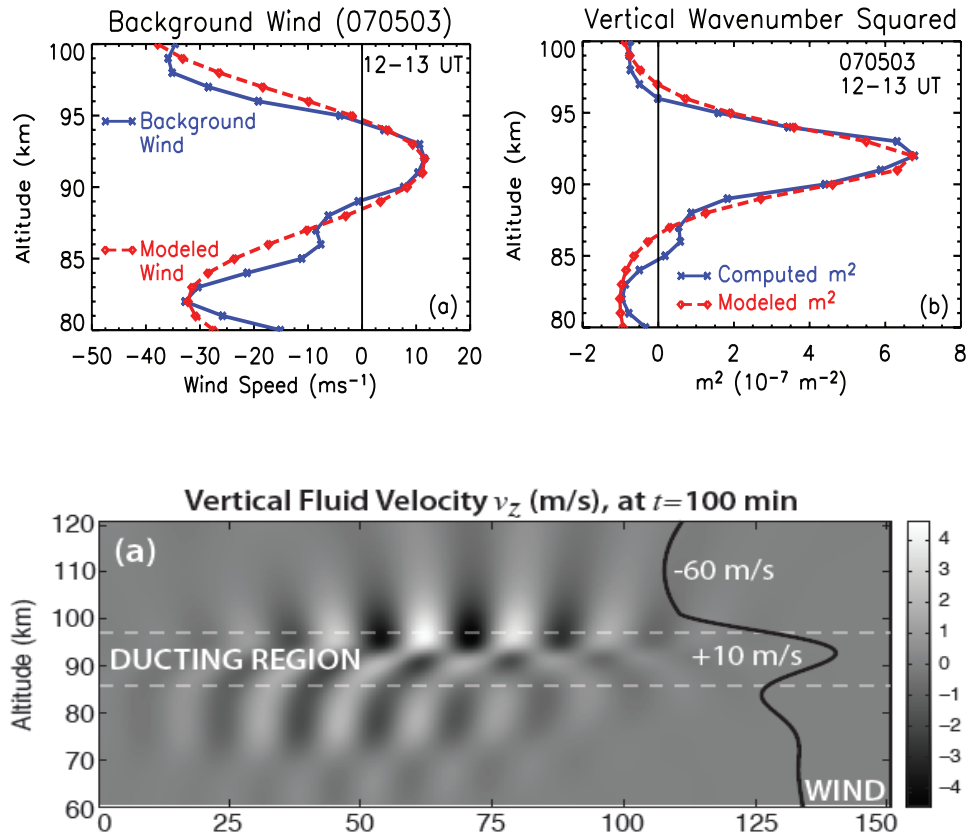


Figure 3.12. Background winds and squared vertical wavenumber analysis for 5 July 2003 small-scale gravity wave event reported by *Sikhamda et al.*, 2009 (top), which shows a strong wind inversion in the opposite direction of the wave propagation that lead the negative value of m^2 at ~ 87 km and ~ 97 forming a duct region. The model simulation for the same event depicts upward wave propagation through the mesopause region (bottom).

However, from the meridional wind observation from Wakkanai MF radar shown in **Figure 3.10(b)** we can see that the wind speed was less than 20 m/s propagating southward around the mesopause region. This relatively weak background wind resulted only in positive squared vertical wavenumbers throughout the mesopause and lower thermosphere region (80-110 km), in which the wave can still propagate upward in this region. Therefore, instead of considering the possibility of wind-ducting

mode, we now discuss the thermal ducting mode where the strength of thermal duct depends mostly on the Brunt-Väisälä frequency, i.e. the thermal duct mode occurs when there is a sharp inversion of temperature gradient.

Walterscheid et al. [2001] reported a nonlinear numerical study on possible thermal ducted of small-scale gravity wave ($\lambda_h \sim 25$ km) generated by a storm that observed over Adelaide that was believed to have traveled southward ~ 2000 km from its source in the tropic. Their result showed two duct regions in the stratosphere (20-60 km) and lower thermosphere (60-140 km) shown in **Figure 3.13**. *Snively et al.* [2008] validated this study by conducting analytical and numerical simulations to explain the linear coupling between the stratospheric and lower thermosphere ducts. The thermospheric profile such as the neutral density, temperature and wind for both simulations was obtained from the MSIS-E-90 model. **Figure 3.14** shows the schematic and result of model study for linear coupling between two duct regions. The result demonstrated that a simple wave tunneling is likely to be significant linear source of ducted wave propagating at high-altitude. The tunneling occurs when there is a resonance between two ducts, resulting energy exchange from one duct mode to another at the same frequency and horizontal wavelength [e.g. *Fritts and Yuan*, 1989; *Snively et al.*, 2008]. This simple coupling mechanism is effective for a short-period gravity wave generated in the troposphere to become ducted around mesopause [e.g. *Fritts and Yuan*, 1989; *Walterscheid et al.*, 2001; *Sutherland and Yewchuk*, 2004, *Snively et al.*, 2008].

In order to evaluate the thermal duct in the CGWs event on 18 October 2012, we used the temperature profile data obtained from the SABER instrument. As mentioned above, the waves were likely generated around 0600 UT, and fortunately, SABER has several simultaneous data around that time.

Table 3.1 shows the events around the wave generation time and **Figure 3.5 (b)** shows the time and location of each events mapped in the geographic coordinates. The Brunt-Väisälä frequency (N) can be derived directly from the temperature data using the following equations [Tuan *et al.*, 1979]:

$$N^2 = - \left[\frac{g}{\rho} \left(\frac{\partial \rho}{\partial z} \right) + \frac{g^2}{c_s^2} \right] \quad (3.4)$$

where ρ is atmospheric density and c_s is the sound speed. Assuming an exponentially scaled atmosphere:

$$\frac{1}{\rho} \left(\frac{\partial \rho}{\partial z} \right) = - \frac{1}{H} = - \frac{m_a g}{k_B T} \quad (3.5)$$

as

$$c_s^2 = \frac{\gamma k_B T}{m_a} \quad (3.6)$$

Therefore, N^2 can be written as

$$N^2 = \frac{g}{H} - \frac{g^2}{c_s^2} = \frac{m_a g^2}{k_B T} \left(\frac{\gamma-1}{\gamma} \right) \quad (3.7)$$

where g , and H are the acceleration due to the gravity, and scale height, respectively. γ is the ratio of specific heats, k_B is the Boltzmann's constant, T is the temperature obtained from the SABER data and m_a is the mean molecular mass (=28.96 atomic mass units).

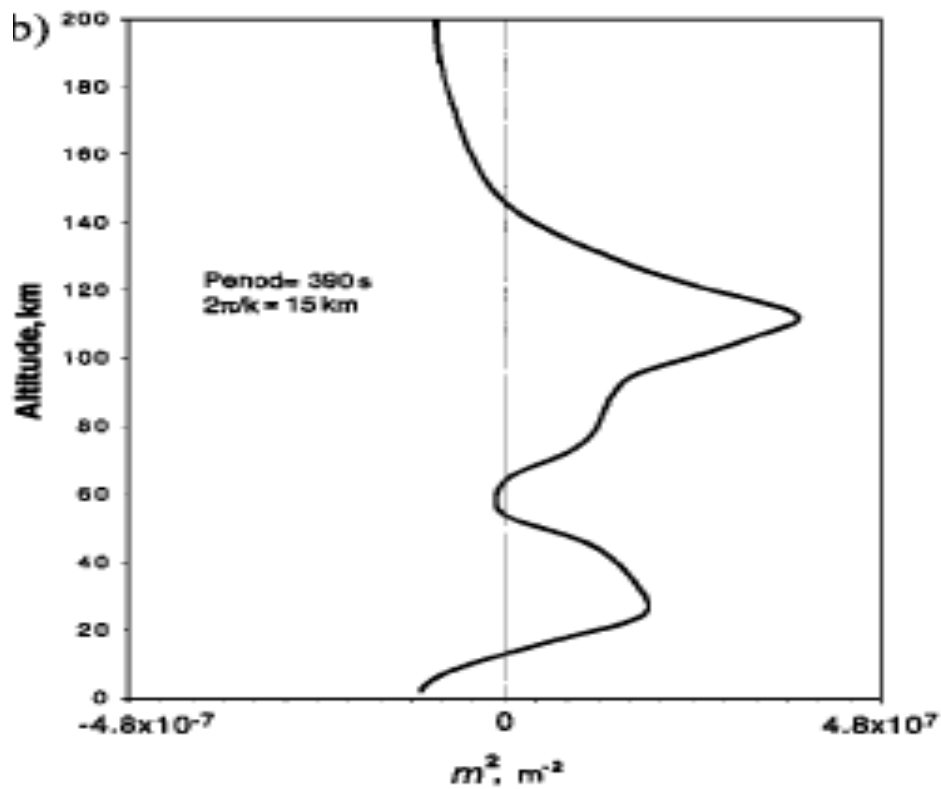


Figure 3.13. Altitude profiles of m^2 showing two duct regions in stratosphere and lower atmosphere [Waltherscheid et al., 2001].

Table 3.1. SABER data on October 18, 2012 near the expected center around the time of the wave generation. All values reference to the 90 km tangent point.

Event number	Date	Time (UT)	Latitude	Longitude
37	2012-10-18	07:59:43	45.7456	146.523
38	2012-10-18	08:00:52	41.8111	146.259
39	2012-10-18	08:01:34	39.3782	146.165
40	2012-10-18	08:02:45	35.3601	146.127
41	2012-10-18	08:03:30	32.7702	146.157

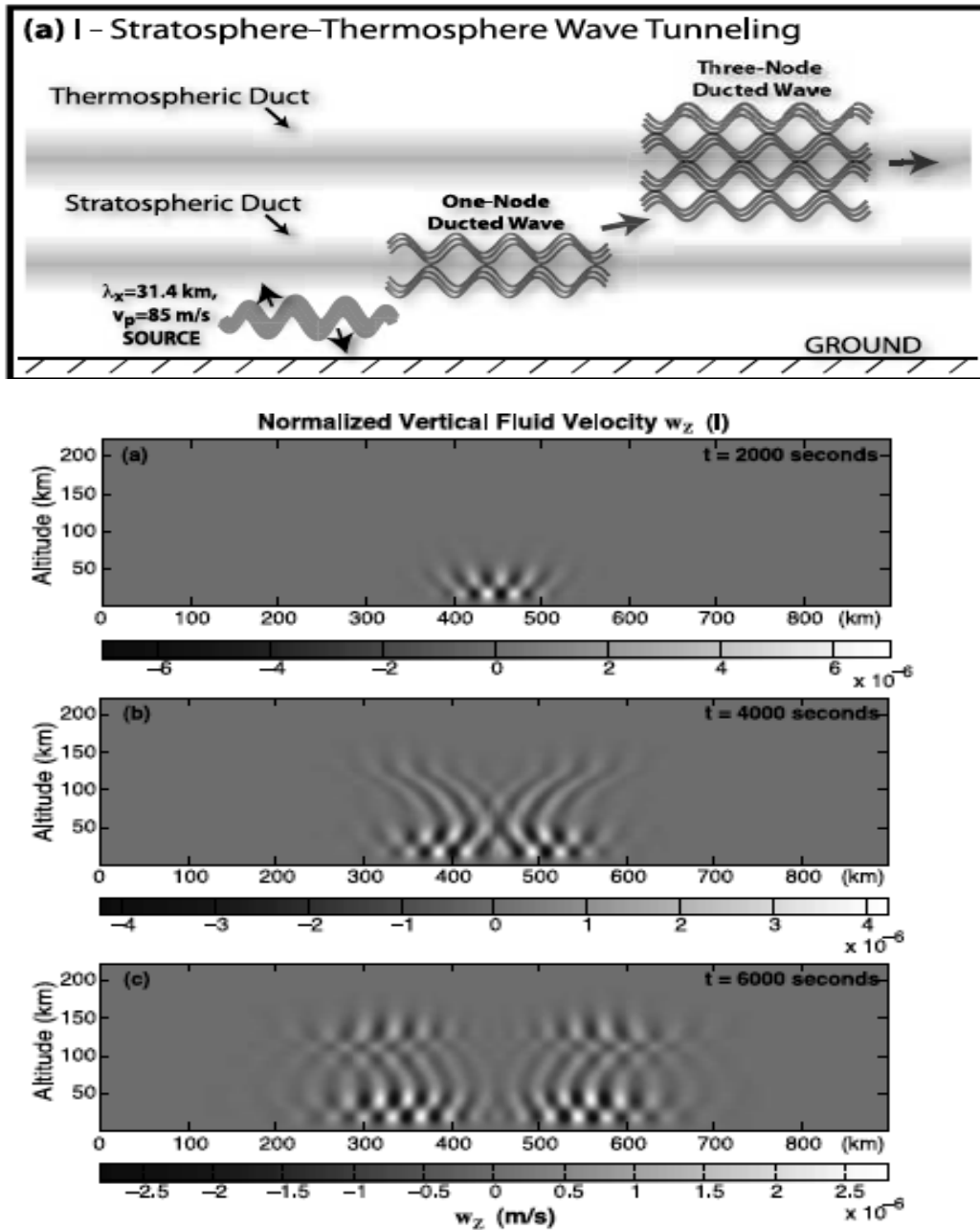


Figure 3.14. Schematic of simulation study reported by *Snively et al.* [2008] (top) showing the linear coupling between stratospheric and lower-thermospheric ducts (top). Three bottom images show the vertical perturbation velocity depicting (a) stratospheric ducted wave excitation, (b) vertical propagation into thermosphere and (c) ducted wave propagation in both stratospheric and thermospheric ducts.

The most distinct feature of altitude profile of the N^2 derived from the SABER data, shown in **Figure 3.12(a)**, is the maximum value in the mesopause at the altitude of ~ 95 km in the event number 40 and around ~ 100 km in the event number 41 data. This feature is constrained with a minimum value of N^2 around the stratopause (~ 50 km) and lower thermosphere (~ 115 km). Thus, it is possible to produce duct-mode waves in the mesopause region where the N^2 values are relatively large.

The m^2 profile then can be calculated using the derived Brunt-Väisälä frequency and the dispersion relation in Equation (2.4) by assuming the absence of background wind ($u=0$). Even though the dispersion relation is mostly valid for isothermal atmosphere, here we applied the equation to our non-isothermal atmosphere following the similar approach in previous studies by *Walterscheid et al.* [2001] and *Hecht et al* [2009]. The equation is given as

$$m^2 = \left(\frac{N^2}{\Omega^2} - 1 \right) k^2 - \frac{1}{4H^2} \quad (3.8)$$

where ω is the wave period obtained from the observation. In this discussion, we took only the event number 40 and 41, which were the closest to the expected center and the time of waves generation in the source region (~ 0600 UT).

Figure 3.15(b) shows the plot of the vertical wavenumber squared as a function of altitude for two events (event number 40 and 41). The two events show a similar trend in the vertical wavenumber squared, where the $m^2 < 0$ at the altitude of ~ 45 km and ~ 110 km, forming a duct region in between. When $m^2 > 0$ means that the wave can propagate vertically, on the other hand if $m^2 < 0$ means that waves vertically evanescent [*Walterscheid et al.*, 2001]. The altitude profile of m^2 shows there are evanescent regions around stratopause and lower thermosphere bounding the region with $m^2 > 0$ in

the altitude around 55-105 km. The m^2 values become relatively large in the altitude of 95-100 km. As we can see, the evanescent layer around the stratopause is thin; this suggests that there is a possibility of leakage of AGWs from the stratosphere into the mesosphere and then the waves trapped in the duct region. The AGWs can horizontally propagate further in the duct region until reach the distance of ~1400 km away then dissipate. Thus, the thermal ducted mode is the most possible scenario for small-scale CGWs seen in this coordinated observations. The evanescent region in the lower thermosphere (~110 km) shown in the **Figure 3.12(b)** also indicates that the waves could not propagate upward to the thermosphere region. This fact is consistent with the observation, where we did not observe any waves pattern in the OI 630-nm from the Rikubetsu all-sky camera.

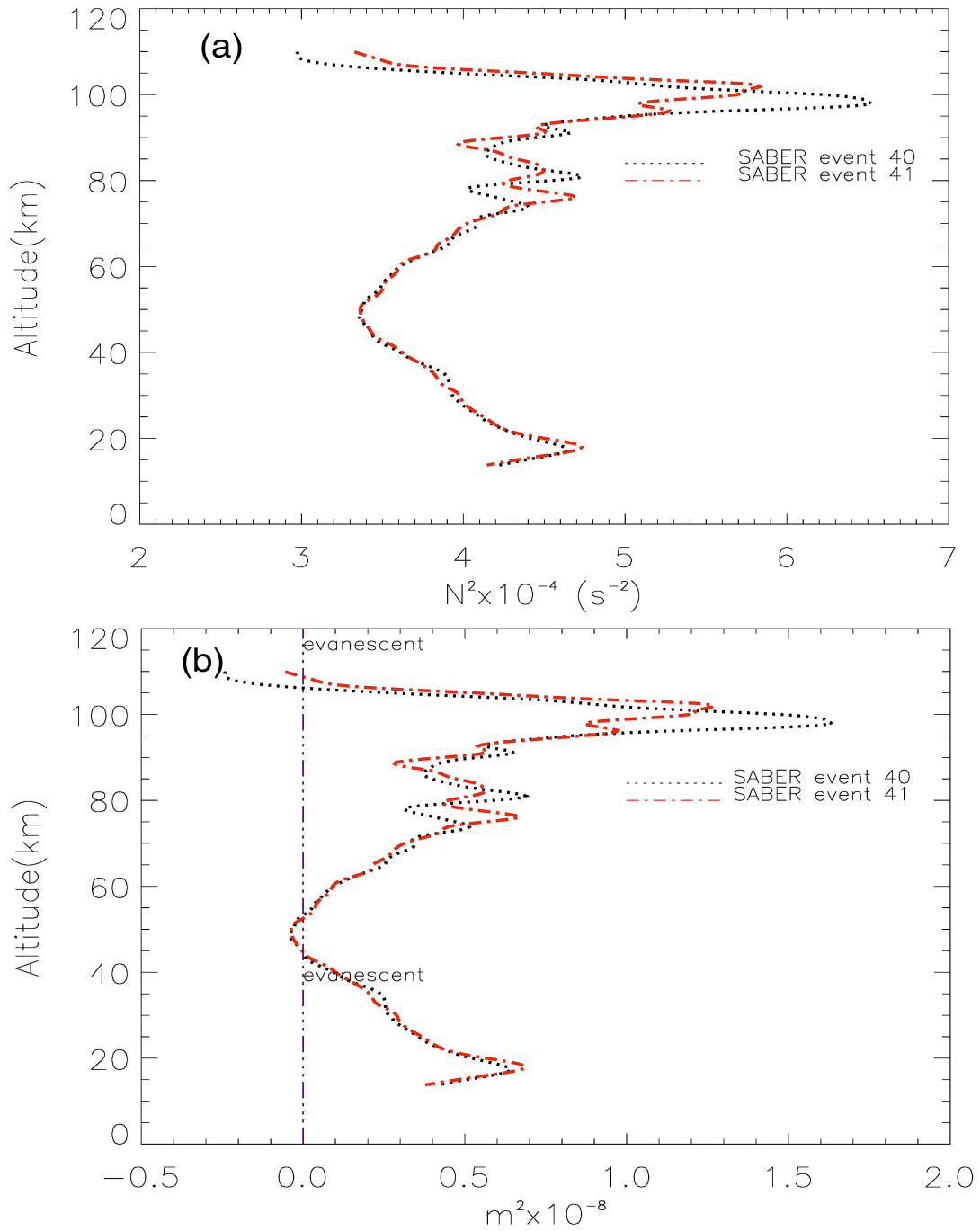


Figure 3.15. (a) Brunt-Väisälä frequency profile derived from the temperature profile of SABER data for event number 40 (black dashed-line) and event number 41 (red dashed-line). (b) Altitude profile of m^2 for SABER data event number 40 (black dashed-line) and number 41 (red dashed-line).

3.3. Concluding Remarks

We focused on the partial (arc-like shaped) concentric gravity waves (CGWs) event using the data from the coordinated observation of IMAP/VISI, all-sky imager at Rikubetsu, MTSAT, TRMM and MF radar at Wakkanai, combined with MERRA data. IMAP/VISI observed the CGW event in O₂ 762-nm emission at ~1203 UT on October 18, 2012 in the northeastern part of Japan. The similar pattern was also observed with the all-sky imager at Rikubetsu (43.5°N, 143.8°E) in the OI 557.7-nm and OH-band airglow emissions from ~1100-1200 UT. The horizontal wavelength, phase velocity and period of atmospheric gravity wave estimated from the OH data are $\sim 50 \pm 2$ km, $\sim 105 \pm 10$ m/s and 8.6 min., and those from OI 557.7-nm data are $\sim 51 \pm 2$ km, $\sim 96 \pm 8$ m/s and 9.2 min with the estimated elevation angle of $\sim 42.5^\circ$. On the other hand, the horizontal wavelength seen in IMAP/VISI O₂ 762-nm data is $\sim 67 \pm 10$ km.

In order to locate the point source accurately, we fitted the points manually picked from the wave front on airglow pattern to a circle by using the least square method. The best fitted circle for IMAP/VISI data has an outermost radius of ~ 1400 km and the center is at (33°N, 143°E) in geographical coordinate and those for OH and OI 557.7-nm emissions data at Rikubetsu the center are (33°N, 143°E) and (35°N, 143°E) with the outermost radius of ~ 1200 km and ~ 1100 km, respectively. Thus, we confirm that the CGWs observed both from IMAP/VISI and Rikubetsu all-sky imager generated by the same source since the radii and center positions are matched well with each other. The MTSAT and TRIMM data showed high-localized precipitation and convection activity over the Honshu island of Japan (up to 19.7 mm/h at 0600 UT), suggesting that this convective activity could be the source of the CGWs. The strong eastward wind around the tropopause was likely responsible to ~ 500 km shift the

estimated center eastward from the source. The relatively weak wind conditions above the tropopause (~ 18 m/s) allowed the wave to propagate upward then the strong zonal wind in the middle atmosphere (~ 60 m/s) reflected off the waves expanding in westward direction resulted in an arc-like shaped airglow pattern seen in the upper atmosphere.

The data showed that the CGWs could propagate up to ~ 1400 - 1500 km horizontally from the source to the mesopause region, but not further away. The small-scale horizontal wavelength and long distant propagation show that the CGWs observed both by IMAP/VISI and Rikubetsu all sky imager were likely ducted. From the analysis of the possible wind duct and thermal duct, we conclude that the wind duct was unlikely since the background wind from the Wakkanai MF radar during this period showed no strong wind in the opposite direction of the wave propagation, resulted only positive squared vertical wavenumber. On the other hand, the temperature profile obtained almost simultaneously with SABER is consistent with the generation of thermal duct. Thus, we concluded that the possible scenario is the thermal duct. The vertical wavenumber profile derived from temperature data obtained almost simultaneously with the SABER satellite around the expected center showed a possible ducting region between two evanescent regions at the stratopause and at lower thermosphere. The thin evanescent layer in the stratopause might allow some atmospheric gravity waves to leak into mesosphere and then ducted and travelled for long distance. **Figure 3.16** summarizes the plausible scenario of the CGWs propagation mechanism revealed with this study. However, the limitation of the observational data makes it difficult to explain precisely. Therefore, a future simulation study based on this result would be very useful to explain the characteristics of CGWs propagation in details.

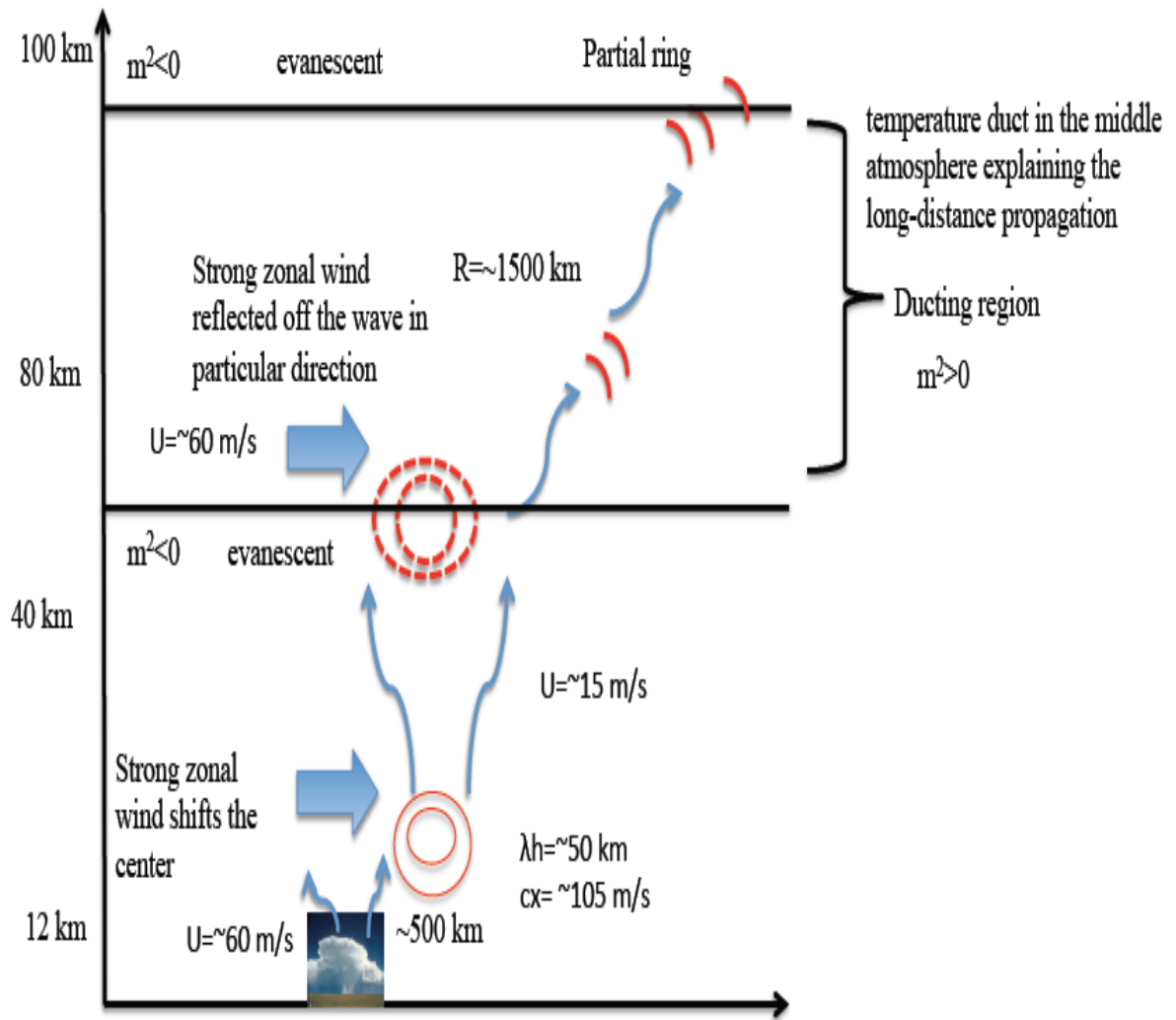


Figure 3.16. Schematic drawing of plausible scenario of propagation mechanism of partially CGWs seen in O_2 (762 nm) airglow emission from IMAV/VISI and OI (557.7 nm) and OH emissions from Rikubetsu all-sky camera on 18 October 2012.

Chapter IV

Observation Result and Discussion Part II: Statistical Study

3-years of Concentric Gravity Waves Variability in the Mesopause as Observed by IMAP/VISI

This chapter focuses on the statistical characteristics on the concentric gravity waves (CGWs) in the mesopause, especially on the occurrence variability, global and seasonal variation. In the past, CGWs event was investigated with case study basis, local information was clarified [e.g., *Hapgood and Taylor*, 1988; *Dewan et al.*, 1998; *Suzuki et al.*, (2007 and 2013), *Vadas et al.*, 2010; *Yue et al.*, (2009 and 2013); *Akiya et al.*, 2014, *Azeem et al.*, 2005; *Miller et al.*, 2015]. A statistical study on CGWs is necessary for comprehensive and quantitative understanding of the coupling process between lower and upper atmospheres since CGW event is useful to identify causal relationship between the two regions. To address this issue, space-based observations are ideal since they cover wider area globally and can measure atmospheric gravity waves without cloud obscuration.

Gong et al., [2015] surveyed the CGWs activity in the stratosphere (~40 km altitude) in CO₂ emissions (4.3 μ m) from AIRS (Atmospheric Infrared Sounder) data in the nadir direction. They showed the global distribution of CGWs occurred in January

and July 2010 with horizontal wavelengths ranging from 50 to 1700 km. They found that the occurrence of CGWs was mostly related to tropical and sub-tropical deep convective activities in summer and jet imbalance in winter. However, this study did not clarify its seasonal dependence since their analysis spanned only two months data. To our best knowledge, there is no statistical study of CGWs in the mesopause region. IMAP/VISI is one of a few space-based instruments that is capable of imaging small scale gravity waves in airglow emission (several tens km) in the mesosphere and lower thermosphere (MLT) region [Sakanoi *et al.*, 2011; Akiya *et al.*, 2014], which makes this instrument suitable for investigating the global characteristics of CGWs.

We found totally 235 CGWs events from the O₂ A-band airglow emission data taken with IMAP/VISI during the period of 3 years from 2013 to 2015. Using the method described in Chapter II, the wave parameters were derived. The occurrence variabilities in seasonal, latitudinal and global distribution of the CGWs events are shown in the observation result. In the discussion, the occurrence variability and global distribution of occurrence are compared with the results presented in past studies. Background wind data from GAIA was used to explain the latitudinal and seasonal distributions.

4.1. Observation Results

4.1. 1. Occurrence Probability and Characteristics of CGWs

Figure 4.1 summarizes the quantitative characteristics of all of the CGW events examined in this study. **Figure 4.1(a)** is the histogram showing the total IMAP/VISI paths per month. IMAP/VISI provides data for approximately 15 paths/day which

makes total of ~400-500 data path/month in average. The number of paths normalizes the occurrence probability, distribution of horizontal wavelength and maximum radius. **Figure 4.1(b)** indicates the number of CGW events per month. Out of the 235 CGW events, 104, 85 and 46 events occurred in 2013, 2014 and 2015, respectively. Compared **Figure 4.1(a)** and **Figure 4.1(b)**, it is clear that the occurrence rate of CGWs event is less than 5% of total paths. From the 3 years data, we can see that the occurrence is low during the solstice (June-July and December-January) and significantly higher during non-solstice months (February-May and August-November).

Figure 4(c) shows the measured horizontal wavelength of CGWs ranging from 50 km to 250 km, and it was dominated (~70 %) by 60-150 km scale. Note that the result of horizontal wavelength is constrained by the horizontal resolution of IMAP/VISI instrument mentioned in the Chapter II, meaning that CGWs with smaller scales (less than approximately 30 km) that usually can be observed from the ground-based imager are not detected here. *Gong et al.* [2015] reported that majority of the horizontal wavelength in the stratopause falls between 400-1300 km with the average values in January and July are 800 km and 500 km, respectively. These results are much larger than that observed by IMAP/VISI (60-150 km). This difference is probably caused by the difference in the spatial resolution (~30 km for IMAP/VISI data, ~50 km for AIRS data) and swath width of field-of-view between AIRS (1650 km) and IMAP/VISI (600 km).

Figure 4.1(d) shows the maximum radius of the CGWs pattern ranging from 200-3000 km, and it was dominated by 600-1800 km radius. The maximum radius was calculated from the center to the outermost ring seen in the O₂ airglow emission data. This result of maximum radius is greater than those estimated with ground-based imager presenting the maximum radius between 200 km to 300 km [e.g., *Suzuki et al.*,

2007; Yue *et al.*, 2009]. Nishioka *et al.* [2013] reported a concentric gravity wave event in the F-region that was observed in GPS TEC data over the North America after the 2013 Moore EF5 tornado. The waves could propagate up to ~1600 km in the horizontal direction. A recent simulation study by Liu *et al.* [2014] suggested that typhoon-generated CGWs could travel up to a few thousand km from its center. Our results from IMAP/VISI data clearly demonstrate a comprehensive and precise characteristics are not only for the maximum distance of CGWs propagation but also for its seasonal dependence and horizontal wavelength. **Figure 4.2** shows the characteristics of the observed CGWs separated in northern and southern hemisphere. The occurrence rate is slightly higher in the northern hemisphere by ~24%, suggesting that the convective activities over the continent are likely more significant as the source of the CGWs.

4.1.2. Global, Seasonal and Latitudinal Distribution of CGWs

The global distribution of CGWs center is shown in **Figure 4.3(a)**. The global map shows some favored regions (e.g. Central Africa and North America) but very few events over equatorial convective regions such as Indonesia and South America. One possible explanation for the lack of CGWs at equator is that the spatial scale of CGWs may be small in this region. If a CGW is excited by vertically deep and horizontally small heating at Equator associated with individual convective clouds, its horizontal wavelength might become smaller than the horizontal resolution of IMAP/VISI. However, the strength of latent heat release, or the nature of middle-atmosphere structure (wind, pressure, temperature) could also be the reason of the contrast drawn between the favored region and over the convection region in the tropics.

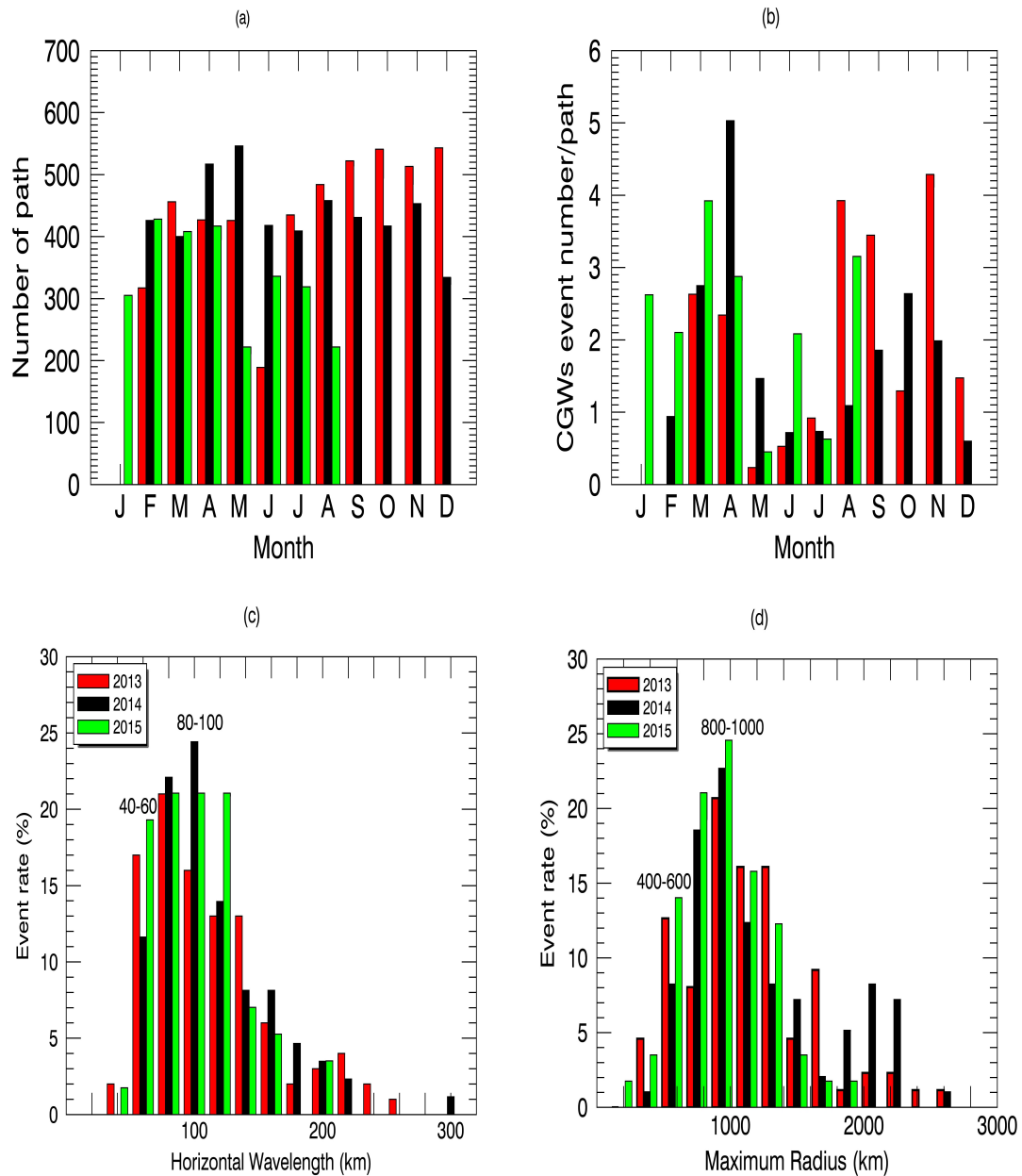


Figure 4.1. (a) Monthly-total path number from January to December. Red, black and green are 2013, 2014 and 2015, respectively. (b) Monthly occurrence number of the CGWs. (c) Distribution of horizontal wavelength. Horizontal wavelength of 60-150 km is dominant. (d) Distribution of the maximum radius shows the majority of the CGWs travel a distance of 600-1800 km from its center.

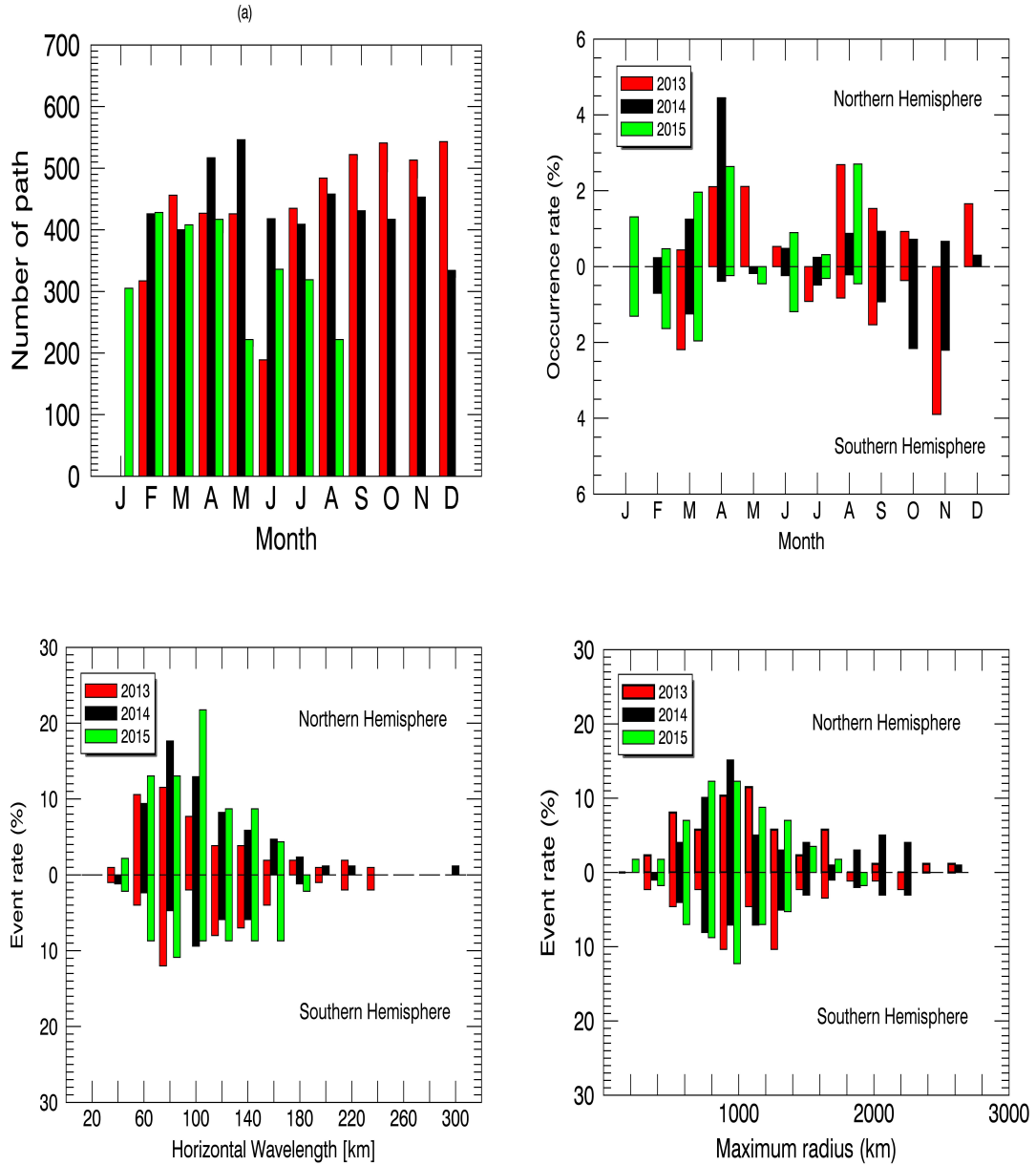


Figure 4.2. The same as **Figure 4.1**, except these figures show the distribution of occurrence rate (b), horizontal wavelength (c) and (d) maximum radius in northern and southern hemispheres.

The latitudinal distribution of the CGW centers shown in **Figure 4.3(b)** has peaks at mid-latitudes (40°N and 40°S) and minimum at low-latitudes (10°S). In this figure, the number of CGW event was zonally averaged at each latitudinal interval of

10°, and normalized by the observation time, considering the fact that the ISS orbit provides more observation in the higher latitudes than in the equatorial region. The result is consistent with a modeling study by *Liu et al.* [2014] that displayed the occurrence of CGWs excited by convective activity were seen at low to middle latitudes with a broad range of radius. *Liu et al.* [2014] also showed the occurrence is low around the equator, consistent with the IMAP/VISI observation. Note that the horizontal resolution of the CGWs in their simulation study is ~200 km.

Figure 4.4 shows the number of CGW events normalized by observation time as a function of latitude from January to December. The solid red line represents the data in 2013, black line is 2014 and green line is 2015. It is obvious that strong latitudinal and seasonal variations exist, and that CGWs are active in the periods of February-May and August-November, and also there is significant asymmetry between the northern and the southern hemisphere particularly during the active period (February-May and August-November) **as shown in Figure 4.5 and Figure 4.6.**

If we look precisely at the result during the high activity period (February-May and August-November), there are more events in the southern hemisphere during February-March, but this toggles rapidly to more occurrences in the northern hemisphere during the April-May. During August-September, more events occur in the northern hemisphere, and there is a rapid change during October-November toward more occurrences in the southern hemisphere. These significant changes before and after the equinoxes are probably related with the background wind changes its direction [e.g. *Yue Deng et al.*, 2014].

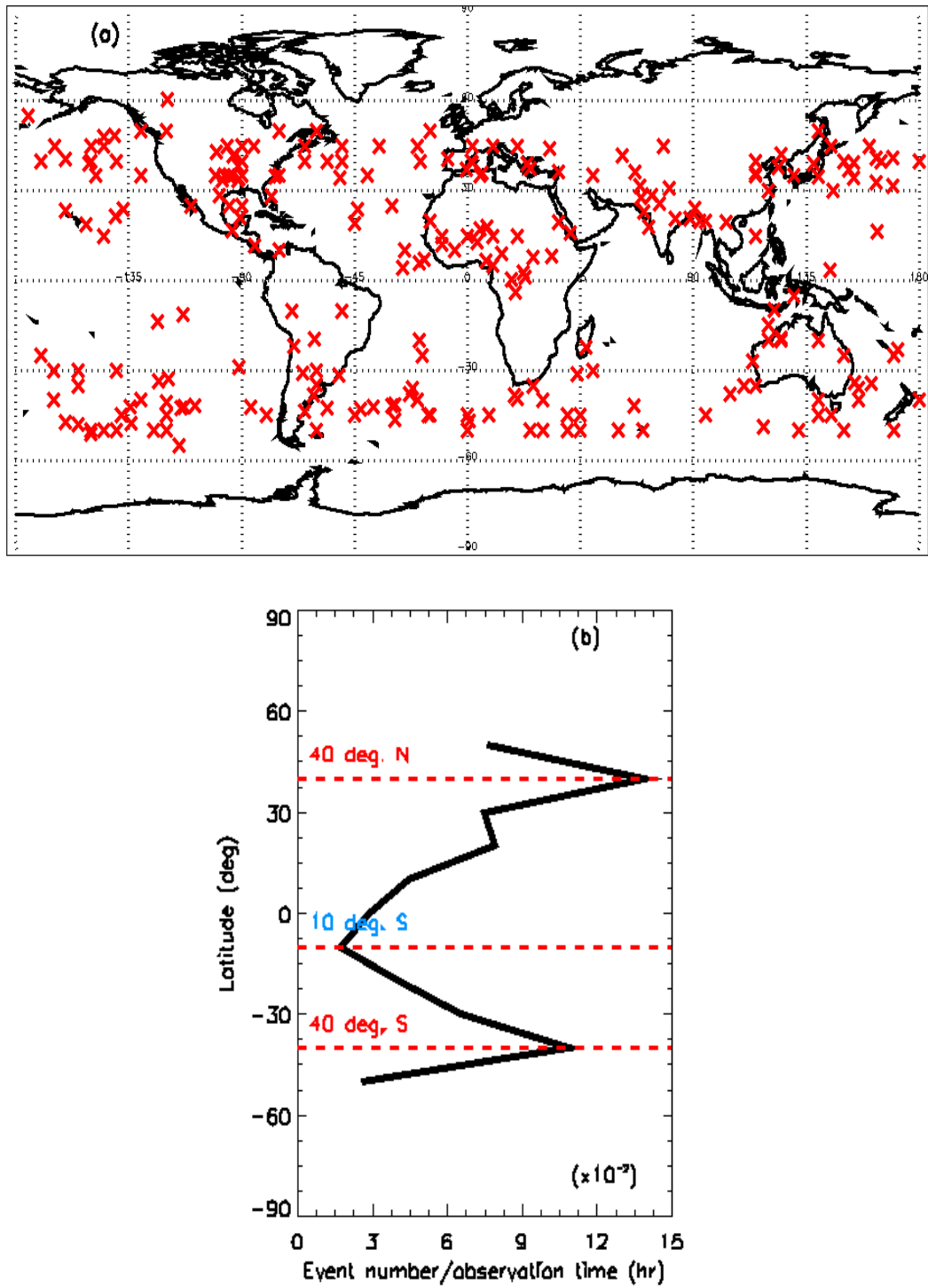


Figure 4.3. (a) Global distribution of CGWs occurrence during the period of 2013 to 2015. (b) Zonally averaged latitudinal occurrence probability of CGWs event which shows maxima at 40°N and 40°S and minimum at 10°S.

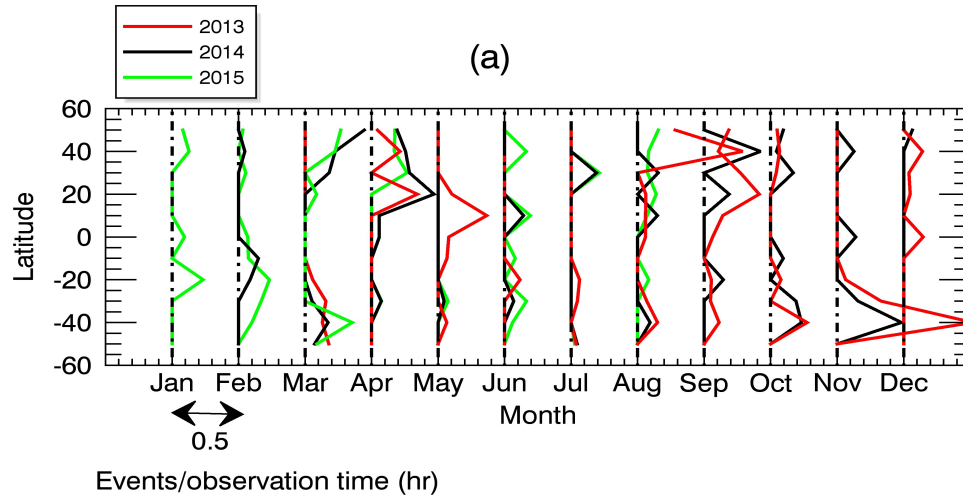


Figure 4.4. Latitudinal distribution of event number from January to December (a) and transition of CGWs occurrence between northern and southern hemisphere before and after the equinoxes (b).

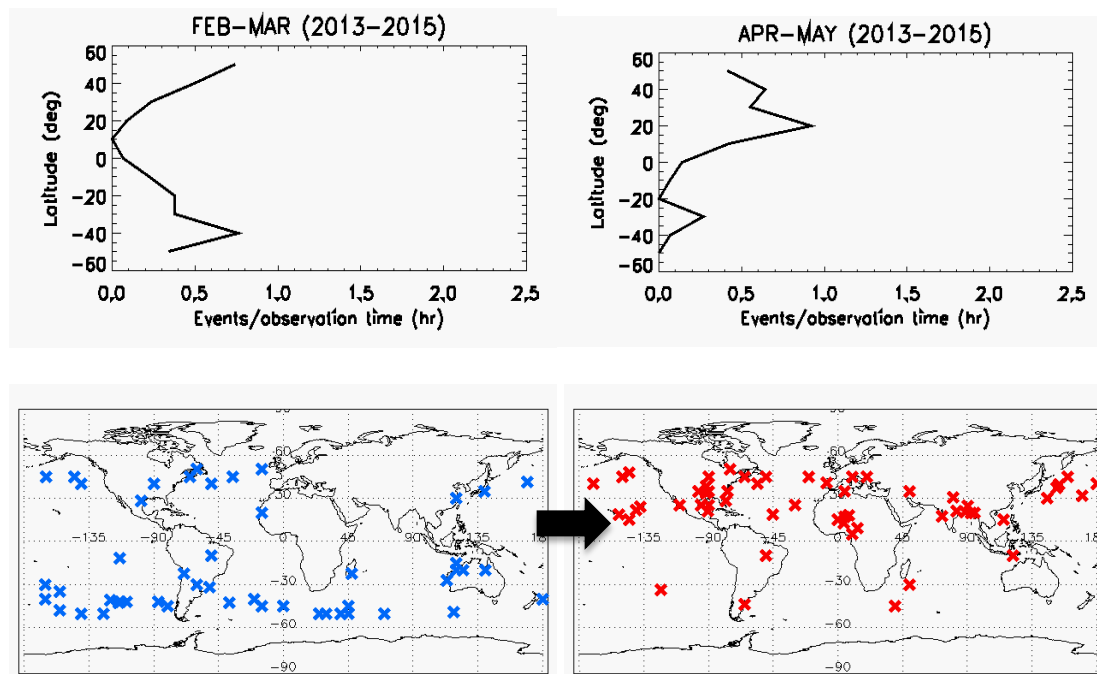


Figure 4.5. Transition of CGWs occurrence between northern and southern hemisphere before and after the equinoxes on February-March to April May seen in the latitudinal distribution profile (top) and global map (bottom).

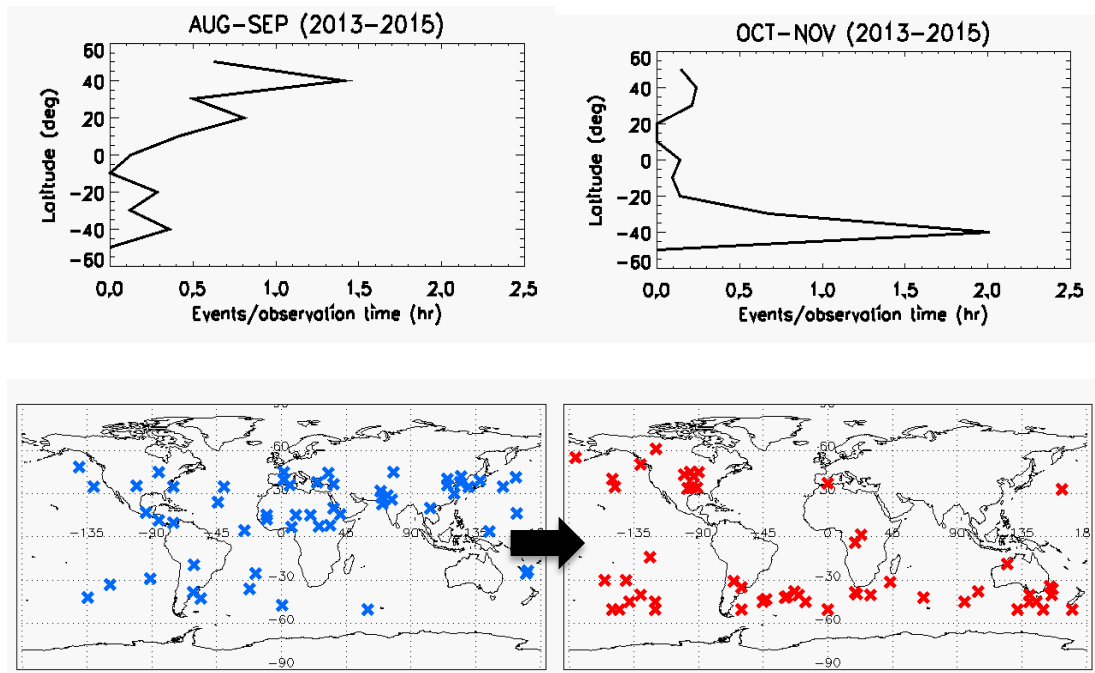


Figure 4.6. Same as **Figure 4.5**, except for transition seen between August-September and October-November.

4.2. Discussion

4.2.1. Comparison with Previous Studies: Occurrence Variability and Global Distribution

Yue et al. [2009] analyzed ~5 years data from an all sky camera at Yucca Ridge Field Station, Colorado (40.7°N, 104.9°W) and used the OH data (~87 km altitude) from 2003 to 2008. 9 CGW events were found with a typical horizontal wavelength of 40 to 80 km. They found that the CGWs occurred only during the periods of May-June and August-September. This observation was conducted in the northern hemisphere (~40°N). In contrast, IMAV/VISI data covered both hemispheres and showed that the global occurrence was seen in every month, with significantly higher during the periods

of February-May and August-November, as presented in **Figure 4.1(b)**. The inter-hemispheric transition seen in **Figure 4.5** and **Figure 4.6** obviously shows that the activities during February-March and October-November are mainly in the southern hemisphere, explaining the relative decrease of event detection during the same periods by *Yue et al.* [2009]. **Figure 4.7(a)** shows the comparison of seasonal dependence of CGWs obtained from Yucca Ridge data and IMAP/VISI data.

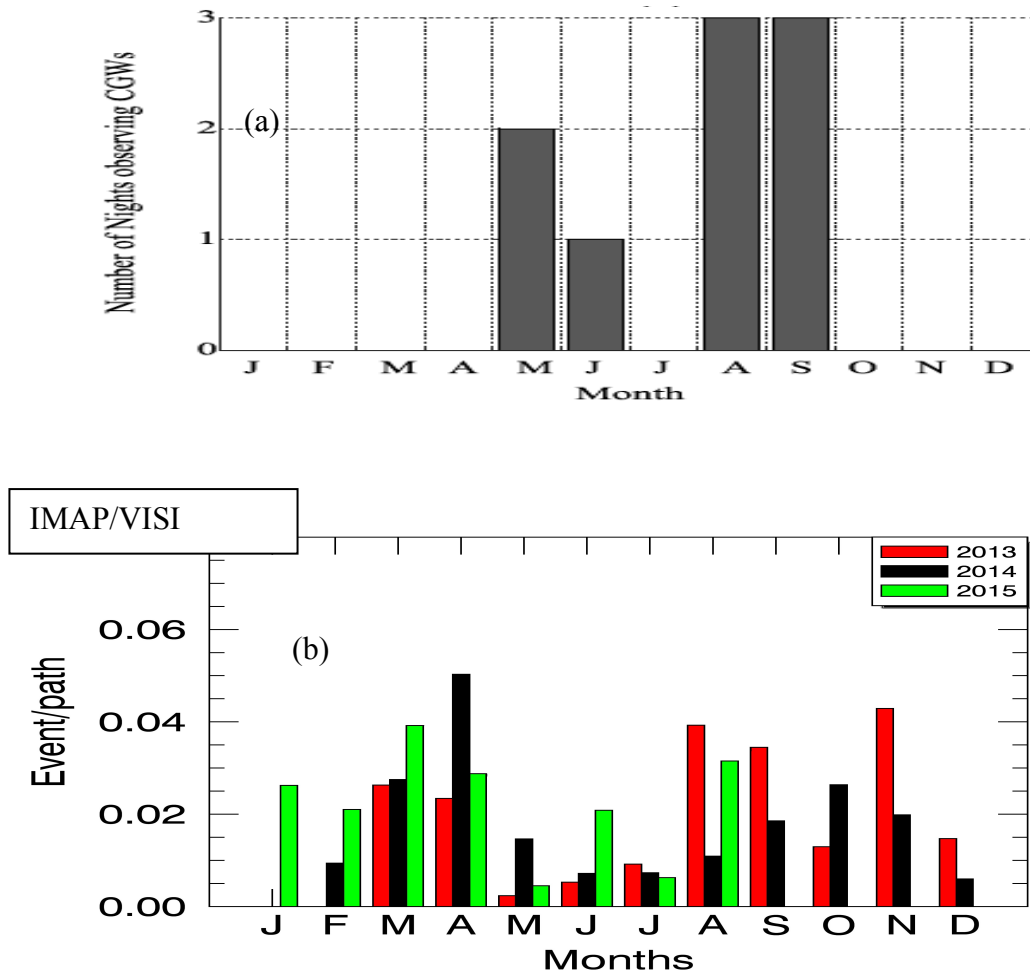


Figure 4.7. Occurrence variability comparison between ground-based observation at (a) Yucca Ridge (*Yue et al.*, 2009) and (b) IMAP/VISI (present study).

The global distribution of the CGWs in the mesopause has never been reported so far, and therefore, this study makes the first attempt to reveal the global distribution of CGWs in this region. On the other hand, there are several studies of global distribution of gravity waves in the lower atmosphere. For an instance, the global distribution of gravity waves without classification was analyzed using the AIRS radiance data in the stratopause [e.g., *Hoffmann and Alexander*, 2009; *Gong et al.*, 2012; *Hoffmann et al.*, 2013]. In addition, *Ern et al.* [2011] reported the global distribution of general gravity wave momentum flux using the HIRDLS data for various altitudes from 30-70 km.

Focusing on the CGWs statistical study, *Gong et al.*, [2015] reported a global distribution of CGWs in the stratopause (~40 km) and compared it with the ECMWF model. They found a similar distribution with the result derived from IMAP/VISI data, showing a band-like high activity occurrence in the southern hemisphere both for daytime (descending) and nighttime (ascending). They also found several hotspots over deep convective region, such as Indonesia, Central Africa and South America. The correlation between the deep convective region and CGWs occurrence was higher during day time, while during nighttime they found that the occurrence was shifted from the deep convective activity region to higher latitude, especially over Indonesia. This result has a good agreement with our result where we observed almost no activity over deep convective region over Indonesia. Despite the similarity of the distribution, the result reported by *Gong et al.* [2015] did not show full seasonal variability. Thus, the full seasonal variability estimated from IMAP/VISI data gives us an advantage for clarifying more comprehensive picture on the global characteristics of CGW.

4.2.2. Relationship of Zonal and Latitudinal Distribution of CGWs with the Background Wind

Previous studies demonstrated that upward propagation of CGWs strongly affected by the background wind. Both *Suzuki et al.* [2007] and *Yue et al.* [2009] suggest that only very low background wind conditions allow CGWs to propagate upward to the mesopause without any significant wind filtering. According to this suggestion, the CGWs occurrence should be maximized around the equinoxes when the wind speed is close to zero in the stratosphere and mesosphere, while very low CGWs activity is expected during solstices when the wind speeds are strongest. This idea is basically consistent with the IMAP/VISI data showing that the CGW activity with low activity at solstice and high around equinox. Thus, it implies that not only near zero winds ($< \sim 10$ m/s) allow the CGWs to propagate upward to the mesopause (~ 95 km) but low to moderate background wind conditions (~ 15 - 30 m/s) are important to take into account as well [*Vadas et al.*, 2009]. However, the present study also demonstrates interesting behaviors of the CGW occurrence, such that there is year-to-year variability and sometimes the occurrence peak is not always at equinoxes but shifted before or after. As shown in **Figure 4.1(b)**, the total number of occurrence varies each year in which one year has significantly higher occurrence than others. The occurrence in 2013 (104 events) is higher by $\sim 22\%$ than in 2014 (85 events). The occurrence in 2015 (46 events) even though only 8 months, seems to be comparable with 2014 occurrence. The variation may due to the variation of source, background profile (wind and temperature) in the middle atmosphere. However, since the mechanism is complicated, it is difficult to tell straight forward which factor is the most significant. More detailed analysis is needed, however this is out of the scope of this thesis.

In order to validate the hypothesis regarding the effect of the background wind

mentioned above, we used the zonal-mean zonal wind from GAIA data assuming that the meridional winds are much smaller than the zonal wind and the longitudinal dependence is negligibly small. Using GAIA, we analyzed the distribution of zonal wind at altitude range between 10-95 km for each month from 90°S- 90°N, in order to represent the latitudinal and seasonal wind between the tropopause and airglow layer. Vertical propagation is limited to conditions when the horizontal phase speed (c_x) is equal to the horizontal background speed (U) in the direction of wave propagation [McLandress, 1998]. Under these conditions, the waves encounter critical level at certain altitude when the wave speed reached the background wind speed. **Figure 4.8** shows an example of latitudinal distribution of zonal-mean zonal wind obtained with the GAIA data on March 2013. The solid line represents the minimum wind speed (westward wind) and dashed line represents the maximum wind speed (eastward wind). The range between the minimum and maximum winds indicates the critical level region.

We can see that the atmospheric gravity waves with $c_x=50$ m/s should be outside the critical level filtering range, meaning that the westward and eastward phases of the CGWs can propagate through the stratosphere and mesosphere without encountering critical level filtering. Based on this method, we examined the critical level filtering effect for the each season using the results on the seasonal variation of CGWs described in the Section 3.1. We divided the season into solstices, i.e., December-January and June-July, and around equinoxes where the CGWs occurrence is high (February-May and August-November). The results are shown in **Figure 4.9**. We can see that around the equinoxes (February-May and August-November), the wind range is 0 to $\sim\pm 30$ m/s which means the waves with $|c_x| > \sim 30$ m/s can propagate in both direction in the latitudinal range of 50°S-50°N. On the other hand, only high-speed waves ($|c_x| > \sim 100$

m/s) can propagate upward during solstices due to the strong zonal wind (~ 100 m/s) at the mid-latitude. These analyses explain the statistical result in the present study showing higher occurrence around the equinoxes than the solstices. In this figure, we also confirm the hypothesis that not only near zero winds allow the CGWs to propagate upward to the mesopause, but also low to moderate wind (~ 30 -50 m/s) can support the upward propagation. Further, this moderate winds (~ 30 -50 m/s) must also contribute to produce the partial rings pattern seen in the airglow emissions at mesopause.

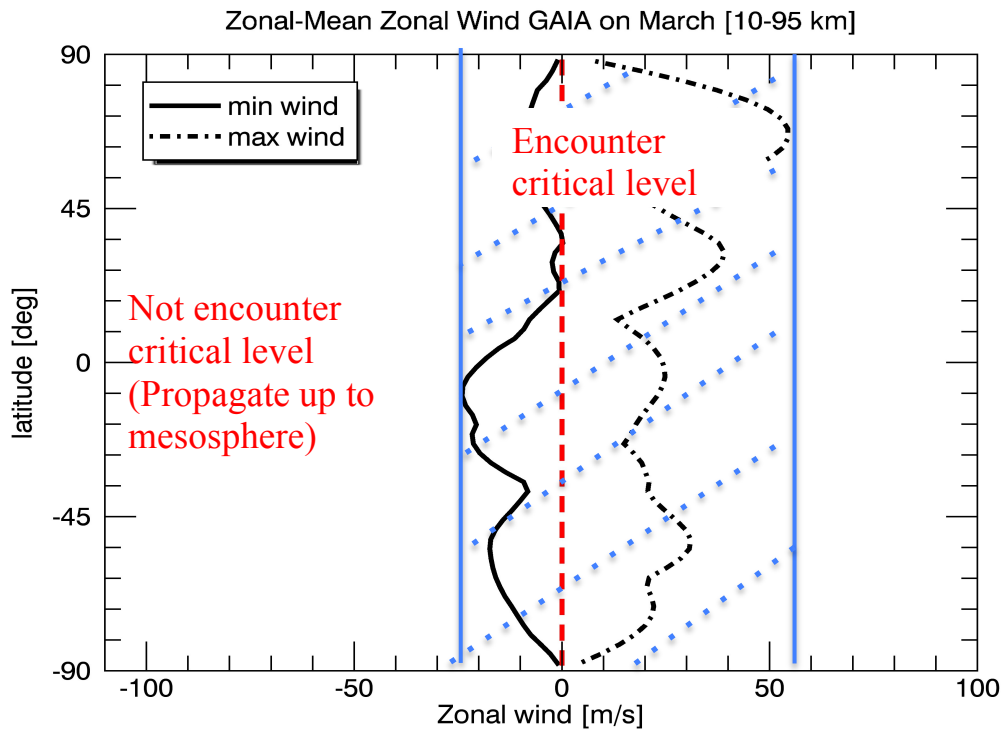


Figure 4.8. Latitudinal distribution of zonal-mean zonal wind from the GAIA data between the altitude ranges of 10-95 km. The solid line represents the minimum wind (westward wind) and dashed line represents the maximum wind (eastward wind). The Blue shaded region indicates the critical level region. The waves with horizontal phase speed (c_x) $> \pm 50$ m/s can avoid the critical level filtering.

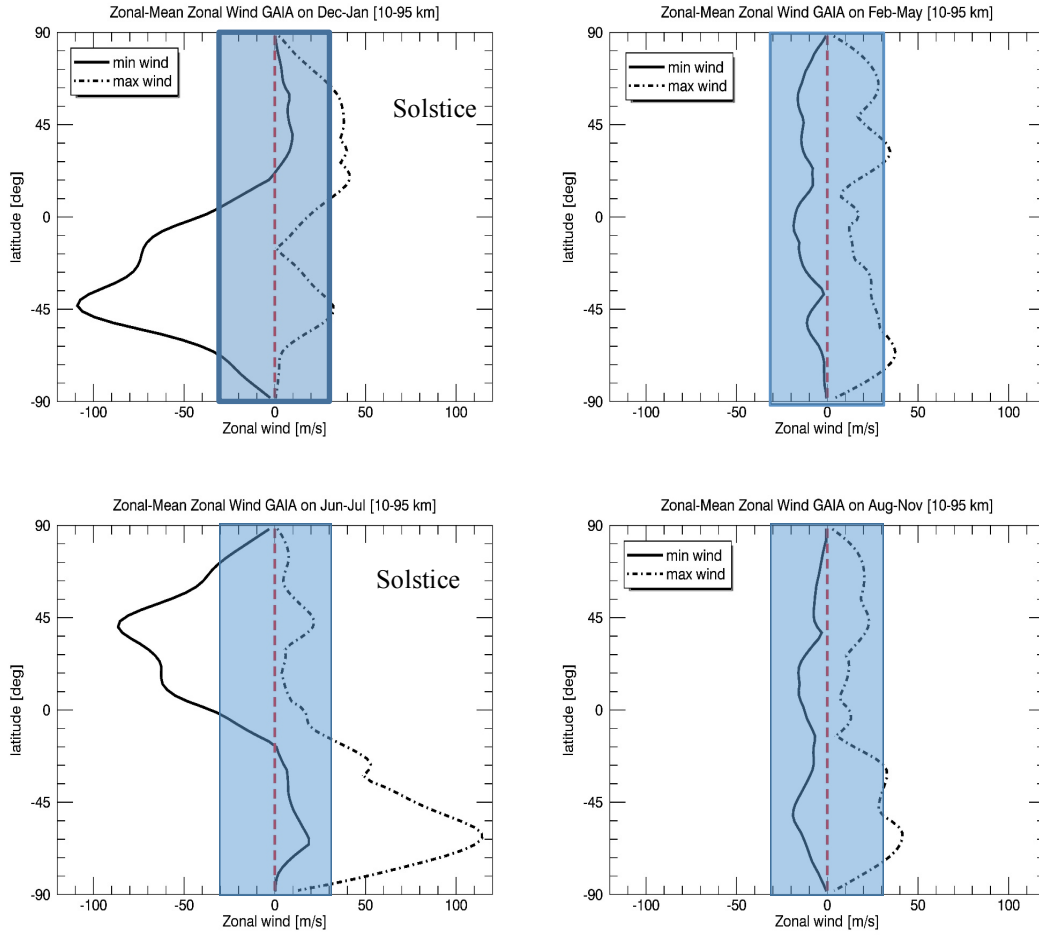


Figure 4.9. Latitudinal distribution of zonal-mean zonal wind from the GAIA data between altitude range of 10-95 km on solstices (Dec-Jan and Jan-Jul) and equinoxes (Feb-May and Aug-Nov).

4. 3. Concluding Remarks

The CGW occurrence variability in the mesopause region (~ 95 km) was examined using 3 years O_2 A-band airglow data taken with IMAF/VISI. Statistical analysis of 235 CGWs events indicated that horizontal wavelength ranged from 50 km to 250 km, dominated (70% of total event) by 60 km to 150 km (i.e., mesoscale structures). The

maximum radius of concentric pattern showed that CGWs could travel for a distance up to 3000 km with typical radii of 600-1800 km. The global distribution of CGW centers showed preferential occurrence at mid-latitudes, with peaks around 40°N and 40°S , and a minimum around 10°S . On the interhemispheric seasonable variability, more events were found at mid-latitudes in the summer hemisphere, with a rapid transition between northern and southern hemispheres occurring around the equinoxes. The monthly occurrence probability showed a similar seasonal variation for each year; lower during the solstices and higher during non-solstice months. This observation led us to conclude that low to moderate background wind conditions were preferable for the unfiltered upward propagation of CGWs launched in the lower atmosphere. Further, the global map of CGWs events showed several preferable regions (e.g. Central Africa, North America) but very few events over convective regions in South America and Indonesia. The relationships between CGW events at mesopause, their sources and wave propagations is the key issue to understand the precise characteristics of CGWs, such as regional occurrence, year-to-year variability and so on. However, these issues are beyond the scope of this study and will be investigated in the future.

Chapter V

Conclusion

We focused on the spatial and temporal variability of concentric gravity waves (CGWs) in the mesopause region using the O₂ A-band (762 nm) nightglow data from IMAP/VISI data. Concentric gravity waves (CGWs) are useful to identify one-to-one correspondence between the source region and upper atmosphere. However, there were only a handful of reports on the CGWs since the opportunity of CGWs detection was rather limited. To address this issue, we performed two approaches: The first approach is a case study of CGWs to clarify the detailed characteristics of wave generation and propagation mechanism using coordinated satellite and ground-based observation data as well as simulation result. The second approach is a statistical study to examine the global distribution and seasonal variability of CGWs.

On the case study, we examined a partial CGWs event obtained with coordinated IMAP/VISI and an all sky imager at Rikubetsu observations. IMAP/VISI observed the partial CGWs in O₂ 762-nm emission at ~1203 UT on October 18, 2012 in the northeastern part of Japan. The similar airglow pattern was also seen in the all-sky imager data at Rikubetsu (43.5°N, 143.8°E) in the OI 557.7-nm and OH-band airglow emissions from ~1100-1200 UT. The least square method was carried out to fit a circle

to observed concentric pattern to estimate the circle center, i.e. the source point, and the horizontal wavelength. Outermost radius of the best fitted circle for IMAF/VISI data is ~ 1400 km centering at (33°N , 143°E) in geographical coordinate, and those of OH and OI 577.7-nm emissions data at Rikubetsu are ~ 1200 km centering at (33°N , 143°E) and ~ 1100 km centering at (35°N , 143°E) respectively. The horizontal wavelength, phase velocity and period of atmospheric gravity wave are estimated from successive image data at Rikubetsu, and found to be ~ 50 km, ~ 105 m/s and 8.6 min. from the OH data, and ~ 51 km, ~ 96 m/s and 9.2 min from OI 577.7-nm data the elevation angle of $\sim 42.5^\circ$. On the other hand, the horizontal wavelength seen in IMAF/VISI O_2 762-nm data is ~ 67 km. It is evident that CGWs observed both from IMAF/VISI and Rikubetsu all-sky imager were generated by the same source since the outermost radii; horizontal wavelength and center positions are matched well with each other. From the MTSAT and TRMM data during this period, there was a high-localized precipitation (up to 19.7 mm/h at 0600 UT) and convection activity (convective index ~ 40) over the Honshu island of Japan, around the estimated source point, suggesting that it is reasonable to consider this activity as the source of the CGWs. The strong eastward wind around the tropopause of ~ 40 m/s obtained from MERRA data was likely responsible to eastward shift between the estimated center [33°N , 143°E] and the most active area of convection/precipitation [33°N , 136°E]. From TRMM data, it is found that the relatively low winds above the tropopause (~ 18 m/s), which allowed the wave to propagate upward. Then, the waves were probably reflected by the strong zonal wind in the middle atmosphere (~ 60 km altitude) and finally expanded in a particular direction resulted in partial CGWs (an arc-like shaped pattern) seen in the airglow layers. The observed CGWs were likely ducted considering the fact that the small scale CGWs (~ 50 km in horizontal wavelength) could propagate up to ~ 1400 - 1500 km horizontally at

mesopause. The vertical wavenumber profile derived from temperature data from SABER satellite around the expected center of the wave showed a possible ducting region between two evanescent regions in the stratopause (~45 km altitude) and lower thermosphere (~ 110 km altitude). The thin evanescent layer in the stratopause may allow some waves to leak into mesosphere and then ducted and travelled for long distance.

On the second approach, we conducted a statistical study using 235 CGWs events obtained from IMAV/VISI data for 3 years. We applied the similar method as described in the case study to derive the wave parameters. It is found that the horizontal wavelength of CGWs ranged from 50-250 km, dominated (70%) by 60 to 150 km. The maximum radius of CGWs was ~3000 km and typical radii ranged of 600 – 800 km, suggesting that the mesoscale CGWs could travel for such a long distance. The global distribution of CGW center locations showed preferential occurrence at mid-latitudes, with peaks on 40°N and 40°S, and a minimum around 10°S. More events tend to occur in the summer hemisphere mid-latitudes, with a strong transition between northern and southern hemispheres occurring around the equinoxes. The monthly occurrence probability showed a similar seasonal variation for each year; low activity at solstices and high activity during non-solstice months. The comparison between this observational data with zonal wind profile from the GAIA model led us to conclude that low to moderate background winds around equinoxes (~ less than 30 m/s) were preferable for the unfiltered upward transmission of CGWs launched from the lower atmosphere. The global map of CGWs locations showed several preferable regions, such as Central Africa, North America, but very few events over convective regions in South America and Indonesia. Although we have revealed the characteristics of CGWs, some of issues, such as regional occurrence variability showing the contrast draw

between some preferable regions and convective regions in tropics, and year-to-year variation are still unsolved. These issues are beyond the scope of this study and will be investigated in the future.

References

- Adachi, T., M. Yamaoka, M. Yamamoto, Y. Otsuka, L. Yuichi, H. Huixin, C-C. Hsiao, A.B. Chen, R-R. Hsu (2010), Midnight latitude-altitude distribution of 630 nm airglow in the Asian sector measured with FORMASAT-2/ISUAL, *J. Geophys. Res.*, 115, A9, CiteID A09315.
- Akiya, Y., A. Saito, T. Sakanoi, Y. Hozumi, A. Yamazaki, Y. Otsuka, M. Nishioka, and T. Tsugawa (2014), First spaceborne observation of the entire concentric airglow structure caused by tropospheric disturbance, *Geophys. Res. Lett.*, 41, 6943–6948, doi:10.1002/2014GL061403.
- Azeem, I., J. Yue, L. Hoffmann, S. D. Miller, W. C. Straka III, and G. Crowley (2015), Multisensor profiling of a concentric gravity wave event propagating from the troposphere to the ionosphere, *Geophys. Res. Lett.*, 42, 7874–7880, doi:10.1002/2015GL065903.
- Burrage, M. D., N. Arvin, W.R. Skinner, and P.B. Hays (1994), Observations of the O₂ atmospheric band nightglow by the High-Resolution Doppler Imager, *J. Geophys. Res.*, 99, 15,017–15,023.
- Coble, M. R., G. C. Papen, and C. S. Gardner (1998), Computing two-dimensional unambiguous horizontal wavenumber spectra from OH airglow images, *IEEE Trans. Geosci. Remote Sens.*, **36**, 368–382.

- Deng, Y., Y. Huang, Q. Wu, J. Noto, D. Drob, and R. B. Kerr (2014), Comparison of the neutral wind seasonal variation from midlatitude conjugate observations, *J. Geophys. Res. Space Physics*, 119, doi:10.1002/2013JA019716.
- Dewan, E. M., R. H. Picard, R. R. O'Neil, H. A. Gardiner, J. Gibson, J. D. Mill, E. Richards, M. Kendra, and W. O. Gallery (1998), MSX satellite observations of thunderstorm-generated gravity waves in mid-wave infra-red images of the upper stratosphere, *Geophys. Res. Lett.*, 25, 939 – 942, doi:10.1029/98GL00640.
- Dörnbrack, A. and Nappo, C.J. (1997), A note on the application of linear wave theory at a critical level. *Boundary-Layer Meteorol.* 82:399-416.
- Ern, M., Preusse, P., Gille, J. C., Hepplewhite, C. L., Mlynchak, M. G., Russell III, J. M., and Riese, M.: Implications for atmospheric dynamics derived from global observations of gravity wave momentum flux in stratosphere and mesosphere, *J. Geophys. Res.*, 116, D19107, doi:10.1029/2011JD015821, 2011.
- Feofilov, A. G., et al. (2009), Daytime SABER/TIMED observations of water vapor in the mesosphere: retrieval approach and first results, *Atmos. Chem. Phys.*, 9, 8139–8158.
- Fetzer, E. J., and J. C. Gille, Gravity wave variance in LIMS temperatures, part I, Variability and comparison with background winds, *J. Atmos. Sci.*, 51, 2461–2483, 1994
- Fritts, D.C., Gravity wave saturation in the middle atmosphere: A review of theory and observations, *Rev. Geophys.* 2, 2, 275-308, 1984.
- Fritts, D. C., and R. A. Vincent (1987), Mesospheric momentum flux studies at Adelaide, Australia: Observations and a gravity wave-tidal interaction model, *Journal of the Atmospheric Sciences*, 44 (3), 605–619.

- Fritts, D. C., Isler, J. R., Hecht, J. H., Waletscheid, R. L., and Andreassen, O. (1997), Wave breaking signatures in sodium densities and OH nightglow. 2. Simulation of wave and instability structures. *J. Geophys. Res.* 102:6669–6684.
- Fritts, D. C., and M. J. Alexander, Gravity wave dynamics and effects in the middle atmosphere, *Rev. Geophys.*, 41(1), 1003, doi:10.1029/2001RG000106, 2003.
- Garcia, F. J., M. J. Taylor, and M. C. Kelley (1997), Two-dimensional spectral analysis of mesospheric airglow image data, *Appl. Opt.*, **36**, 7374–7385.
- Fritts, D.C., and P. K. Rastogi, Convective and dynamical instabilities due to gravity wave motions in the lower and middle atmosphere: Theory and observations, *Radio Sci.*, 20, 1247-1277, 1985.
- Fritts, D. C. and Yuan, L.: An Analysis of Gravity Wave Ducting in the Atmosphere: Eckart's Resonances in Thermal and Doppler Ducts, *J. Geophys. Res.*, 94, 18455–18466, 1989.
- Gauge, K. S. and Balsley, B. B. (1978), Doppler radar probing of the clear atmosphere. *Bull. Am. Meteorol. Soc.* 59:1074–1093.
- Giovanni TOVAS homepage, available at: <http://gdata1.sci.gsfc.nasa.gov>. (Accessed: 2013, March 15).
- Goldstein, S. (1931), On the stability of superposed streams of fluids of different densities, *Proceedings of the Royal Society A*, (132), 524–548.
- Gong, J., J. Yue, and D. L. Wu (2015), Global survey of concentric gravity waves in AIRS images and ECMWF analysis, *J. Geophys. Res. Atmos.*, 120, 2210–2228, doi:10.1002/2014JD022527.
- Gossard, E. E., and W. H. Hooke (1975), *Waves in the Atmosphere*, Elsevier, New York.

- Greer, R. G. H., Murtagh, D. P., McDade, I. C., Llewellyn, E. J., and Witt, G. (1987), Rocket photometry and the lower-thermospheric oxygen nightglow, *Phil. Trans. R. Soc. Lond.*, A323, 579–595.
- Hapgood, M. A., and M. J. Taylor (1982), Analysis of airglow image data, *Ann. Geophys.*, 38, 805–813.
- Hays, P.B., J.F. Kafkalidis, and W.R. Skinner (2003), A global view of the molecular oxygen night airglow, *J. Geophys. Res.*, 108: 4646.
- Hecht, J. H., R. L. Walterscheid, D. C. Fritts, J. R. Isler, D. C. Senft, C. S. Gardner, and S. J. Franke (1997), Wave breaking signatures in OH airglow and sodium densities and temperatures. 1. Airglow imaging, Na lidar, and MF radar observations. *J. Geophys. Res.* 102:6655–6668.
- Hecht, J.H., M.J. Alexander, L. Walterscheid, L. J. Gelinas, R. A. Vincent, A. D. MacKinnon, J. M. Woithe, P. T. May, W. R. Skinner, M. G. Mlynchak, and J. M. Russell III (2009), Imaging of atmospheric gravity waves in the stratosphere and upper mesosphere using satellite and ground-based observations over Australia during the TWICE campaign, *J. Geophys. Res.*, 114, D18123, doi:10.1029/2008JD011259.
- Hoffmann, L., X. Xue, and M. J. Alexander (2013), A global view of stratospheric gravity wave hotspots located with Atmospheric Infrared Sounder observations, *J. Geophys. Res. Atmos.*, 118, 416–434, doi:10.1029/2012JD018658.
- Holton, J. R., The role of gravity wave induced drag and diffusion in the momentum budget of the mesosphere, *J. Atmos. Sci.*, 39, 791–799, 1982.
- Holton, J.R. (2004), An introduction to dynamic meteorology, ch. 7, p. 196.

- Horinouchi, T., T. Nakamura, and J.-I. Kosaka (2002), Convectively generated mesoscale gravity waves simulated throughout the middle atmosphere, *Geophys. Res. Lett.*, 29(21), 2007, doi:10.1029/2002GL016069.
- Igarashi, K., Y. Murayama, K. Hocke, R. Yamazaki, M. Kunitake, M. Nagayama, and I. Nishimuta (1999), Coordinated observations of the dynamics and coupling processes of mesosphere and lower thermosphere winds with MF radars at the middle-high latitude, *Earth Planet Science*, **51**, 657–664.
- Isler, J. R., Taylor, M. J., and Fritts, D. C.: Observational Evidence of Wave Ducting and Evanescence in the Mesosphere, *J. Geophys. Res.*, 102, 26301–26313, 1997.
- Jacobson, A. R., R. Holzworth, J. Harlin, R. Dowden, and E. Lay (2006), Performance assessment of the Worldwide Lightning Location Network (WWLLN) using the Los Alamos Sferic Array (LASA) array, *J. Atmos. Oceanic Technol.*, 23, 1082–1092.
- H. Jin, Y. Miyoshi, D. Pancheva, P. Mukhtarov, H. Fujiwara, H. Shinagawa, Response of migrating tides to the stratospheric sudden warming in 2009 and their effects on the ionosphere studied by a whole atmosphere-ionosphere model GAIA with COSMIC and TIMED/SABER observations, *Journal of Geophysical Research: Space Physics*, 2012, 117, A10
- Kato, S. (1996), Diurnal atmospheric oscillation, 1. Eigenvalues and Hough functions, *J. Geophys. Res.*, 71, 3201-3209.
- Killeen, T.L., Q. Wu, S.C. Solomon, D.A. Ortland, W.R. Skinner, R.J. Nijewski, D.A. Gell (2006), TIMED Doppler Interferometer: Overview and recent result, *J. Geophys. Res.*, 111, A10, CiteID A10S01.

- Lin, C. H., C. H. Liu, J. Y. Liu, C. H. Chen, A. G. Burns, and W. Wang (2010), Midlatitude summer nighttime anomaly of the ionospheric electron density observed by FORMOSAT-3/COSMIC, *J. Geophys. Res.*, 115, A03308.
- Lindzen, R.S. (1967), Thermally driven diurnal tide in the atmosphere, *Quart. J. Roy Meteor. Soc.*, 86, 18-42.
- Lindzen, R.S. (1981), Turbulence and stress owing to gravity wave and tidal breakdown, *J. Geophys. Res.*, 86, 9707-9714.
- Little, C. G. (1969), Acoustic methods for the remote probing of the lower atmosphere. *Proc. IEEE* 57:571–578.
- Liu, Z., D. Ostrenga, W. Teng, and S. Kempler (2012), Tropical Rainfall Measuring Mission (TRMM) Precipitation Data and Services for Research and Application, *American Meteorol. Soc.*, DOI:10.1175/BAMS-D-11-00152.1.
- Liu, H.-L., J. M. McInerney, S. Santos, P. H. Lauritzen, M. A. Taylor, and N. M. Pedatella (2014), Gravity waves simulated by high-resolution Whole Atmosphere Community Climate Model, *Geophys. Res. Lett.*, 41, 9106–9112, doi:10.1002/2014GL062468.
- Makhlouf, U. B., R. H. Picard, and J. R. Winick, Photochemical-dynamical modeling of the measured response of airglow to gravity waves, *J. Geophys. Res.*, **100**, 11289–11311, 1995.
- Madden, R.A and Julian, P.R. (1972), Further evidence of global-scale 5-day pressure waves, *J. Atmos. Sci.*, 29, 1464-1469.
- Manson, H. A. (1990), Gravity wave horizontal and vertical wavelengths: An update of measurements in the mesosphere region (~80–100 km). *J. Atmos. Sci.* 47:2765–2773.

- Marsh, A. K. P., N. J. Mitchell, and L. Thomas, Lidar studies of stratospheric gravity-wave spectra, *Planet. Space Sci.*, 39, 1541–1548, 1991.
- Matsuno, T., A quasi-one-dimensional model of the middle atmospheric circulation interacting with internal gravity waves, *J. Meteorol. Soc. Jpn.*, 60, 215–226, 1982.
- McDade, I. C., D. P. Murtagh, R. G. H. Greer, P. H. G. Dickinson, G. Witt, J. Stegman, E. J. Llewellyn, L. Thomas, and D. B. Jenkins (1986), ETON 2: Quenching parameters for the proposed precursors of $O_2(b^1\Sigma_g^+)$ and $O(^1S)$ in the terrestrial nightglow, *Planetary and Space Science*, 34 (9), 789–800.
- Meinel, A. B. (1950), OH emission bands in the spectrum of the night sky, *Astrophysical Journal*, 111, 555.
- Mende, S.B., H. Frey, S.P. Geller, and G.R. Swenson (1998), Gravity wave modulated airglow observation from spacecraft, *Geophys. Res. Lett.*, 25: 757–760.
- Mertens, C. J., M. G. Mlynczak, M. Lo´pez-Puertas, P. P. Wintersteiner, R. H. Picard, J. R. Winick, L. L. Gordley, and J. M. Russell III (2001), Retrieval of mesospheric and lower thermospheric kinetic temperature from measurements of CO_2 15 μm Earth limb emission under non-LTE conditions, *Geophys. Res. Lett.*, 28(7), 1391–1394.
- S. D. Miller et al. Upper atmospheric gravity wave details revealed in nightglow satellite imagery, *Proceedings of the National Academy of Sciences* (2015). DOI: 10.1073/pnas.1508084112
- Molina, A. (1983), Sodium nightglow and gravity waves. *J. Atmos. Sci.* 40:2444–2450.
- Minschwaner, K., Herceg, D., Budzien S.A., Dymond, K.F., Fortna, C., McCoy, R.P., (2007), Observations of middle ultraviolet emissions in the middle and lower thermosphere: NO , O_2 , O and Mg^+ , *J. Geophys. Res.*, 112, A10, CiteID A10311.

- Mitchell, N. J., L. Thomas, and A. K. P. Marsh, Lidar observations of long-period gravity waves in the stratosphere, *Ann. Geophys.*, 9, 588–596, 1991.
- Murtagh, D.P., G. Witt, J. Stegman, I.C. McDade, E.J. Llewellyn, F. Haris, and R.G.H Greer (1990), An assessment of proposed $O(^1S)$ and $O_2(b^1\Sigma_g^+)$ nightglow excitation parameters, *Planet. Space Sci.*, 38: 43-53.
- Nakamura, T., T. Tsuda, S. Fukao, and S. Kato, Comparison of the mesospheric gravity waves observed with the MU radar (35N) and the Adelaide MF radar (35S), *Geophys. Res. Lett.*, 20, 803–806, 1993a.
- Nakamura, T., T. Tsuda, S. Fukao, A. H. Manson, C. E. Meek, R. A. Vincent, and I. M. Reid, Mesospheric gravity waves at Saskatoon (52_N), Kyoto (35_N), and Adelaide (35_S), *J. Geophys. Res.*, 101, 7005–7012, 1996.
- Nakamura, T., T. Aono, T. Tsuda, A.G. Admiranto, E. Achmad, and Suranto (2003), Mesospheric gravity waves over a tropical region observed by OH airglow imaging in Indonesia. *Geophys. Res. Lett.* 30.
- Nappo, C. J. (2002), *An Introduction to Atmospheric Gravity Waves*, chap. 1: Fundamentals, pp. 1 – 54, Academic Press, San Diego.
- Newsom, R. K. and Banta, R. M.: 2002, 'shear Instability Gravity Waves in the Stable Nocturnal Boundary Layer as Observed by Doppler Lidar during CASES-99', *J. Atmos. Sci.*, in press.
- NOAA/OAR/ESRL PSD homepage, available at: <http://www.esrl.noaa.gov/psd/>. (Accessed: 2013, March 1).
- Ohsawa, T., H. Ueda, A. Hayashi, and J. Matsumoto (2001), Diurnal variation of convective activity and rainfall in tropical Asia, *J. Meteorol. Soc. Jpn.*, 79: 333-352.

- Ottersten, H., Hardy, K. R., and Little, C. G. (1973), Radar and sodar probing of waves and turbulence in statically stable clear-air layers. *Boundary-Layer Meteorol.* 4:47–89.
- Perwitasari, S., T. Sakanoi, A. Yamazaki, Y. Otsuka, Y. Hozumi, Y. Akiya, A. Saito, K. Shiokawa, and S. Kawamura (2015), Coordinated airglow observations between IMAP/VISI and a ground-based all-sky imager on concentric gravity wave in the mesopause, *J. Geophys. Res. Space Physics*, 120, 9706–9721, doi:10.1002/2015JA021424.
- Peterson, A. W. and L. M. Keiffaber (1973), Infrared photography of OH airglow structures. *Nature* 242:321–322.
- Pierce, A. D., and S. C. Coroniti (1966), A mechanism for the generation of acoustic-gravity waves during thunderstorm formation, *Nature*, 210, 1209–1210.
- Poulos, G. S., W. Blumen, D. C. Fritts, J. K. Lundquist, J. Sun, S. P. Burns, C. Nappo, R. Banta, R. Newsom, J. Cuxart, E. Terradellas, B. Balsley, and M. Jensen (2001), CASES-99: A comprehensive investigation of the stable nocturnal boundary layer. *Bull. Am. Meteorol. Soc.* 83:555–581.
- Preusse, P., B. Schaeler, J. T. Bacmeister, and D. Offermann, Evidence for gravity waves in CRISTA temperatures, *Adv. Space Res.*, 24, 1601–1604, 1999.
- Russell, J. M., III, M. G. Mlynczak, L. L. Gordley, J. Tansock, and R. Esplin (1999), An overview of the SABER experiment and preliminary calibration results, in *Proceedings of the SPIE, 44th Annual Meeting, Denver, Colorado, July 18–23*, vol. 3756, pp. 277–288
- Sagawa, E., T.J. Immel, H.U. Frey, S.B. Mende (2005), Longitudinal structure of the equatorial anomaly in the nighttime ionosphere observed by IMAGE/FUV, *J. Geophys. Res.*, 110, Issue A11, CiteID A11302.

- Sakanoui, T., Y. Akiya, A. Yamazaki, Y. Otsuka, A. Saito, I. Yoshikawa, (2011), Imaging observation of the earth's mesosphere, thermosphere and ionosphere by VISI of ISS-IMAP on the international space station, *IEEJ Trans. on Fundamentals and Materials*, vol. 131, 12, pp.983-988, doi:10.1541/ieejfms.131.983.
- Sentman, D. D., E. M. Wescott, R. H. Picard, J. R. Winick, H. C. Stenbaek Nielsen, E. M. Dewan, D. R. Moudry, F. T. Sao Sabbas, M. J. Heavner, and J. Morrill (2003), Simultaneous observations of mesospheric gravity waves and sprites generated by a midwestern thunderstorm, *J. Atmos. Terr. Phys.*, 65, 537–550, doi:10.1016/S1364-6826(02)00328-0.
- Shiokawa, K., Y. Otsuka, and T. Ogawa (2009), Propagation characteristics of nighttime mesospheric and thermospheric waves observed by optical mesosphere thermosphere imagers at middle and low latitudes, *Earth Planets Sci.*, 61, 479-491.
- Shiokawa, K., Y. Katoh, M. Satoh, M. K. Ejiri, and T. Ogawa (2000), Integrating-sphere calibration of all-sky cameras for nightglow measurements, *Adv. Space Sci.*, **26**, 1025–1028.
- Simkhada, D. B., J. B. Snively, M. J. Taylor, and S. J. Franke (2009), Analysis and modeling of ducted and evanescent gravity waves observed in the Hawaiian airglow, *Ann. Geophys.*, 27, 3213–3224.
- Snively, J. B., and V. P. Pasko (2008), Excitation of ducted gravity waves in the lower thermosphere by tropospheric sources, *J. Geophys. Res.*, 133, A06303, doi:10.1029/2007JA012693.
- Sutherland, B. R. and Yewchuk, K.: Internal wave tunnelling, *J. Fluid Mech.*, 511, 125–134, 2004.

- Suzuki, S. K. Shiokawa, Y. Otsuka, T. Ogawa, M. Kubota, M. Tsutsumi, T. Nakamura, and D. C. Fritts (2007b), Gravity wave momentum flux in the upper mesosphere derived from OH airglow imaging measurements, *Earth Planet Space*, 9, 421–428.
- Suzuki, S., K. Shiokawa, Y. Otsuka, T. Ogawa, K. Nakamura, and T. Nakamura (2007a), A concentric gravity wave structure in the meso- spheric airglow images, *J. Geophys. Res.*, 112, D02102, doi:10.1029/ 2005JD006558.
- Suzuki, S., S. L. Vadas, K. Shiokawa, Y. Otsuka, S. Kawamura, and Y. Murayama (2013a), Typhoon-induced concentric airglow structures in the mesopause region, *Geophys. Res. Lett.*, 40, 5983–5987, doi:10.1002/2013GL058087.
- Swenson, G. R and C. S. Gardner, (1998), Analytical models for the response of the mesospheric OH* and Na layers to atmospheric gravity waves. *J. Geophys. Res.* **103**:6271–6294.
- Swenson, G. R., J. Tang, F. Kamalabadi, and S. J. Franke (2005), Methods of deducing intrinsic measurements of high frequency atmospheric gravity waves (AGWs), in SPIE, *Remote Sensing of Clouds and Atmosphere X*, vol. 5979, edited by K. Schaefer, A. Comeron, J. R. Slusser, R. H. Picard, M. R. Carleer, and N. Sifakis, pp. 261–269.
- Takeuchi, W., T. Nemoto, T. Kaneko, and Y. Yasoka (2007), Development of MTSAT data processing, visualization and distribution systemon WWW, *J. Jpn. Soc. Photogramm. Remote Sens.*, 46(6), 42–48.
- Taylor, G. I. (1931), Effect of variation in density on the stability of superposed streams of fluid, *Proceedings of the Royal Society of London. Series A, Containing Papers of a Mathematical and Physical Character*, 132 (820), 499–523.

- Taylor, M. J., D. N. Turnbull, and R. P. Lowe (1995), Spectrometric and imaging measurements of a spectacular gravity wave event observed during the ALOHA-93 campaign. *Geophys. Res. Lett.* 22:2848–2852.
- Tsuda, T., Y. Murayama, M. Yamamoto, S. Kato, and S. Fukao, Seasonal variation of momentum flux in the mesosphere observed with the MU radar, *Geophys. Res. Lett.*, 17, 725–728, 1990.
- Tsuda, T., and K. Hocke (2004), Application of GPS radio occultation data for studies of atmospheric waves in the middle atmosphere and ionosphere. *J. Meteorol. Soc. Jpn.* 82: 419–426.
- Taylor, M. J., and M. A. Hapgood (1988), Identification of a thunderstorm as a source of short period gravity waves in the upper atmospheric night- glow emissions, *Planet. Space Sci.*, 36, 975–985, doi:10.1016/0032-0633(88)90035-9.
- Taylor, M.J., E.H. Ryan, T.F. Tuan and R. Edwards (1993), Evidence of Preferential Directions for Gravity Wave Propagation Due to Wind Filtering in the Middle Atmosphere, *J. Geophys. Res.* 98, 6047–6057.
- Taylor, M. J., D. N. Turnbull, and R. P. Lowe (1995), Spectrometric and imaging measurements of a spectacular gravity wave event observed during the ALOHA-93 campaign, *Geophys. Res. Lett.*, 22(20), 2849– 2852.
- Tuan, T. F., Hedin, R., Silverman, S. M. and Okuda, M. (1979) On gravity wave induced Brunt-Väisälä oscillations. *J. Geophys. Res.* 84, 393.
- Vadas, S. L., J. Yue, C.Y. She, P. Stamus, and A. Z. Liu (2009), A model study of the effects of winds on concentric rings of gravity waves from a convective plume near Fort Collins on 11 May 2004, *J. Geophys. Res.*, 114, D06103, doi:10.1029/2008JD010753.

- Vargas, F., G. R. Swenson, A. Z. Liu, and D. Gobbi (2007), O(¹S), OH, and O₂(b) airglow layer perturbations due to AGWs and their implied effects on the atmosphere, *Journal of Geophysical Research - Atmospheres*, 112 (D14), D14102.
- Vadas, S., J. Yue, and T. Nakamura (2012), Mesospheric concentric gravity waves generated by multiple convective storms over the North American Great Plain, *J. Geophys. Res.*, 117, D07113, doi:10.1029/2011JD017025.
- Vincent, R. A. and Reid, I. M. (1983), HF Doppler measurements of mesoscale gravity wave momentum fluxes. *J. Atmos. Sci.* 40:1321–1333.
- “Wakkanai, Japan MF Radar”, available at: <http://cedarweb.hao.ucar.edu/wiki/>. (Accessed: 2013, June 3).
- Walterscheid, R. L., J. H. Hecht, R. A. Vincent, I. M. Reid, J. Woithe, and M. P. Hickey (1999), Analysis and interpretation of airglow and radar observations of quasi-monochromatic gravity waves in the upper mesosphere and lower thermosphere over Adelaide, Australia, *J. Atmos. Sol. Terr. Phys.*, 61, 461–478.
- Walterscheid, R.L., G. Schubert, D.G. Brinkman (2001), Small scale gravity waves in the upper mesosphere and lower thermosphere generated by deep convective tropical convection, *J. Geophys. Res.*, Vol. 106, doi: 10.1029/2000JD000131509.00.
- Watanabe, T., M. Nakamura, and T. Ogawa (1981), Rocket measurements of O₂ atmospheric and OH Meinel bands in the airglow, *J. Geophys. Res.*, 86, 5768-5774.
- Wilson, R., M.-L. Chanin, and A. Hauchecorne, Gravity waves in the middle atmosphere observed by Rayleigh lidar, 1, Case studies, *J. Geophys. Res.*, 96, 5153–5167, 1991

- Whiteway, J. A., and A. I. Carswell, Lidar observations of gravity wave activity in the upper stratosphere over Toronto, *J. Geophys. Res.*, 100, 14,113–14,124, 1995.
- Witt, G., J. Stegman, B. H. Solheim and E.J. Llewellyn (1979), A measurement of the $O_2 (b^1 \Sigma_g^+)$ atmospheric band and the $O(1S)$ green line in the nightglow, *Planet. Space Sci.*, 27,341-350.
- Yue, J., S. L. Vadas, C.-Y. She, T. Nakamura, S. C. Reising, H.-L. Liu, P. A. Stamus, D. A. Krueger, W. Lyons, and T. Li (2009), Concentric gravity waves in the mesosphere generated by deep convective plumes in the lower atmosphere near Fort Collins, Colorado, *J. Geophys. Res.*, 114, D06104, doi:10.1029/2008JD011244.
- Yue, J., L. Hoffmann, and M.J. Alexander (2013), Simultaneous observations of convective gravity waves from a ground-based airglow imager and the AIRS satellite experiment, *J. Geophys. Res.*, 118: 1-14, doi:10.1002/jgrd.50341.